PHYSICAL MECHANISMS AFFECTING HOT CARRIER-INDUCED DEGRADATION IN GALLIUM NITRIDE HEMTS

By

Shubhajit Mukherjee

Dissertation

Submitted to the Faculty of the

Graduate School of Vanderbilt University

in partial fulfillment of the requirements

for the degree of

DOCTOR OF PHILOSOPHY

in

Interdisciplinary Materials Science

December, 2015

Nashville, Tennessee

Approved:

Professor Ronald D. Schrimpf

Professor Sokrates T. Pantelides

Professor Daniel M. Fleetwood

Professor Robert A. Reed

Professor James E. Wittig

ABSTRACT

Gallium Nitride or GaN-based high electron mobility transistors (HEMTs) is currently the most promising device technology in several key military and civilian applications due to excellent high-power as well as high-frequency performance. Even though the performance figures are outstanding, GaN-based HEMTs are not as mature as some competing technologies, which means that establishing the reliability of the technology is important to enable use in critical applications. The objective of this research is to understand the physical mechanisms affecting the reliability of GaN HEMTs at moderate drain biases (typically $V_{DS} < 30$ V in the devices considered here). The degradation in device performance is believed to be due to the formation or modification of charged defects near the interface by hydrogen depassivation processes (due to electron-activated hydrogen removal) from energetic carriers. A rate-equation describing the defect generation process is formulated based on this assumption. A combination of ensemble Monte-Carlo (EMC) simulation statistics, ab-initio density functional theory (DFT) calculations, and accelerated stress experiments is used to relate the candidate defects to the overall degradation behavior (V_T and g_m). The focus of this work is on the 'semi-ON' mode of transistor operation in which the degradation is usually observed to be at its highest. This semi-ON state is reasonably close to the biasing region of class-AB high power amplifiers, which are popular because of the combination of high efficiency and low distortion that is associated with this configuration. The carrier-energy distributions are obtained using an EMC simulator that was developed specifically for III-V HFETs. The rate equation is used to model the degradation at different operating conditions as well as longer stress times from the result of one short duration stress test, by utilizing the carrier-energy distribution obtained from EMC simulations for one baseline condition. This work also attempts to identify the spatial location of these defects, and how this impacts the V_T shift and g_m degradation of the devices.

ACKNOWLEDGEMENTS

I would like to thank my advisor Prof. Ronald Schrimpf for accepting me in the group and giving me the opportunity to work on this fantastic project. I am extremely grateful for the guidance, encouragement and continuous financial support throughout this work. I would like to thank my co-advisor Prof. Sokrates Pantelides and Prof. Daniel Fleetwood for their guidance, criticisms and valuable inputs. I would also like to acknowledge Prof. Robert Reed and Prof. Jim Wittig for serving on my dissertation committee and providing useful comments. I am also grateful to VINSE for the IGPMS doctoral admit, and the Office of Naval Research for funding this project (through the DRIFT MURI Grant # N-00014-08-100655).

I am especially indebted to Yevgeniy Puzyrev for the inputs without which this work would be incomplete. The calm, friendly and helpful nature of Yevgeniy made the countless hours of discussion absolutely seamless. In addition, I am grateful to Jin Chen for performing the time consuming stress experiments. Also, special acknowledgements to Prof. Jasprit Singh and his team (University of Michigan) for providing access to the Monte-Carlo simulation code which is the backbone of this work, and the SSLEEC Center (UC Santa Barbara) for providing the devices. I would also like to acknowledge Aditya Kalavagunta (COMSOL) and Jean-Marie Lauenstein (NASA GSFC) for providing valuable inputs on adjacent projects, even though I never got an opportunity to meet either of them personally. I would also like to acknowledge my master's thesis advisor Prof. Leonard Trombetta (University of Houston) for initiating my interest in the field of semiconductor physics, and suggesting to try for doctoral studies.

I would like to thank all my friends, faculty and staff at RER and VUSE for their help and support, which made the last four years the most enjoyable of my academic life. The friendly, tension-free and collaborative environment at RER is a huge incentive for any graduate student. This is evident from the fact that hardly any RER student is in a hurry to leave. The academic experience at RER prepares the students to compete with the very best in the semiconductor field.

I would like to thank my industry mentors, Pejman Khosropour (Supertex/Microchip), Jim Fulford, Mark Gardner (both at Micron) and Jeff Wittich (Intel) for giving me the opportunity to intern with their respective groups, where I gained some valuable experience by being involved in cutting-edge transistor technology development. I believe the technical skill-set and the understanding of the semiconductor industry developed during these summer internships is going to help me a lot in my career in the future.

Finally, I would like to acknowledge my parents for the blessings, patience, support and constant encouragement throughout the duration of graduate studies. The numerous technical discussions and occasional arguments with my younger brother Shrijit (University of Florida and Intel) have been mutually beneficial academically as well as professionally.

TABLE OF CONTENTS

Page

ABSTRACT……………………………………………………………………………………….ii

ACKNOWLEDGEMENTS………………………………………………………………………iii

LIST OF FIGURES ………………………………………………………………………………vii

LIST OF TABLES………………………………………………………………………………....x

CHAPTER

I. INTRODUCTION 1

Background: GaN HEMT Technology……... 1
Reliability Issues in GaN-based HEMTs 5
Objective of the Proposed Research…. 6

II. TECHNOLOGY OVERVIEW: GaN HEMTS 7

GaN-HEMT Device Fundamentals 7
Device Fabrication Procedure 9
Analytical Model for a HEMT 10
Impact of Polarization Charge 12
Important Figures of Merit 13
Reliability-Limiting Mechanisms 15
The Case of ‘Semi-ON’ 17

III. PROCESS-DEPENDENCE OF DEGRADATION 19

Growth and Processing Information 19
Transistor Characteristics: Unstressed 21
Stress Experiment Results: At ‘semi-ON’ 22

IV. DEGRADATION MODELING: METHODOLOGY 25

Approach for Predictive Modeling 25
Assumptions for Simplification 26
The Rate Equation 27
Exponential Dependence of Degradation 28

V. EMC SIMULATOR DESCRIPTION….. 30

Simulator Overview: Michigan HFET 30
Simulator Formalism: EMC Approach 31
Device Structure and Composition 36

VI. EMC SIMULATION RESULTS 37

Band Diagram and Carrier Density 37
Electric Field Profiles 40
Carrier Energy Distribution: Bias-Dependence 41
Carrier Energy Distribution: Temperature-Dependence 44
Carrier Energy Distribution: Doping-Dependence 47
Carrier Energy Distribution: Geometry-Dependence 48

VII. EXTRACTION OF DEFECT SCATTERING CROSS-SECTION 51

Defect Activation Energy Calculation: Ab-Initio DFT 52
Cross-Section Calculation (σ) 56
Activation Energy (E_{act}) as a Modeling Parameter 57
Energy-Dependent Cross-Section 58

VIII. V_T DEGRADATION MODELING: BIAS-DEPENDENCE 59

Model for V_T shift: Bias-Dependence 59
Results of Predictive Modeling 60
Comparison with Experimental Data 63
Prediction for Longer Duration Stress 64

IX. V_T DEGRADATION MODELING: TEMPERATURE-DEPENDENCE 66

Model for V_T shift: Temperature-Dependence 66
Results of Predictive Modeling 67
Comparison with Experimental Data 69

X. TRANSCONDUCTANCE DEGRADATION MODELING 71

Relating g_m Degradation with V_T Shift 71
Results for Predictive Modeling 74
Comparison with Experimental Data 75
Prediction for Longer Duration Stress 77

XI. MODELING MULTIPLE-DEFECTS: V_T and TRANSCONDUCTANCE 78

The Two-Defect Model: Approach 78
Likely Defect: Substitutional Iron Complex 80
Modeling Temperature Data (for Iron) 82

XII. CONCLUSION 86

REFERENCES 90

BIOGRAPHICAL SKETCH 93

LIST OF FIGURES

Figure Page

I-1 Major military and commercial communication application areas in which GaN-based HEMTs are currently being used……………………………………………3

I-2 Overview of the design requirements, enabling features and performance advantages obtained for a wide bandgap semiconductor-based system…………………4

II-1 The cross-sectional view of AlGaN/GaN HEMT structure. The quantum well (2D Electron Gas) forms at the interface. SiC or Sapphire is usually used as the substrate material………………………………………………………………8

II-2 The band diagram of an AlGaN/GaN HEMT at $V_{GS} = 0$. The quantum well (2DEG) forms in the conduction band. The band-gap of GaN is about 3.4 eV. The band-gap of AlGaN is 4.5 eV………………………………………………………8

II-3 The combined effect of spontaneous (P_{SP}) and piezoelectric (P_{PE}) polarization fields at the AlGaN/GaN interface. There is a net positive polarization-induced charge build-up……………………………………………………………………12

II-4 Overview of all the major and minor reliability-limiting mechanisms observed in the state-of-the-art AlGaN/GaN HEMT devices. The arrows indicate the physical location where the device is affected due to the mentioned problem……...….15

II-5 Electron temperature contour plot for an AlGaN/GaN HEMT device structure subjected to semi-ON (V_{GS} = -2 V, V_{DS} = 20 V) stress at 300 K. The simulation is done using S-Device TCAD. The peak (dark red region) is at the end of the gate on the G-D access side…………………………………………………………………16

III-1 The three categories of device characterized: unpassivated rectangular gate (top), passivated rectangular gate (center) and passivated trench gate (bottom). Devices in each category were fabricated using these three processing recipes: Ga-rich, N-rich and NH_3-rich…………………………………………………...……20

III-2 The drain current (I_D-V_G) and transconductance ($\delta I_D/\delta V_G$) characteristics for a PA-MBE grown (Ga-rich) rectangular passivated gate device (for V_{DS} = 0.2 V)………21

III-3 The impact of the device temperature on the V_T of unstressed Ga-rich HEMT….……..21

III-4 $V_{pinch\text{-}off}$ shift for Ga-rich, N-rich and NH_3-rich HEMTs from the first batch of devices stressed in the semi-ON (V_{GS} = -2 V, V_{DS} = 20 V) condition………………….22

III-5 (a) V_T shift for Ga-rich HEMTs in semi-ON condition (V_{GS} = -2 V, V_{DS} = +20 V) for identical devices. (b) The corresponding transconductance (g_m) degradation ($\Delta g_m/g_m$) for the same devices……………………………………………………….…23

IV-1 Overview of our methodology for the V_T degradation modeling process. The methodology is based on the assumption that the V_T shift and g_m degradation takes place due to the build-up of charged defects near AlGaN/GaN interface. High energy carriers are responsible for the formation of these defects due to hydrogen depassivation process……………………………………………...……………26

V-1 Overview of the flow of the formalism for a simulation run using the Michigan HFET simulator……………………………………………………………...……………31

V-2 The E-k diagram for Gallium Nitride (for Wurtzite arrangement). The HFET simulator considers the non-parabolicity effects in Γ, L and U-M valleys……………..32

VI-1 Energy band diagram obtained at the gate for (a) V_{GS} = -2.0 V, V_{DS} = 20 V (b) V_{GS} = 0 V, V_{DS} = 20 V (c) V_{GS} = +2.0 V, V_{DS} = 20 V. The quantum well (2DEG) is at the AlGaN/GaN interface……………………………………………..…...38

VI-2 Electron and hole density obtained by slicing at the gate for (a) V_{GS} = -2.0 V, V_{DS} = 20.0 V (b) V_{GS} = 0 V, V_{DS} = 20.0 V (c) V_{GS} = +2.0 V, V_{DS} = 20.0 V (d) V_{GS} = -2.0 V, V_{DS} = 30.0 V. The peak is at the AlGaN/GaN interface…………...…39

VI-3 Parallel electric field as a function of channel position for different V_{GS} values at 300 K for V_{DS} = 20.0 V. The gate extends from 0.35 µm to 0.4 µm………………..…..40

VI-4 Perpendicular electric field as a function of channel position for different V_{GS} values at 300 K for V_{DS} = 20.0 V. The gate extends from 0.35 µm to 0.4 µm…………40

VI-5 Carrier energy distribution for different gate bias values at 300 K for V_{DS} = 20 V sliced at the end of gate on G-D access region side (0.4 µm)……………………...…..42

VI-6 (a) Carrier energy distribution for V_{GS} = -2.0 V, V_{DS} = 20 V (300 K) obtained by slicing at different points along the channel. (b) The total number of carriers at each slicing point compared with the number of energetic (E > 2 eV) carriers at the corresponding point………………………………………………………….……...43

VI-7 (a) Carrier energy distribution for different temperatures in semi-ON state (V_{GS} = -2.0 V, V_{DS} = 20.0 V) condition sliced at the end of the gate on the Gate-Drain access region side. (b) Close-up view of the high energy carrier distribution region (greater than 2 eV) of Fig VI-7. (a)…………………………...……45

VI-8 (a) Carrier energy distribution for different GaN and AlGaN donor density in the semi-ON (V_{GS} = -2 V, V_{DS} = 20 V) condition sliced at the end of the gate on the G-D access side. (b) Close-up view of the high energy carrier distribution region (greater than 2 eV) of Fig VI-8. (a)……………………………………….………47

VI-9 Carrier energy distribution for different device geometry (access lengths) in the semi-ON (V_{GS} = -2 V, V_{DS} = 20 V) condition sliced at the end of the gate on the G-D access region side……………………………………………………………….48

VI-10 Carrier energy distribution for different drain bias values for V_{GS} = -2.0 V, sliced at the end of the gate on the G-D access region side…………………..………...49

VI-11 Comparison of high energy (E > 1.8 eV), medium energy (E > 0.5 eV) and the total number of carriers obtained for different drain bias conditions obtained at V_{GS} = -2.0 V, sliced at the end of the gate on the G-D access region side……….......50

VII-1 (a) Atomic configuration and the corresponding migration energy barrier of a doubly hydrogenated Ga vacancy in GaN. The red line highlights the H removal path and energy barrier along the path. (b) Atomic configuration and barrier of hydrogenated substitutional oxygen in AlGaN. The red arrow shows the removal of H to the next cell. The barrier is calculated along the path between initial and final positions of the H……………………………………………...……..54

VII-2 (a) Energy barrier for electron-activated removal for hydrogen in GaN from first-principles DFT calculations using VASP. The figure shows the atomic configuration of hydrogenated substitutional O, with Al atoms shown in dark blue. The red circle shows the position of H. The barrier is calculated along the path between initial and final positions of the H. The activation barrier for initial step of removal process is 0.5 eV. (b) Barrier and defect reconfiguration for H to move further from O. The barrier for this complete removal is 2.1 eV……..…55

VII-3 Exponential fits to the semi-ON stress (V_{GS} = -2 V, V_{DS} = 20 V) results for three Ga-rich devices, and the corresponding extracted cross-section values………….56

VII-4 Extracted scattering cross-section values from the fit to Device # 3 (Ga-rich) semi-ON data for eight hypothetical defects with different activation energies………..57

VII-5 Impact on the extracted cross-section values from fit to Device # 3 semi-ON stress data when the cross-section is assumed to be energy-dependent………………...58

VIII-1 The V_T shift predictions (for the N-rich devices) obtained for different values of V_{GS} at 300 K (for V_{DS} = 20 V). The predictions are based on the scattering cross-section value obtained from the exponential fit to semi-ON (V_{GS} = -2 V) stress experiment data (black)…………………………………………………….…61

VIII-2 The V_T shift predictions (for the Ga-rich devices) obtained for different values of V_{GS} at 300 K (for V_{DS} = 20 V). The predictions are based on the scattering cross-section value obtained from the exponential fit to semi-ON (V_{GS} = -2 V) stress experiment data (black)…………………………………………………….……62

VIII-3 The values of summation of product of number of carriers and their velocities obtained for different values of V_{GS} considering six hypothetical defects with different activation energies…………………………………………………………..…62

VIII-4 Comparison of experimental results (for V_{GS} = 20 V) with V_T shift predictions (N-rich devices) obtained for different values of V_{GS} at 300 K…………………...…....63

VIII-5 Long duration V_T shift prediction (Ga-rich) obtained for semi-ON (V_{GS} = -2 V) at 300 K (V_{DS} = 20 V). The predictions are based on the scattering cross-section value obtained from the fit to the first 10 hours of the stress test data……………...…64

IX-1 The values of summation of product of number of carriers and their velocities obtained for the different values of temperature considering six defects with different activation energies……………………………………………………….…..67

IX-2 The density of precursor defects (N_d^{∞}) for different device temperatures for Ga-rich devices obtained from the V_T values for the corresponding temperature……….68

IX-3 The values of summation of product of number of carriers and their velocities obtained for the different values of temperature considering six defects with different activation energies…………………………………………………….……..69

IX-4 The V_T shift predictions (for Ga-rich devices) obtained for different temperatures at semi-ON (V_{GS} = -2 V, V_{DS} = 20 V) compared with the experimental data for the corresponding temperature. The predictions are based on the cross-section value obtained from the exponential fit to the room temperature stress test data (green) considering an E_{act} of 0.6 eV…………………………………………………….…….69

IX-5 The V_T shift predictions (for Ga-rich devices) obtained for different temperatures at semi-ON compared with the experimental data for the corresponding temperature. The predictions are based on the scattering cross-section value obtained from the exponential fit to the 300 K stress experiment data (green) considering an activation energy of 2.1 eV……………………………………………………………………..…...70

X-1 The best fit obtained by scaling the V_T shift exponential fit to the semi-ON stress at 300 K to match the corresponding g_m degradation data at semi-ON (at 300 K)……….72

X-2 The g_m degradation predictions (Ga-rich) obtained for different temperatures at semi-ON (V_{GS} = -2 V, V_{DS} = 20 V) compared with the experimental data for the corresponding temperature. The predictions are based on the value of α obtained scaling the V_T exponential fit to the 300 K g_m data (green) from the semi-ON stress experiment…………………………………………………………….75

X-3 The long duration g_m degradation prediction (Ga-rich) obtained for V_{GS} = -2 V at 300 K (for V_{DS} = 20 V). The prediction is based on the scattering cross-section value obtained from the exponential fit to the first 10 hours of stress experiment data (Fig (a)), and carrier scattering factor obtained from scaling the V_T shift to match semi-ON g_m degradation data at 300 K, again for 10 hours (Fig (b))………..…...76

X-4 The long duration g_m degradation prediction (Ga-rich) obtained for V_{GS} = -2 V at 300 K (for V_{DS} = 20 V). The prediction is based on the scattering cross-section value obtained from the exponential fit to the first 10 hours of stress experiment data (Fig (a)), and the carrier scattering factor obtained from scaling the V_T shift to match semi-ON g_m degradation data at 300 K, again for 10 hours (Fig (b))…………..…76

X1-1 The best fit to the V_T shift and g_m degradation data at 400 K using the two-defect exponential model. The related contributions due to each defect activation energy has been also represented for both V_T and g_m………………………………………..……80

X1-2 Atomic configurations are shown above corresponding migration energy barriers of H removal from iron impurity. Red circles show the positions of Fe (in brown) and H. Arrows connect initial and final H positions. These positions correspond to the initial and final points of the distance axis in the migration energy plots. N atoms are shown in blue, Ga atoms are shown in green. (a) H migration near Fe_{Ga} with the barrier of 0.6 eV. (b) Defect configurations of H migration near Fe-V_N with barrier of 1.4 eV……………………………………………………………………...81

X1-3 The V_T shift data for the devices stressed at semi-ON for different temperatures modeled using two-defect model, with activation energies of 0.6 eV (initial barrier) and 1.4 eV (for the complete removal of H)………………………………………….......83

X1-4 Fits to the transconductance degradation ($\Delta g_{m}/ g_m$) data for the devices stressed at semi-ON (V_{GS} = -2 V, V_{DS} = 20 V) for different temperatures using the two-defect model, with defect activation energies of 0.5 eV and 1.8 eV……………………...……...84

LIST OF TABLES

Table Page

I-1 Comparison of important performance figures of major technologies in the power electronics domain……….2

VI-1 Number of carriers above a given energy level for different values of V_{GS} with V_{DS} = 20 V……….43

VI-2 Number of carriers above a given energy level for different temperatures at semi-ON (V_{GS} = -2 V)……….46

VIII-1 Density of benign defects at t = 0, and the calculated values of time constants for different values of V_{GS} with V_{DS} = 20 V……….63

IX-1 Density of benign defects at t = 0, and the calculated values of time constants for different device operating temperatures……….68

XI-1 Calculated time constants at different temperatures for the defect activation energies of 0.6 eV and 1.4 eV, respectively. The time constants for 400 K are obtained directly from the two-activation-energy fit to the 400 K stress data……….84

XI-2 Concentrations of available pre-existing defects at different temperatures for the defect activation energies of 0.6 eV and 1.4 eV respectively, obtained from the exponential fits to the data of Fig I-1……….85

CHAPTER I

INTRODUCTION

Over the last two decades, the Gallium Nitride (GaN) material system has established itself as extremely important for the next generation microwave/RF communication, power electronics, opto-electronics and microelectromechanical systems application areas. GaN-based HEMTs have become attractive for very high efficiency microwave systems as well as power management applications. GaN HEMTs are expected to replace existing technologies like Gallium Arsenide (GaAs), Silicon Carbide (SiC) and Silicon-based Double-Diffused MOS (DMOS) in several key military and civilian application areas in the next few years [1].

1.1 Potential for Gallium Nitride Technology

Historically, GaN was one of the first III–V compound semiconductors to be studied. First reports on the epitaxy of GaN by halide vapour phase epitaxy date back to the year 1969. Due to the non-availability of a single crystalline GaN substrate, GaN films were typically deposited on sapphire substrates. Although years of intensive studies on GaN growth and its properties followed, the interest declined in the early 1980s, as several severe problems, preventing the utilization of GaN in electronic and opto-electronic devices, seemed to be impossible to overcome: the GaN films suffered from a very high n-type background carrier concentration and no p-type doping could be achieved. In the late 1980s high quality GaN films on sapphire substrates were reported in a two-step growth process, which resulted in a dramatic improvement of both the structural and the electrical properties of the GaN films. A broad range of GaN-based electronic devices has been realized, including high electron mobility transistors (HEMTs), heterojunction bipolar transistors (HBTs), bipolar junction transistors (BJTs), Schottky and pin rectifiers and metal oxide semiconductor field effect transistors (MOSFETs) [1]-[3].

The first AlGaN/GaN HEMT was demonstrated by Prof. M. Asif Khan and his group in 1994 [4]. GaN-based HEMTs have been available commercially in the US since 2006, and have gained considerable popularity because of excellent high-power and high-frequency performance achieved at very high efficiency. The promise of electronic applications is primarily in the area of sources and amplifiers for communications and low loss switches in power conditioning applications. This performance can be attributed to a combination of extremely high breakdown field, high saturation velocity and excellent high temperature performance. Table I-1 lists the performance figures of all the major technologies competing in the power electronics space. In most categories, GaN-based devices excel over other technologies. The last two rows summarize the resulting performance advantages at the system level and to the customer. The highlighted features offer the most significant product benefits. The high power per unit width translates into smaller devices that are not only easier to fabricate but also offer much higher impedance. This makes it easier to match them to the system, which is often a complex task with conventional devices in GaAs (e.g., a matching ratio 10 times larger might be needed for a standard GaAs transistor, increasing the overall complexity for the design engineers). Today, the state-of-the-art AlGaN/GaN HEMTs (grown on SiC substrates) exhibit an output power density as high as 50 W/mm [3], [5].

TABLE I-1

Comparison of the important performance figures of major technologies competing in the power electronics and RF communication applications domain [1].

Technology:	Si (LDMOS)	GaAs	SiC	GaN	Diamond
E_g (eV)	1.12	1.42	3.26	3.39	5.45
n_i (cm^{-3})	1.5×10^{10}	1.5×10^{6}	8.2×10^{-9}	1.9×10^{-10}	1.6×10^{-27}
ε_r	11.8	13.1	10.1	9.0	5.5
μ_n (cm^2/Vs)	1350	8500	700	2000	1900
v_{sat} (10^7 cm/s)	1.0	1.0	2.0	2.5	2.7
E_{br} (MV/cm)	0.3	0.4	3.0	3.3	5.6
JFOM i.e. $E_{br}\, v_{sat} / 2\pi$	1.0	2.7	20.0	27.5	50.0
BFOM i.e. $\varepsilon\, \mu\, E_g^3$	1.0	16	134	637	3900

The excellent high-power and high-frequency performance makes GaN HEMT-based microwave power amplifiers and switches suitable for numerous military applications like state-of-the-art active phase array radar, communication jammers, missile guidance electronics and non-lethal systems like directed-energy weapons. GaN-based HEMTs can amplify high power radio frequency signals at microwave frequencies very efficiently. This result in greater sensitivity for an antenna array, which means it can detect and track objects at longer distances. Also the size of the antenna can be reduced without compromising performance, greatly improving transportability. The wide band gap of GaN provides a large critical breakdown field, increasing the maximum operating voltage, whereas the higher drain current that GaN-based HEMTs offer makes the broadband matching of high-power MMICs and RF amplifiers simpler and more efficient than the competing technologies. The high thermal conductivity of the material also enables more efficient amplifier cooling, which makes these devices suitable for applications in harsh environments [3], [6], [7].

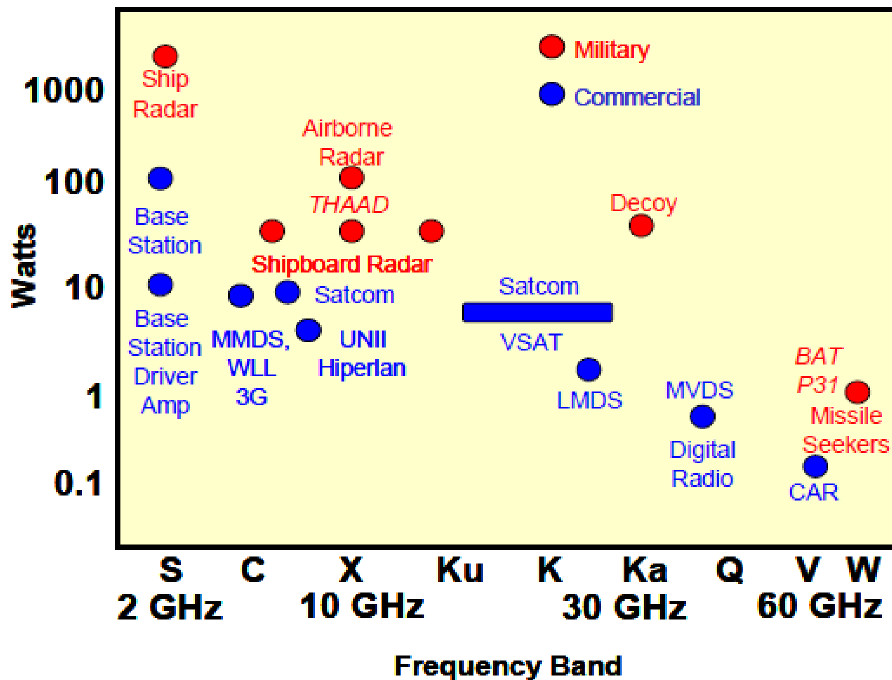

Fig. I-1. Major military and commercial communication application areas in which GaN-based HEMTs are currently being used or will be used in the near future. AlGaN/GaN HEMTs are more suitable for the applications in which higher power density is desirable [3].

On the civilian applications side, GaN electronics are becoming more common in ultra-wideband communication systems like cellular base-station trans-receivers, satellite communications and television broadcasting systems. Since these systems operate at higher power and higher frequency than competing technologies, they allow a smaller antenna size for the terminal users. Increased power and frequency of GaN HEMTs also improves the data transmission rate of broadband wireless internet connections. The faster switching of GaN devices compared to the competing technologies also results in comparatively more efficient power conversion. Hence, gallium nitride transistors are also finding use in applications like compact DC-DC conversion systems, AC motor drives, mobile battery chargers, and switched mode power supplies. Fig. I-2 gives an overview of the design needs, the enabling features and the performance gains that we can expect from a given technology.

Need	Enabling Feature	Performance Advantage
High Power/Unit Width	Wide Bandgap, High Field	Compact, Ease of Matching
High Voltage Operation	High Breakdown Field	Eliminate/Reduce Step Down
High Linearity	HEMT Topology	Optimum Band Allocation
High Frequency	High Electron Velocity	Bandwidth, μ-Wave/mm-Wave
High Efficiency	High Operating Voltage	Power Saving, Reduced Cooling
Low Noise	High gain, high velocity	High dynamic range receivers
High Temperature Operation	Wide Bandgap	Rugged, Reliable, Reduced Cooling
Thermal Management	SiC Substrate	High power devices with reduced cooling needs
Technology Leverage	Direct Bandgap: Enabler for Lighting	Driving Force for Technology: Low Cost

Fig. I-2. Overview of the design requirements, enabling features and the corresponding performance advantages obtained for a wide bandgap semiconductor-based system [1].

The best performance figures obtained (till 2013) from GaN-based HEMTs are as follows [6]:

- Maximum operating frequency (F_{max}): 450 GHz
- Breakdown Voltage (BV): 750 V
- Maximum operating temperature: 800 C
- Power Density: 60 W/mm

1.2 Reliability Issues in GaN HEMTs

Thanks to the recent advances in the growth and processing of GaN HEMTs, it is now possible to fabricate devices with cut-off frequencies in excess of 400 GHz, and output power densities in excess of 50 W/mm. However, the reliability of AlGaN/GaN HEMTs is still a very big challenge. Major transistor performance issues observed in the state-of-the-art GaN-based HEMTs include current collapse, gate-lag effects, second virtual gate, transient phenomena, buffer trapping, leakage, and the gate-sinking issue [5], [8].

One of the biggest reliability issues is the reverse-bias permanent degradation of these transistors at high drain bias (typically V_{DS} > 30 V). HEMTs subjected to reverse-bias stress may show a sudden increase in gate current due to the formation of defect-related conductive paths. This type of degradation is usually ascribed to inverse-piezoelectric effects or to the generation (or percolation) of defects close to the gate. It has been suggested that there is a 'critical (gate-drain) voltage' beyond which the gate diode of the AlGaN/GaN HEMT begins to degrade. Hence, the degradation depends on the electric field. Recent reports have suggested that the reverse-bias permanent degradation is also possible at a bias less than the 'critical voltage' if the duration of the electrical stress is sufficiently large [8], [9].

The understanding of the reverse-bias or the 'OFF-state' reliability has been steadily improving over the years. Special designs such as drain field plates and recessed gate structures are regularly used to improve the reliability without impacting the transistor performance. The processes responsible for the 'semi-ON-state' degradation at moderate drain bias have not been completely identified, however. It has been suggested that high energy or hot electrons may be responsible for this. 'Semi-ON-state' is the transition region between the pinch-off and completely ON region of the transistor characteristics. Hot carriers can result in the formation of traps or activation of defects by transferring energy to the lattice. This may result in shifting of the V_T and gradual degradation of drain current and peak g_m of the device. The impact of hot carriers in influencing the degradation kinetics has not been completely understood [5], [9].

1.3 Objective of Proposed Research

The objective of this research is to understand the physical mechanisms affecting the reliability of AlGaN/GaN HEMTs at moderate drain biases ($V_{DS} < 30$ V). In these conditions, the degradation in the device performance is believed to be due to the formation or modification of charged point defects near the interface by high energy electrons (electron-activated hydrogen removal). A rate-equation describing the defect generation process with respect to stress time is formulated based on this assumption. A predictive model is introduced that uses a combination of EMC simulation statistics, ab-initio DFT calculations and accelerated stress experiments. The model can be used to help determine the type of defect as well as describe the overall degradation behavior (e.g., the V_T shift and the reduction in g_m). The model developed predicts the device degradation at longer stress times as well as different operating conditions (like bias and temperature) from a single short duration stress test, by utilizing the carrier-energy statistics obtained from the EMC simulations, as long as the defects present in the device are properly identified. The carrier-energy distribution determined from the EMC simulations is obtained at the location in the device where the maximum degradation due to the high energy carriers is expected. The focus of this work is the 'semi-ON' mode of operation in which the degradation is usually observed to be at its highest for moderate drain bias values.

CHAPTER II

TECHNOLOGY OVERVIEW: GALLIUM-NITRIDE HEMT

This chapter provides a technological overview of AlGaN/GaN HEMTs. It covers the basics of device operation, an analytical model of the 2DEG density, some important figures of merit, and reliability issues. The chapter also introduces the concept of 'semi-ON' state degradation, which is the primary focus of this research.

2.1 GaN-HEMT Device Fundamentals

A High Electron Mobility Transistor (HEMT), also known as a Heterostructure FET (HFET), or a Modulation-Doped FET (MODFET) is field-effect device that utilizes the difference in band-gap of two materials to create a potential well in which carriers can flow from source to drain. MOSFETs, on the other hand, rely on transport in the doped region under an MOS capacitor gate where an inversion layer forms. The carriers in the inversion layer are slowed down by scattering from the dopant atoms, which limits the peak mobility as well as the saturation velocity of these carriers and decreases the switching time. This makes Si MOSFETs unsuitable for very high frequency applications. HEMTs avoid this problem as the carrier transport takes place in a quantum well (2D Electron Gas layer) formed at the heterojunction of two wide band-gap materials. The quantum well in the conduction band is formed due to the band-gap difference of the two materials. The doping of the material in which the 2DEG is formed is extremely low. The quantum well provides a very low resistance path as there is very little collision of electrons with the impurity atoms. This significantly increases the switching speed and the cut-off frequency of the transistor. In GaN-based HEMTs, the carrier density is even higher due to the impact of spontaneous and piezoelectric polarization [2].

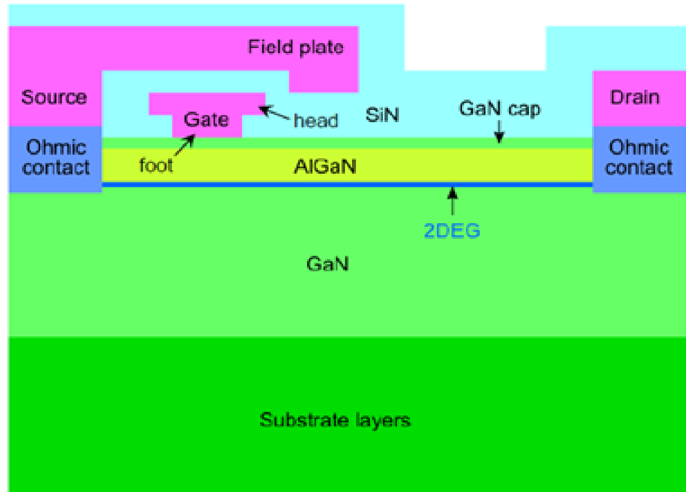

Fig. II-1. The cross-sectional view of AlGaN/GaN HEMT structure. The quantum well (2DEG) forms at the interface. SiC or Sapphire is usually used as the substrate material [10].

The cross-sectional view of a typical AlGaN/GaN HEMT device is shown in Fig. II-1. The material of choice for the gate metal is an alloy of nickel, gold and platinum. Silicon-carbide and sapphire are usually used as the substrate materials. Some recently developed devices use silicon as the substrate [14]. The AlGaN layer has a GaN cap, and the entire layer is covered with SiN for passivation. The field-plates are introduced to reduce the peak electric field at the gate-edge and improve the reliability of the devices. Fig. II-2 shows the energy band diagram of the device above, obtained vertically at the gate. The quantum well (2DEG layer) is formed at the heterojunction even without application of gate bias. Hence, GaN-based HEMTs are typically depletion mode devices.

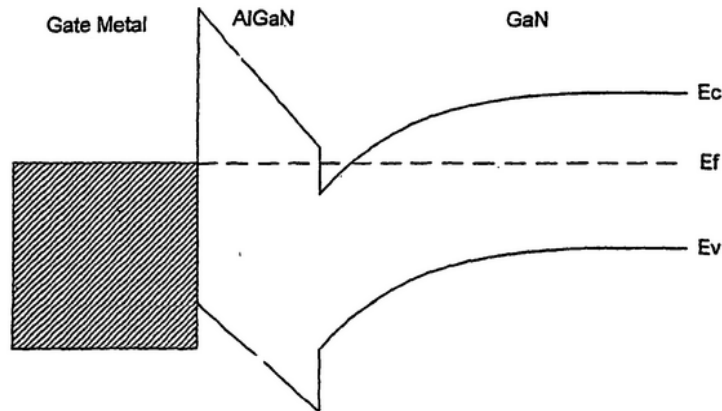

Fig. II-2. The band diagram of an AlGaN/GaN HEMT at $V_{GS} = 0$. The quantum well (2DEG) forms in the conduction band. Band-gap of GaN = 3.4 eV. Band-gap of AlGaN = 4.5 eV.

2.2 Device Fabrication Procedure

The precise application of the HEMTs determines the selection of the substrate material. The lack of a Gallium Nitride substrate necessitates heteroepitaxy on compatible substrates. Sapphire (Al_2O_3) is semi-insulating, can withstand high growth temperatures and is relatively inexpensive. On the down side, sapphire has very low thermal conductivity, large lattice mismatch and relatively large coefficient of thermal expansion. Silicon carbide on the other hand has a high thermal conductivity, low lattice mismatch as well as mismatch due to coefficient of thermal expansion. But it is quite expensive and has a large density of crystallographic defects. Silicon is low cost, available in large diameter wafers and easy to integrate due to existing silicon fabs. But the lattice mismatch as well as the coefficient of thermal expansion is extremely large.

The epitaxial layers are grown on the substrates by Molecular Beam Epitaxy (MBE) or Metal-Organic Chemical Vapor Deposition (MOCVD) techniques. With sapphire as a substrate, the nucleation layer consists of GaN or AlN deposited at a low temperature (typically 600 ºC), which is then heated up to the growth temperature of the main layer. The GaN and AlGaN layers are typically grown at 1000 ºC at growth rates of ~ 1µm/h. Nucleation on SiC layer is typically performed using AlN growth at around 900 ºC . The physical effect that dominates the device behavior as well as the defect density is the polar nature of the GaN and AlGaN. The Ga-face GaN is the preferred polarity for growing high quality devices [1]-[4].

The first step of the typical device fabrication process is the definition of the active device area. This is determined by Cl_2 mesa etching or by ion implantation. The Ohmic contacts are made by partially etching the AlGaN in the source and drain regions and depositing the alloy and annealing at 900 ºC . Ti/Al/Ni/Au is the preferred material for Ohmic contacts. The gate is defined by lift-off of Ni/Au metallurgy and obtained by optical stepper lithography. The final step is the deposition of a passivation layer like SiN. This layer serves a critical purpose in eliminating dispersion between the large signal AC and the DC characteristics of HEMTs.

2.3 Analytical Model for a HEMT

The analytical model considered here was developed initially for a general HEMT device, and the effect of piezoelectric polarization has been added to model the 2DEG density for a GaN HEMT more accurately. The conduction band discontinuity at the interface creates a potential well which confines the 2DEG. The potential well is assumed to have only two quantum levels, E_0 and E_1, which are relevant for the operation of the device (other levels are always above the Fermi level). A self-consistent solution to the Poisson and Schrödinger equation gives us the 2DEG density. The 2DEG density (cm^{-2}) in terms of energy levels is as follows [1], [2], [11]:

$$n_s = DkT\left\{\left[1+exp\left(\frac{E_F-E_0}{kT}\right)\right]\left[1+exp\left(\frac{E_F-E_1}{kT}\right)\right]\right\} \qquad (\text{II}-1)$$

D is the density of states in the potential well. Now, the 2DEG density (in the quantum well) at the AlGaN/GaN interface is given by:

$$n_s = \frac{\varepsilon}{qd}\left(V_{GS}-V_T-\frac{E_F}{q}\right) \qquad (\text{II}-2)$$

where V_{GS} is the gate voltage, V_T is the threshold voltage, E_F is the Fermi level and d is the thickness of the AlGaN between the Schottky gate and the 2DEG layer. The complete expression for the the threshold voltage is as follows:

$$V_T = \phi_B - \Delta E_C - \frac{qN_D d^2}{2\varepsilon} - \frac{\sigma d}{\varepsilon} \qquad (\text{II}-3)$$

where Φ_B is the barrier height at the Schottky/AlGaN junction, ΔE_C is the conduction band discontinuity at the AlGaN/GaN interface, and σ is the polarization charge density. The charge is formed at the AlGaN/GaN or the AlN/GaN interface due to the highly polar nature of the GaN material system. In weak inversion, the Fermi level is below the allowed energy states. The carrier density is small in the 2DEG. This Fermi energy and the 2DEG density can be given as,

$$E_F = kT\,ln\left(\frac{n_s}{2DkT}\right) \qquad (\text{II}-4)$$

$$n_s = 2DkT\,exp\left(\frac{q(V_{GS}-V_T)}{kT}\right) \qquad (\text{II}-5)$$

Beyond weak inversion, the sheet carrier density becomes higher as the Fermi level is much higher in the quantum well. The V_T is usually defined as the beginning of the strong inversion region. The sheet carrier density and the Fermi level close to the pinch-off (arrival of strong inversion) is given by:

$$E_F = \frac{n_s}{2D} \quad \text{(II} - 6\text{)}$$

$$n_s = \frac{2\varepsilon q D}{\varepsilon + 2q^2 D d}(V_{GS} - V_T) \quad \text{(II} - 7\text{)}$$

The HEMT is a field effect transistor, and once the 2DEG is formed the current is controlled by the channel potential $V_c(x)$. The channel current is given by:

$$I = q n_s(x) W v(x) \quad \text{(II} - 8\text{)}$$

where W is the gate width and $v(x)$ is the electron velocity at location x. The velocity of the carrier is dependent on the electric field. At very high fields the velocity reaches its saturation value (v_s). Below this limit, the velocity is limited by mobility. For electric fields less than the critical field, the current can be written as:

$$I = \mu W \frac{\varepsilon}{d}(V_{GS} - V_C(x) - V_T)\frac{dV_C}{dx} \quad \text{(II} - 9\text{)}$$

In the linear region of operation, the last term can be approximated, and the above current expression can be rewritten as follows:

$$I = \mu W \frac{\varepsilon}{d}(V_{GS} - V_T)\frac{V_C(L) - V_C(0)}{L} \quad \text{(II} - 10\text{)}$$

where L is the channel length of the device. The above expression can be modified to include the effects of the source and drain resistances (R_S and R_D):

$$\frac{V_{DS}}{I_{DS}} = R_S + R_D + \frac{Ld}{\mu W \varepsilon (V_{GS} - V_T)} \quad \text{(II} - 11\text{)}$$

The above expression is very useful is extracting important information from the I-V characteristics but it does not take into account the detailed effect of polarization charge.

2.4 Impact of Polarization Charge

The presence of polarization charge at the interface is one important difference between GaN-based HEMTs and other HFET devices. GaN and AlN are highly polar in nature. These materials exhibit strong polarization-induced fields when in contact. The polarization effects can be classified into spontaneous polarization and piezoelectric polarization. Spontaneous polarization refers to the built in polarization field present in an unstrained crystal. This field exists because the crystal lacks inversion symmetry and the bond between the two atoms is not purely covalent. This results in a displacement of the electron cloud towards one of the atoms in the bond. Thus, along the direction in which the crystal lacks inversion symmetry, the asymmetric electron cloud leads to a net positive charge on one face of the crystal and a net negative charge on the other. Piezoelectric polarization is the polarization field that results from the distortion of the crystal lattice. Due to the differences in lattice constants of AlN, GaN, and AlGaN, growing AlGaN on GaN leads to compressive strain in AlGaN. This strain results in a charge sheet at the two faces of the crystal. Fig. II-3 shows the combined piezoelectric (P_{PE}) and spontaneous (P_{SP}) electric fields in a structure with an $Al_xGa_{1-x}N$ layer grown on GaN. The polarization field increases with the Al content (mole-fraction) in the AlGaN. Thus, HEMT structures with AlN on GaN have very large polarization fields [1], [10], [12].

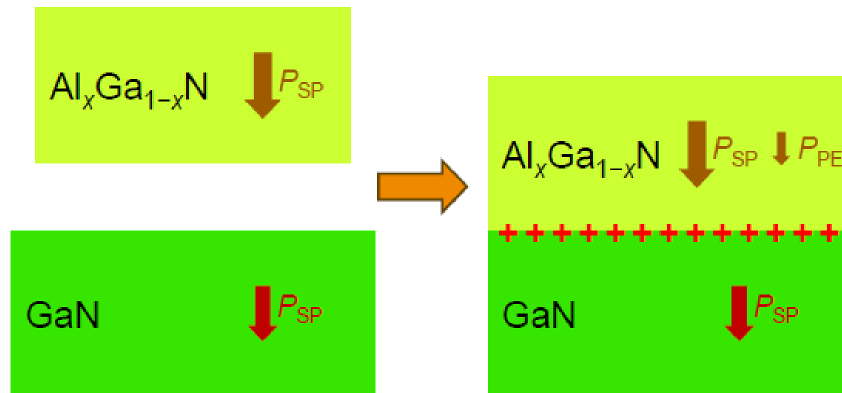

Fig. II-3. The combined effect of spontaneous (P_{SP}) and piezoelectric (P_{PE}) polarization fields at the AlGaN/GaN interface. There is a net positive polarization-induced charge build-up [10].

The 2DEG is formed in the GaN buffer layer even if there is no intentional doping in the AlGaN layer. The effect of doping in the AlGaN is negligible on the 2DEG density. The analytical relation between the 2DEG density and the barrier potential (at the interface) and other parameters in the HEMT is summarized by the following equations:

$$\phi_B = -\frac{qn_s t_1}{\varepsilon} + \frac{q(\sigma_{AlGaN} - n_s)t_2}{\varepsilon} - \frac{qn_s d_0}{\varepsilon} \quad \text{(II} - 12)$$

$$n_s = \frac{\sigma_{AlGaN} t_2 - \frac{\varepsilon \phi_B}{q}}{t_1 + t_2 + d_0} \quad \text{(II} - 13)$$

Here n_s is the 2DEG density in the channel, σ_{AlGaN} is the net polarization charge density of the AlGaN, t_1 is the thickness of the AlGaN cap layer, t_2 is the thickness of the AlGaN layer and d_0 is the distance between the centroid of the 2DEG and the top UID-AlGaN/GaN interface. The equations indicate that there is no doping dependence of the polarization charge.

2.5 Small and Large Signal Figures of Merit

It is important to understand the behavior of devices at higher frequencies, both in small and large signal operation. The former refers to applications such as low noise amplifiers in receivers whereas the latter refers to applications such as power amplifiers used in transmitters. In this context, several figures of merit can be defined to characterize the device performance. The most important figure of merit is the current gain cut-off frequency (f_T), which is proportional to the inverse of the electron transit time across the device as follows [2], [3]:

$$f_T = \frac{g_m}{2\pi C_G} = \frac{1}{2\pi t_{tr}} \quad \text{(II} - 14)$$

where t_{tr} represents the transit time of the electrons through the channel. The frequency response is therefore improved by using materials with better transport properties and shorter channel lengths. If the carriers are moving at a saturated velocity then the transit time is given by,

$$t_{tr} = \frac{L}{v_S} \quad \text{(II} - 15)$$

The current gain cut-off frequency is the primary indicator of the average electron velocity through the transistor and detailed analysis can extract the electron velocity in regions of the transistor. The power gain cut-off frequency of the device (f_{max}) is evaluated with the output of the device presented with the complex conjugate of its output impedance to maximize power transfer. This gain is predominantly dependent on the device as the termination and is determined uniquely by the device characteristic. The power gain cut-off frequency is given by:

$$f_{max} = \frac{f_T}{2\sqrt{R_i/R_{ds}}} \qquad (\text{II}-16)$$

The transistor provides the maximum power gain when both the input and the output are conjugate matched to the generator and load impedance, respectively. The maximum available power gain (*MAG*) is related to the power gain cut-off frequency as follows:

$$MAG = \frac{g_m^2 R_{ds}}{16\pi^2 f^2 C_{gs}^2 R_i} \qquad (\text{II}-17)$$

In power amplifiers a load line match is usually provided at the output rather than a match for the maximum available power gain (*MAG*). The corresponding large signal power gain (*LSG*) is then given by the equation:

$$LSG = \left(\frac{V_{br}-V_k}{V_p}\right)\frac{G_m}{4\pi^2 f^2 C_{gs}^2 R_i} \qquad (\text{II}-18)$$

An important limitation called the power-frequency limit relates to the inherent limit on the breakdown voltage a high frequency device technology can achieve. This limits the output power that can be obtained from a given technology. This limit imposes particularly severe performance limits on broadband microwave power amplifiers. This limit can be given as,

$$f_T V_{br} < \frac{E_{max} v_{sat}}{\pi} \qquad (\text{II}-19)$$

which is purely dependent on the material parameters. So, the transistor f_T and V_{br} need to be traded against each other, by utilizing the length of the drift region of the device.

2.6 Reliability-Limiting Mechanisms

Even though the performance figures of GaN-based HEMTs are exceptional, there are several major reliability-limiting issues which lower the life-time of these devices. Fig. II-4 presents some important degradation issues and indicates the physical location of the related problem, which hampers the reliability of these devices. Degradation of these devices has been reported in all three modes of operation: ON, OFF and semi-ON. The modes of operation will be discussed in details later. The degradation is limited in the ON state of operation, irrespective of the drain bias. Limited degradation is observed in the OFF state of operation when the drain bias is low. But, at higher values of drain bias (V_{DS} > 30 V) there is a large and irreversible degradation in the OFF state. For moderate and low values of V_{DS}, we observe significant degradation of the devices in the semi-ON state. The major transistor performance issues include current collapse, gate-lag effect, second virtual gate, transient phenomenon, buffer trapping, gate/edge leakage and the gate-sinking issue. Punch-through, vertical leakage, high field charge injection, forward turn-on and parasitic breakdown effects have also been reported in some of these devices [8], [13], [14].

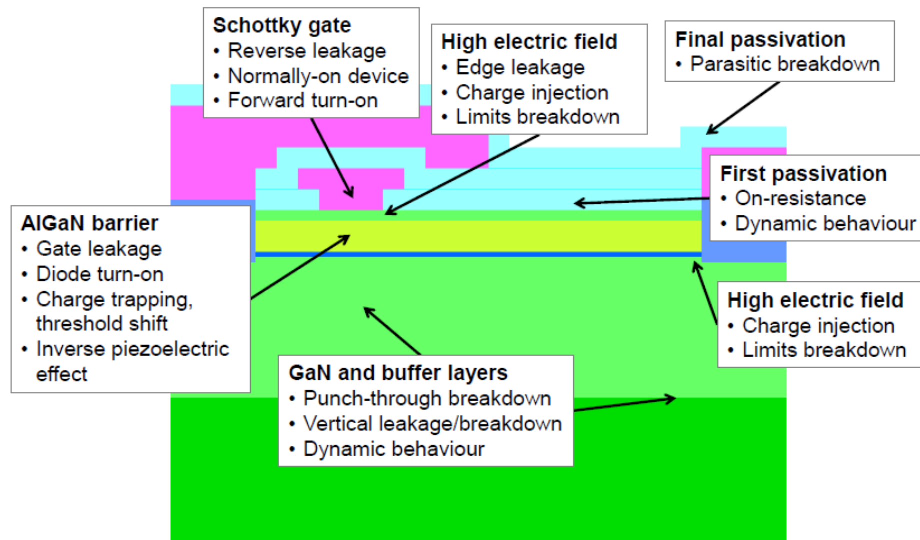

Fig. II-4. Overview of all the major and minor reliability-limiting mechanisms observed in the state-of-the-art AlGaN/GaN HEMT devices. The arrows indicate the exact physical location where the device is affected due to the mentioned problem [10].

At high values of drain bias, the OFF state degradation is due to inverse piezoelectric polarization effects. Both GaN and AlGaN are strongly piezoelectric materials. In response to the high voltages, large stresses are introduced inside these materials. A large electric field appears under the gate edge across the barrier. This can result in large mechanical stress concentrated in a small region of the AlGaN barrier. To make matters worse, due to their lattice mismatch, AlGaN on GaN is typically under substantial tensile strain and therefore stores a sizeable amount of elastic energy at rest. Under electrical stress, if the elastic energy exceeds a critical value, crystallographic defects are formed. These defects are electrically active and may affect the device characteristics in a profound way. Another mechanism that may contribute to the degradation of GaN devices biased in the OFF state is electrons injected from the gate into the GaN due to trap-assisted tunneling. These electrons can reach very high energies and can damage the surface and interfaces, as well as induce traps [15]-[18].

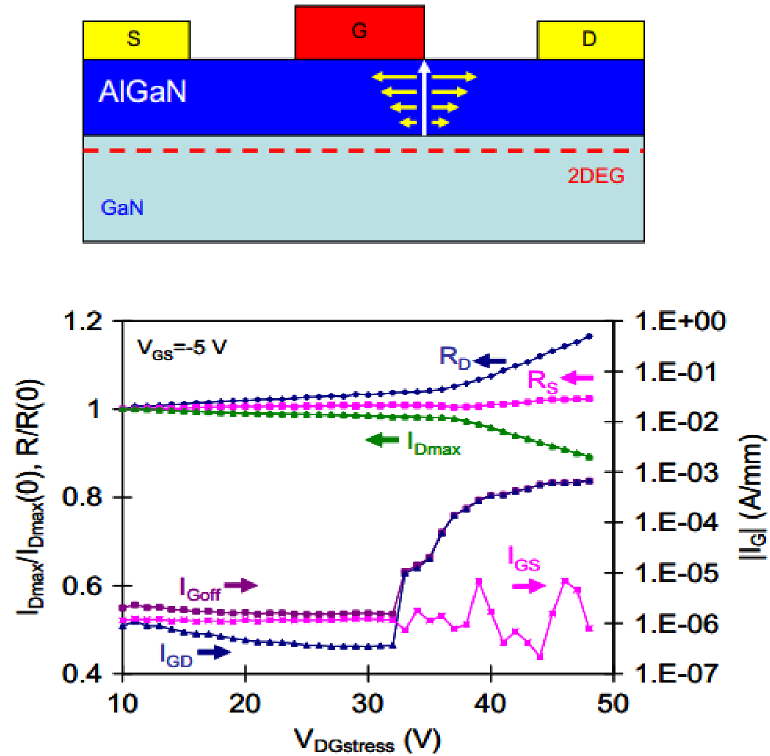

Fig. II-5. (Top) Representation of high-field on the gate-edge and a large tensile stress in a GaN HEMT with a high V_{DS} applied. (Bottom) The change in I_{Dmax}, R_D, R_S and I_{Goff} in an OFF-state step-stress experiment with increasing V_{DG} (for V_{GS} = -5 V) [15].

2.7 The Case of 'semi-ON'

For moderate to low drain biases (V_{DS} < 30 V), the degradation is attributed to hot carriers and the degradation is found to be maximum in the 'semi-ON' state of operation [7]. The electroluminescence micrograph images suggest that the effect of hot carriers is the highest at V_{GS} of approximately -1.5 V for a V_{DS} of 20 V. This can be attributed to the presence of a moderately large number of highly energetic electrons, as a result of a large electric field at the end of the gate on the gate-drain access region side. This results in a large degradation of the transconductance (up to 15% within the first 12 hours) of the device. The significant increase in the degradation at semi-ON state was first reported by researchers from the University of Padova. The images of the EL micrograph and the stress tests in different bias conditions are shown in the Fig II-6 and Fig. II-7 respectively [5], [19].

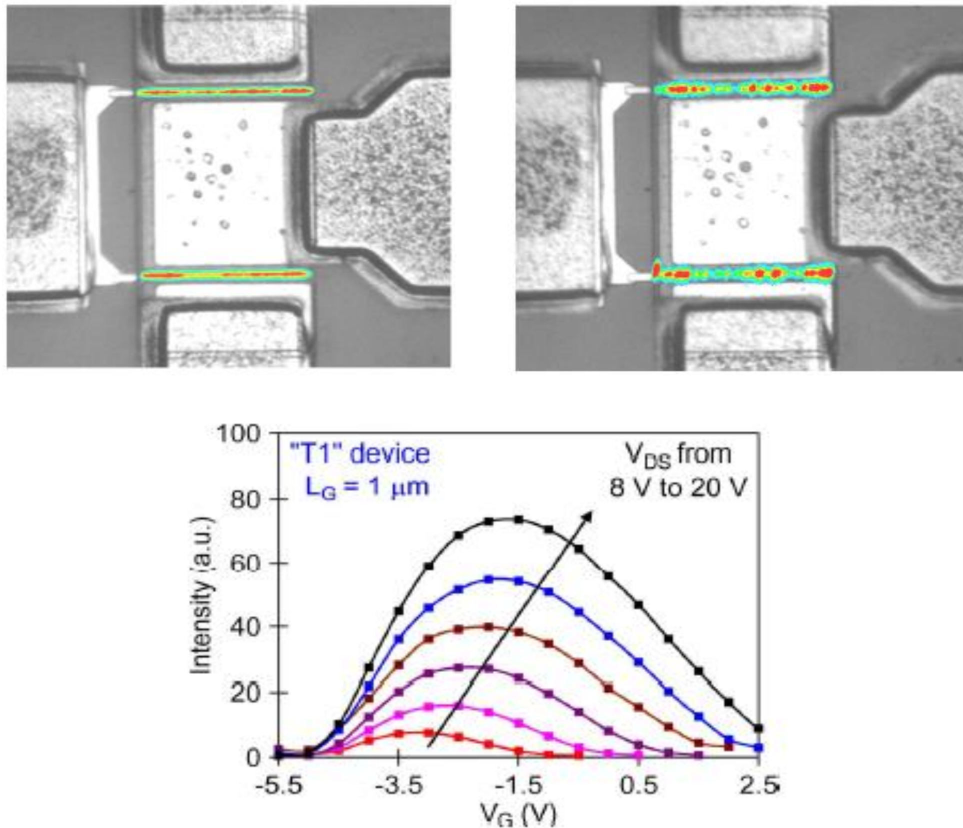

Fig. II-6. EL-intensity micrograph of an AlGaN/GaN HEMT at (top, left) V_{GS} = 0 V (ON condition) and (top, right) V_{GS} = -5 V (semi-ON condition, much brighter) for V_{DS} = 20 V. The bottom plot shows EL-intensity as a function of V_{GS} with V_{DS} varying from 8 V to 20 V [5].

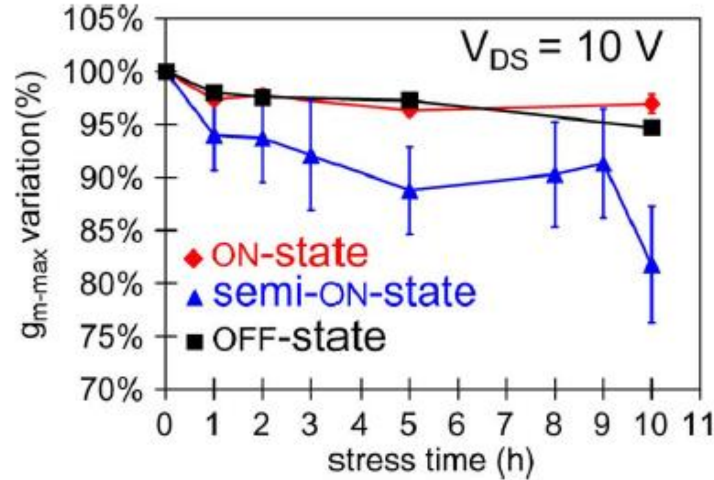

Fig. II-7. The average percent decrease of the maximum value of transconductance measured for V_{DS} = 10 V during a 10-hour stress test under ON (V_{GS} = 0 V, V_{DS} = 20 V), OFF (V_{GS} = -7.7 V, V_{DS} = 20 V) and semi-ON (V_{GS} = -5.5 V, V_{DS} = 20 V) conditions [5].

The shift in threshold voltage and degradation in transconductance in the semi-ON state may result in performance issues in high-power amplification as well as high-frequency switching applications. HEMTs biased in class-AB or deep class-B will be affected the most as the biasing point is very close to the semi-ON region where the threshold voltage shift and transconductance degradation are expected to be the highest because of the simultaneous presence of high electric and field and moderate current density. Class-AB is a popular configuration for high efficiency high-power large-signal amplification applications, due to very low distortion compared to other configurations. The degradation in the transconductance directly impacts the maximum available power gain (*MAG*), as well as the large signal power gain (*LSG*) of the amplifier. Additionally, class-AB amplifiers are usually biased in a way to reduce power consumption compared to class-A amplifiers and to reduce distortion compared to class-B amplifiers. The shift in threshold voltage will result in the class-AB amplifier functioning more like a class B amplifier, resulting in an increase in the distortion [5], [9].

CHAPTER III

PROCESS-DEPENDENCE OF DEGRADATION

This chapter provides an overview of the AlGaN/GaN HEMT devices used for the stress experiments, which is the starting point of the modeling effort. This chapter provides details about the geometry, material composition and fabrication techniques of these devices. The results of the stress experiments performed on these devices have been explained. The modeling approach will be explained in details in the next chapter.

3.1 Growth and Processing Information

The devices used in this study were AlGaN/GaN HEMTs on SiC substrates fabricated at University of California - Santa Barbara (SSLEEC Center). These devices were fabricated using two growth techniques: Plasma-Assisted Molecular Beam Epitaxy (PA-MBE) and Metal-Organic Chemical Vapor Deposition (MOCVD). The MBE growth rate is about 0.5 to 1 μm/hr, performed at a temperature of around 700 C. This growth technique enables growth of precise interfaces which improves transport properties. On the other hand, the MOCVD growth rate is much higher (~ 2 μm/hr), performed at a temperature of about 1000 C. The MOCVD grown devices were NH_3-rich, whereas the PA-MBE devices were Ga-rich and N-rich. The Ga-rich devices show low surface roughness whereas the N-rich devices have lower threading dislocation density.

These devices can be classified into three categories depending on the way the gate metal has been deposited: unpassivated rectangular gate, passivated rectangular gate and passivated trench. The length of the gate is 0.5 μm whereas the width of the structure is 160 μm. The alloy (Ti/Al/Ni/Au) used for the contacts (gate, drain and source) has been annealed at 820 C. The majority of the stress experiment results shown in this work were performed on the devices with passivated rectangular gates (refer Fig. III-1) [21]-[23].

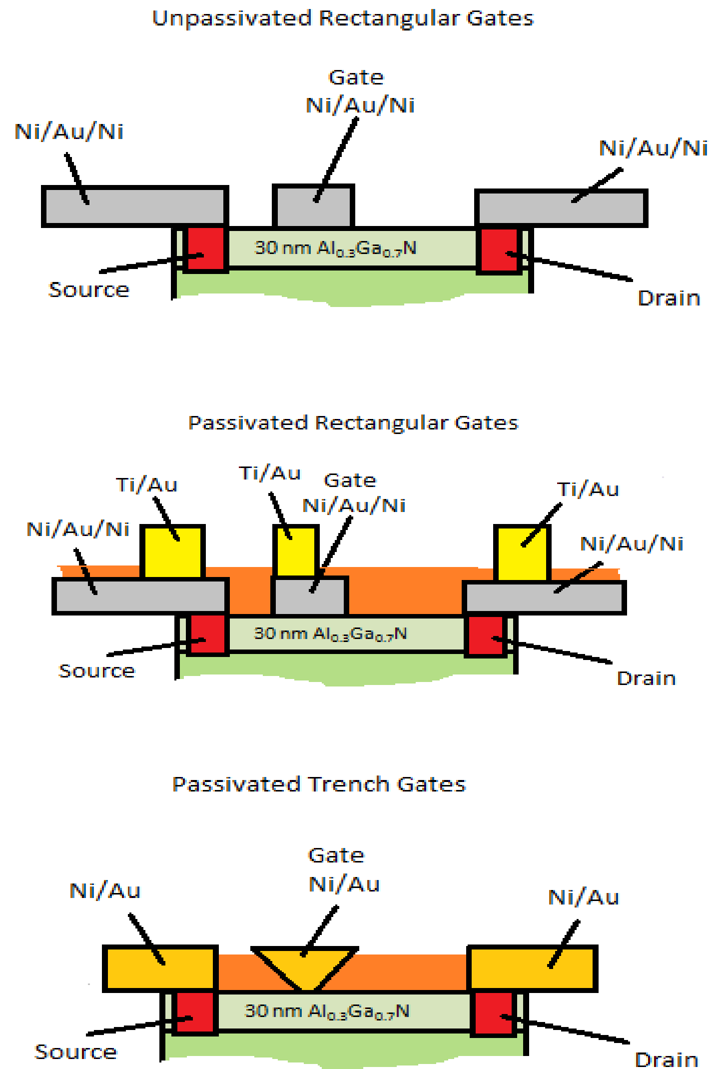

Fig. III-1. The three categories of device characterized: unpassivated rectangular gate (top), passivated rectangular gate (center) and passivated trench gate (bottom). Each category was fabricated using three process techniques: Ga-rich, N-rich and NH_3-rich [21].

The GaN buffer layer is about 3 µm thick and is unintentionally doped. The aluminum mole fraction in the AlGaN layer varies from 28-32 %. The gate structure in these devices is not recessed. The thickness of this AlGaN layer is 30 nm. There is a lot of variation in the gate-source (G-S) and gate-drain (G-D) access region lengths. For consistency, we have used devices with G-S and G-D access lengths of 0.35 µm and 1.2 µm respectively in this work. The passivation layer of silicon-nitride is 160 nm thick [21].

3.2 Basic Transistor Characteristics

The majority of the stress experiments were carried out on the devices with passivated rectangular gates. The value of V_T for the unstressed devices was in the range of -3.5 ± 0.15 V. Fig. III-2 shows the drain current (I_D-V_G) and transconductance (g_m) characteristics for an unstressed Ga-rich rectangular passivated gate device obtained at room temperature. The I_D-V_G characteristic was obtained for a drain bias (V_{DS}) of 0.2 V.

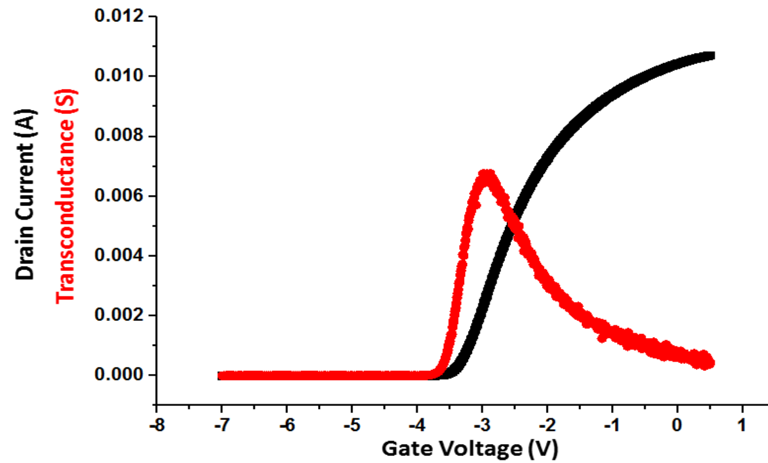

Fig. III-2. The drain current (I_D-V_G) and transconductance ($\delta I_D/\delta V_G$) characteristics for a PA-MBE grown (Ga-rich) rectangular passivated gate device (V_{DS} = 0.2 V). Device width = 160 µm (After [24]).

Fig. III-3 shows the impact of the operating temperature on the V_T of an unstressed PA-MBE grown Ga-rich device. The V_T of the device decreases with the increase in the device temperature. All the transistors show a linear dependence of temperature change on the V_T shift, regardless of the fabrication process or device geometry.

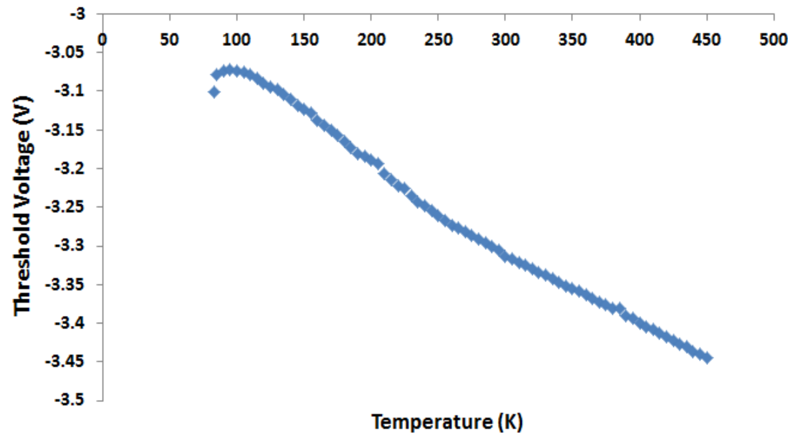

Fig. III-3. The impact of the device temperature on the threshold voltage of an unstressed Ga-rich HEMT.

3.3 Stress Experiment Results: At Semi-ON

The stress tests were performed in the semi-ON condition (V_{GS} = -2 V, V_{DS} = 20 V) as the degradation is expected to be the highest in this state. All the initial measurements were carried out at room temperature and the stress duration ranged from 12 to 24 hours. For the first set of devices, we observed a positive shift in the V_T for the PA-MBE grown (Ga-rich and N-rich) devices whereas there was a negative shift for the MOCVD (NH_3-rich) devices, as shown in Fig. III-4. The positive shift in the V_T indicates a build-up of negative charge at the AlGaN/GaN interface (near the 2DEG), whereas the negative shift in the V_T indicates a build-up of positive charge. The V_T shift for the NH_3-rich devices is significantly greater than the Ga-rich and N-rich devices. The V_T shift plots for N-rich and the NH_3-rich devices indicate saturation at around the three hour mark. There is considerable device-to-device variation in the V_T shift trend, even within the devices fabricated using similar processing conditions. We ignore the stress test results from the Ga-rich samples (of this batch) for our degradation modeling efforts as these devices show very little and inconsistent degradation. There is negligible shift in the V_T for all the three types of devices when subjected to ON stress conditions (V_{GS} = +2 V, V_{DS} = 20 V) [22], [23].

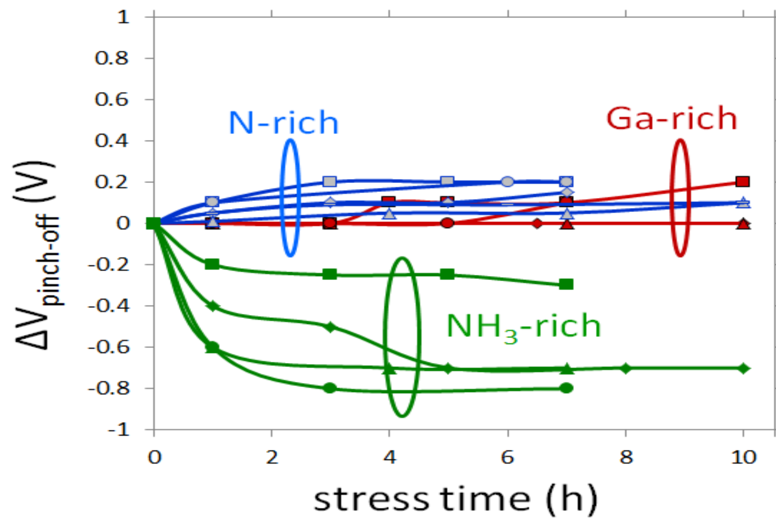

Fig. III-4. $V_{pinch\text{-}off}$ shift for Ga-rich, N-rich and NH_3-rich HEMTs from the first batch of devices stressed in the semi-ON (V_{GS} = -2 V, V_{DS} = 20 V) condition (After [22]).

In the second batch, the majority of the devices were fabricated using the PA-MBE technique under Ga-rich process conditions with passivated rectangular gates. These devices were also subjected to the semi-ON stress (V_{GS} = -2 V, V_{DS} = 20 V), as we observed the maximum degradation in this bias condition. The initial stress tests were carried out at room temperature (for 16 hours). Both the V_T shift as well as the g_m degradation of the device was monitored with respect to the stress time. Fig. III-5 shows the V_T shift and the g_m degradation of the device. The V_T shift is relatively small (around 1.5%, since the unstressed V_T values of these devices are about -3.5 V), whereas the g_m degradation is very large (15%) for the room temperature data [24].

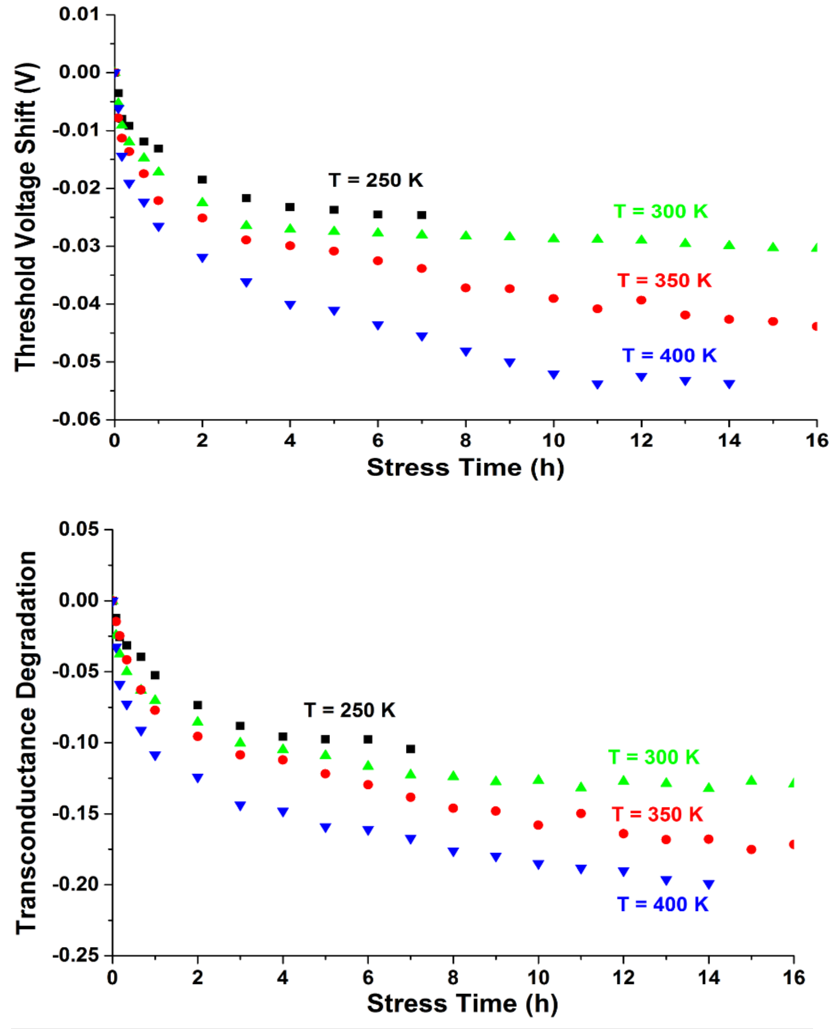

Fig. III-5. (Top) V_T shift for Ga-rich HEMTs in semi-ON condition (V_{GS} = -2.0 V, V_{DS} = +20.0 V) for devices with identical geometries. (Bottom) The corresponding transconductance degradation ($\Delta g_m/g_m$) for the same devices (After [24]).

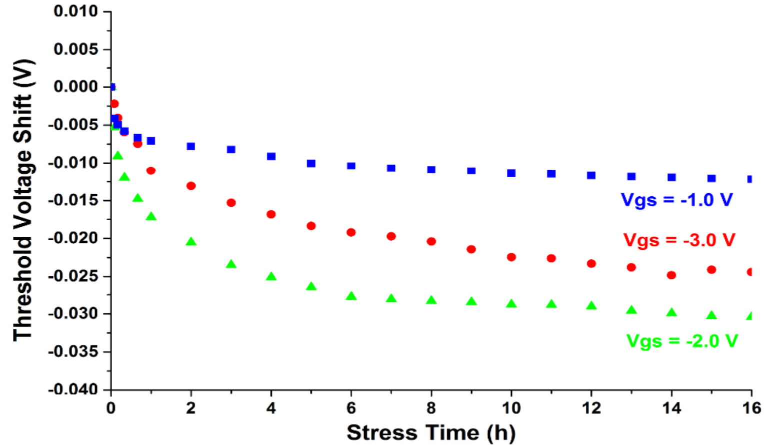

Fig. III-6. V_T shift for identical Ga-rich HEMT devices stressed under different values of gate bias at room temperature (for V_{DS} = 20 V) (After [24]).

We observe that both the V_T shift as well as the g_m degradation increases with the operating temperature. There is a significant increase in the degradation above 350 K. At lower temperatures, the degradation approaches saturation. The small shift in the V_T during the semi-ON stress may not be of great significance, but the large degradation in g_m within 24 hours will be a big concern for engineers designing GaN HEMT-based high efficiency power amplifiers for operation in the class-AB region. The next chapter provides the detailed description of the modeling procedure.

CHAPTER IV

DEGRADATION MODELING: METHODOLOGY

This chapter provides a description of the overall degradation modeling methodology. The predictive model is based on a rate equation that assumes that the degradation is a result of formation of charged defects due to high energy electrons. The chapter also explains the assumptions that have been made to simplify the modeling process.

4.1 Approach for Predictive Modeling

The primary objective of this work is to do predictive modeling of the degradation behavior of important transistor characteristics like V_T and g_m when stressed under different operating conditions, from the result of an accelerated stress test at one given condition. Ensemble Monte-Carlo (EMC) simulations are run at different bias conditions and the carrier-energy statistics are compiled. The condition that results in the largest number of high energy carriers is identified. Then an accelerated stress test is performed at that specific operating condition, as the performance degradation (both V_T shift and the g_m degradation) is the highest when there is maximum number of high energy carriers. The direction of V_T shift from the stress test is useful in identifying the candidate defects that may be present in the device as the growth conditions are known. These point defects are believed to be created by an electron-activated hydrogen removal process. First-principles DFT is used to calculate the activation energy of the defect. Only the electrons with higher energy than this activation energy can form or modify a defect. The number of carriers that exceeds this activation energy is calculated from the EMC results. These results are used in an equation that gives the defect generation rate. Fig. IV-1 provides an overview of the modeling approach used for the threshold voltage degradation prediction process [24]-[28].

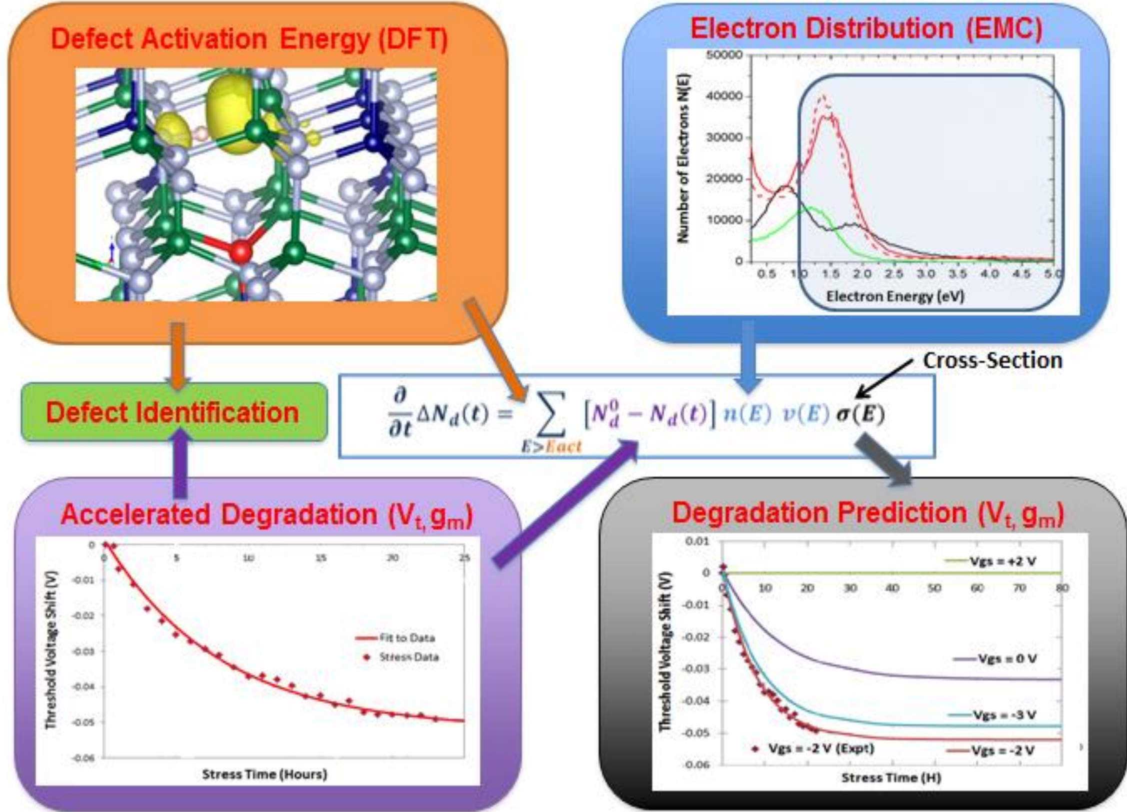

Fig. IV-1. Overview of methodology for the degradation modeling process. The methodology is based on the assumption that the V_T shift and the g_m degradation takes place due to the build-up of charged defects near the AlGaN/GaN interface. High energy carriers are responsible for the formation of these defects due to hydrogen depassivation process. In this exercise, the DFT calculations were performed by **Yevgeniy Puzyrev** and **Xiao Shen**, whereas the stress experiments were carried out by **Jin Chen** and **Tania Roy**.

4.2 Assumptions for Simplification

In this approach the charged defects responsible for degradation are assumed to be distributed uniformly along the channel and the stress induced change in the areal density of the charged defects under the gate results in the shift in V_T, whereas the change in the density of the charged defects under the gate as well as the gate-drain access region results in the degradation of g_m. For simplicity, we consider that the defects are created in a single step by the energetic carriers. We do not consider the dehydrogenation process in terms of electron wind force. Electrons with energies lower than the activation energy can also result in depassivation as long as the carrier strike interval is less than the relaxation time of the system. The simplified σ is assumed to be zero for energies up to E_{act} and a constant value for higher energies.

4.3 The Rate Equation

The device response is modeled by assuming that the energetic carriers can transfer energy to the pre-existing defects and transform them into new configurations and/or new charge states that alter the device characteristics. The change in the defect charge state leads to the shifts in V_T and the degradation of I_D and g_m with increasing stress time. The defect generation rate near the AlGaN/GaN interface is given by the equation:

$$\frac{\partial}{\partial t} Q_d(t) = \sum_{E > E_{act}} \Delta Q_d \, n(E, T, V_{GS}, V_{DS}) \, v(E) \, \sigma(E) \qquad (\text{IV} - 1)$$

where $n(E)$ is the carrier density, $\upsilon(E)$ is the velocity of electrons with energy E, E_{act} is the effective activation energy for the defect transformation, q is the electronic charge, $\sigma(E)$ is the effective, average scattering cross-section of the defects, and $\Delta Q_d(t)$ is the stress-induced change in the areal density of the charge near the interface,

$$\Delta Q_d(t) = q \, [N_d^{\infty} - N_d(t)] \qquad (\text{IV} - 2)$$

where $N_d(t)$ is the areal density of the activated defects at time t and N_d^{∞} is the areal density of the pre-cursor defects. The difference $[N_d^{\infty} - N_d(t)]$ is the concentration of the available pre-existing defects at time t. The scattering cross-section is assumed to be zero for energies up to E_{act} and constant for the higher energies. The carrier density $n(E)$ is obtained from the HFET EMC simulation results, and E_{act}, is calculated using ab-initio DFT. The V_T shift is related to the change in charge density as follows:

$$\Delta V_T(t) = \frac{\Delta Q_d(t) \, d_{AlGaN}}{\varepsilon} \qquad (\text{IV} - 3)$$

where d_{AlGaN} is the thickness and ε is the dielectric constant of the AlGaN layer.

The transconductance (g_m) degradation can now be related to the V_T shift of the device for modeling process. The detailed analysis to link the degradation in transconductance ($\Delta g_m / g_m$) with the stress time to the change in charged defect density ($N_d(t)$) and hence, the shift in $V_T(t)$ has been shown in the Chapter X.

4.4 Exponential Dependence of Degradation

For determining the scattering cross-section of the defect in device, it is helpful to represent the rate equation with an exponential dependence (of time constants) of the carrier energy and electron density. The degradation equation with this exponential dependence can be used to fit the stress test data reasonably well. This can be done in the following way:

Assuming the scattering cross-section of the defect to be independent of energy, combining the equations IV-1 and IV-2, we get the following expression for the rate of change of charged defects with the stress time:

$$\frac{\partial}{\partial t}N_d(t) = \sum_{E>E_{act}} [N_d^{\infty} - N_d(t)]\, n(E,T,V_{GS},V_{DS})\, v(E)\, \sigma \qquad (\text{IV}-4)$$

Now, rearranging the terms and integrating,

$$\int \frac{N_d{}'(t)\, dt}{[N_d^{\infty} - N_d(t)]} = \int \sum_{E>E_{act}} n(E,T,V_{GS},V_{DS})\, v(E)\, \sigma\, dt \qquad (\text{IV}-5)$$

=>

$$-\log\, [N_d^{\infty} - N_d(t)] = \sum_{E>E_{act}} n(E,T,V_{GS},V_{DS})\, v(E)\, \sigma\, t + c \qquad (\text{IV}-6)$$

=>

$$[N_d^{\infty} - N_d(t)] = e^{-\frac{t}{\tau}+c} \qquad (\text{IV}-7)$$

where,

$$\frac{1}{\tau} = \sum_{E>E_{act}} n(E,T,V_{GS},V_{DS})\, v(E)\, \sigma \qquad (\text{IV}-8)$$

Now, at $t = 0$:

$$c = \log\, [N_d^{\infty} - N_d(0)] \qquad (\text{IV}-9)$$

Now, combining the equations IV-7 and IV-9,

$$[N_d^{\infty} - N_d(t)] - N_d(0) = e^{-\frac{t}{\tau}} e^{\log\, [N_d^{\infty} - N_d(0)]} \qquad (\text{IV}-10)$$

=>

$$[N_d^{\infty} - N_d(t)] - N_d(0) = [N_d^{\infty} - N_d(0)]e^{-\frac{t}{\tau}} \qquad (IV-11)$$

Rearranging the terms,

$$N_d(t) = [N_d^{\infty} - N_d(0)][1 - e^{-\frac{t}{\tau}}] \qquad (IV-12)$$

Combining equations IV-3 and IV-12,

$$\Delta V_T(t) = \frac{q\, d_{AlGaN}}{\varepsilon}[N_d^{\infty} - N_d(0)]\left[1 - e^{-\frac{t}{\tau}}\right] \qquad (IV-13)$$

This equation gives the exponential dependence of the degradation (V_T shift) on the carrier energy distribution. The time constant (τ) can be obtained from fitting the stress test data, and this value is directly related to the energy of the hot electrons capable of depassivating hydrogen and cause charged defects, which can be obtained from the EMC simulations. The equation IV-13 can be extended to multiple defects (different scattering cross-sections, and with different activation energies) in the following way,

$$\Delta V_T(t) = \frac{q\, d_{AlGaN}}{\varepsilon}\left\{[N_d^{\infty} - N_d(0)]'(1 - e^{-\frac{t}{\tau 1}}\right) + [N_d^{\infty} - N_d(0)]''(1 - e^{-\frac{t}{\tau 2}}) + \cdots \dots + [N_d^{\infty} - N_d(0)]'^{\cdots}(1 - e^{-\frac{t}{\tau n}})\} \qquad (IV-14)$$

where the time constants are as follows,

$$\frac{1}{\tau_1} = \sum_{E>E_{act1}} n(E,T,V_{GS},V_{DS})\ v(E)\sigma_1$$

$$\frac{1}{\tau_2} = \sum_{E>E_{act2}} n(E,T,V_{GS},V_{DS})\ v(E)\sigma_2$$

.....

$$\frac{1}{\tau_n} = \sum_{E>E_{actn}} n(E,T,V_{GS},V_{DS})\ v(E)\sigma_n$$

CHAPTER V

ENSEMBLE MONTE-CARLO SIMULATOR DESCRIPTION

This chapter describes the basic formalism of the simulator used for the EMC simulations. The Michigan HFET is a C++-based 2-D FEM numerical simulator that has been designed specifically for modeling III-V semiconductor devices. HFET has been developed at the University of Michigan by Prof. Jasprit Singh and his team. This chapter also gives a description of the device structure and material composition that are simulated.

5.1 Simulator Overview: Michigan HFET

This section describes the simulation flow and the physics involved in HFET simulator while modeling a standard III-V device. The formalism is as follows [29]-[33],

1) A two-dimensional (2-D) Poisson, drift-diffusion and continuity equation finite element method (FEM) solver has been used to obtain the current-voltage curves, charge distribution, and electric field along the channel. Please refer Fig. V-1 for the flow.

2) The quasi-Fermi levels obtained from the 2-D Poisson and drift-diffusion solver are then used to solve the Schrödinger and Poisson equations to obtain the wave function and 2-D confined energy level for the different points. Shockley-Read-Hall generation-recombination is also included in the current continuity equation.

3) A 2-D multi-valley (Γ, *L, A* and *U-M*) (refer Fig. V-2) EMC technique is then used to simulate the electric field and the spatial velocity of electrons along the channel. This is calculated using the electric field from the steady-state mobility model. The effects of polarization at AlGaN/GaN interface are included through a charge-control model [31].

4) The spatial velocity of the electrons obtained from EMC as the new mobility model and then feed it back to 2-D Poisson and drift-diffusion solver to solve the equation self-consistently.

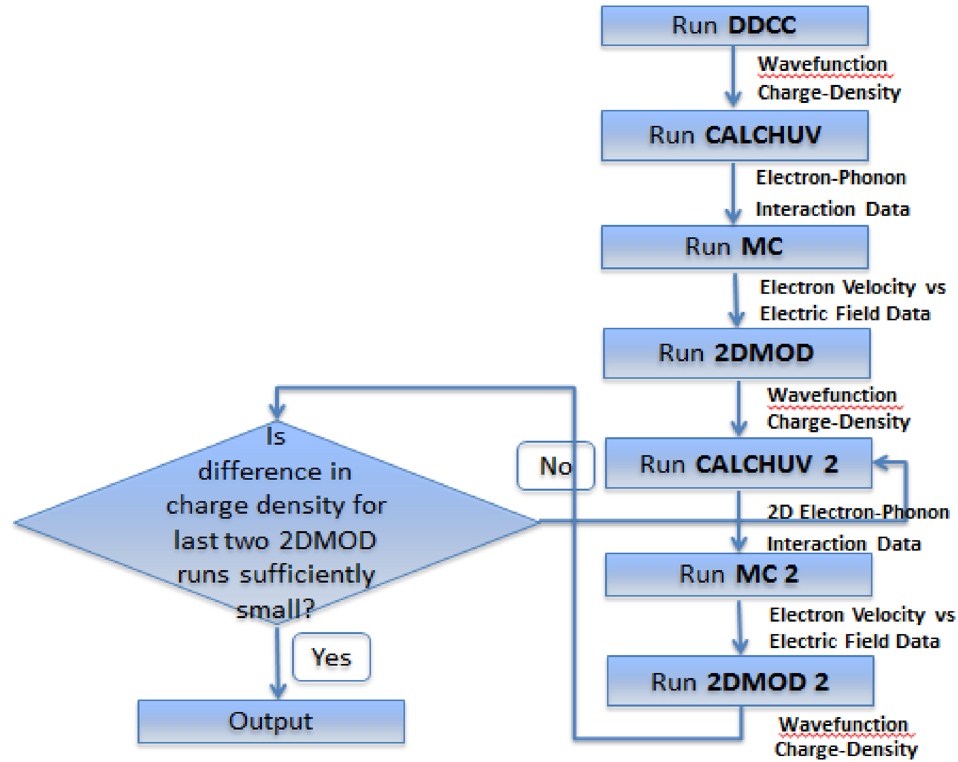

Fig. V-1. Overview of the flow of the formalism for a simulation run using the HFET simulator. The functionalities of the different sections in this flow are as follows [29]:

- ➔ Section DDCC: Solves Poisson and Schrodinger equations (1D).
  Output: Wave-function and charge density.
- ➔ Section CALCHUV: Simulates electron-phonon interaction (2D).
  Output: Electron-phonon interaction data.
- ➔ Section MC: Simulates high-field transport (with 500000 carriers).
  Output: Electron-velocity field along the channel (constant field).
- ➔ Section 2DMOD: Solves Poisson and Schrodinger equations (2D).
  Output: Electric field, Wave-function, charge density (2D).

- ➢ Section 1: Considering constant electric field.

- ➢ Section 2: Considering spatially varying electric field.

5.2 Simulator Formalism: EMC Approach

From the 2-D solver, the electric field profile, quasi-Fermi level, and charge distribution in the channel is obtained. However, the Schrödinger equation can only be solved in the perpendicular y-direction to obtain the confined state in the channel. Therefore, the one-dimensional (1-D) Schrödinger equation and Poisson equation are solved at each x point to obtain the wave function and the 2-D confined energy level for different x points. The scattering rate at

each point x under the channel is then calculated. Then, EMC method is utilized to simulate the electron velocity through the electric field $E_x(x)$. For short-channel effects, the E_y component mainly influences the charge density especially near the drain depletion region. This effect is already taken into account by applying different scattering rates at different points. The 2-D and 3-D EMC method is then implemented with 500000 electrons for the structure. The statistical electron velocities and energy along position of the channel are then recorded and averaged. The MC process takes the following scattering mechanisms (Fig. V-3) into account [31], [32]:

1) polar optical phonon absorption and emission

2) acoustic phonon scattering

3) interface roughness scattering

4) equivalent and non-equivalent inter-valley scattering

5) alloy scattering and

6) charged dislocation scattering.

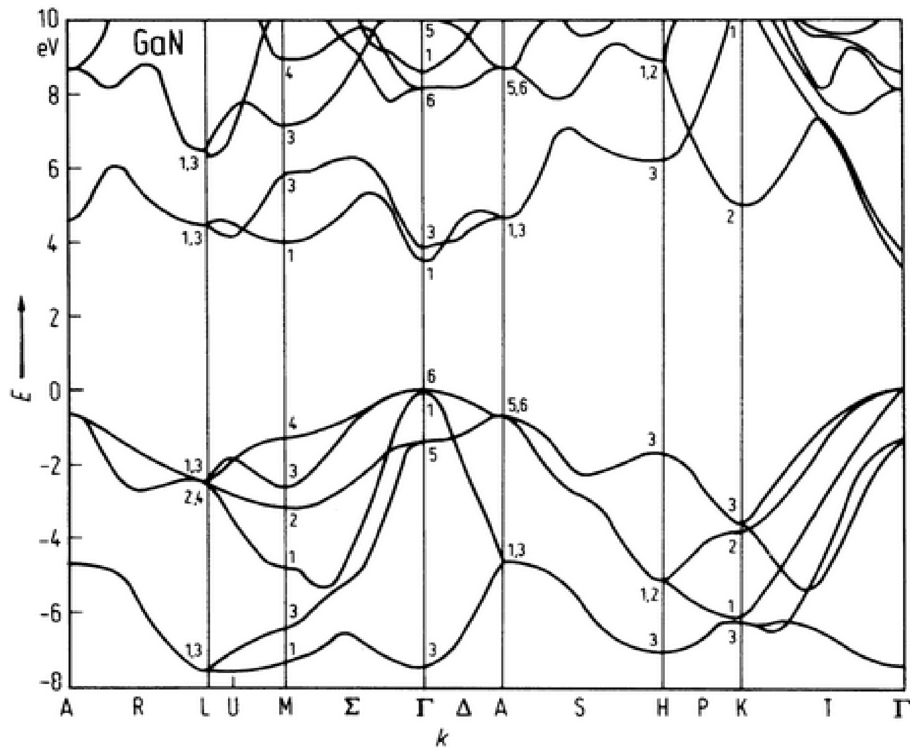

Fig. V-2. The E-k diagram for Gallium Nitride (for Wurtzite arrangement). The Michigan HFET simulator considers the non-parabolicity effects in the *Γ*, *L, A* and *U-M* valleys [34].

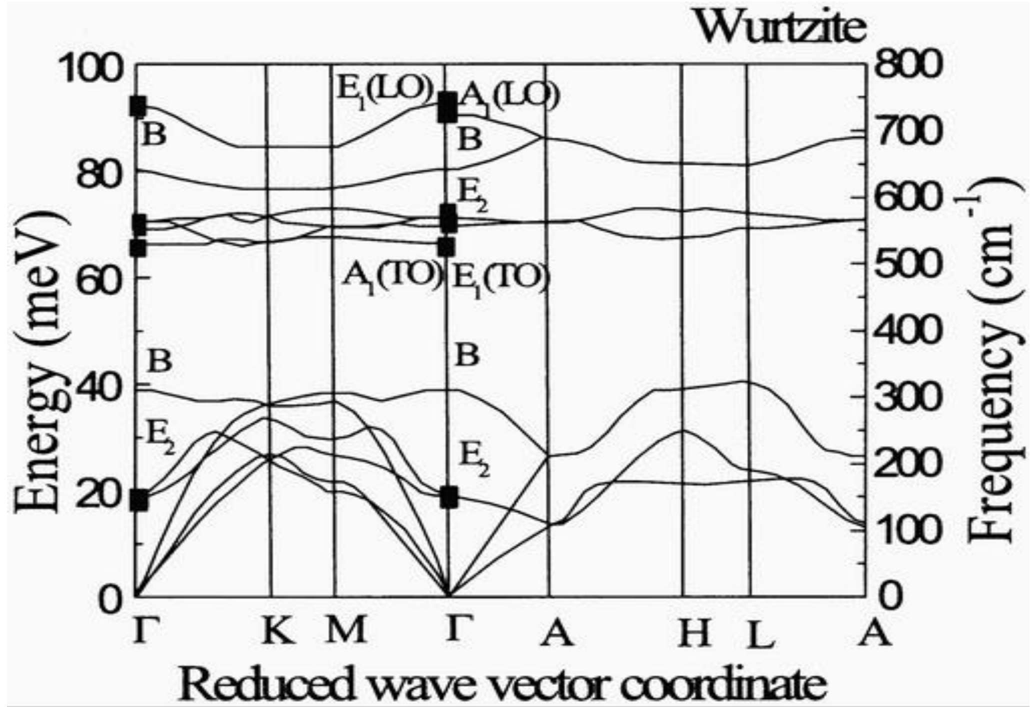

Fig. V-3. Calculated dispersion curves for acoustic and optical branch phonons for Gallium Nitride [34].

For the first iteration, the spatial velocity of the electrons is obtained from the electric field calculated from the steady state mobility model. However, for the short-channel devices, the steady-state mobility model may not work well due to the velocity-overshoot effects. The electric-field component $E_x(x)$ obtained from the steady-state mobility model may not be correct in such short-channel devices. For better accuracy, there is a need to couple the EMC into a 2-D-Poisson and drift-diffusion solver to solve the equation self-consistently. Therefore, the spatial velocity and the old $E_x(x)$ in the channel are used as the new mobility model for the 2-D Poisson and drift-diffusion solver to obtain the new electric-field $E_x(x)$ and charge-distribution profile. Then, the previous steps are repeated to solve the equations self-consistently. With these iteration steps, the spatial electron velocity can be obtained accurately.

The values of fixed charges are used in the charge control calculation, which involves the solution of the Schrodinger and Poisson equations (in 1-D) self-consistently to obtain the potential profile, carrier wave functions and energy levels. The Schrodinger equation (Eq. V-1) yields the confined charge terms in the Poisson equation (Eq. V-2), which in turn determines the

potential profile. This potential profile is fed back into the Schrodinger equation and this process is repeated until the solution of the Poisson equation converges.

$$-\frac{\hbar^2}{2m^*}\frac{d^2\psi_n(z)}{dz^2}+V(z)\psi_n(z)=E_n\psi_n(z) \qquad (\text{V}-1)$$

$$\frac{d^2V(z)}{dz^2}=-\rho \qquad (\text{V}-2)$$

The resulting wave functions from the solution of Eqs. V-1 and V-2 are then used to calculate overlap integrals, I_{mn}, which are used in the calculation of the inter-subband matrix elements. It must be noted that the above wave functions are normalized over the entire device,

$$I_{mn}=\int \psi_m^*(z)\psi_n(z)dz \qquad (\text{V}-3)$$

Transport properties are calculated by the usual Monte Carlo method. This involves simulation of the motion of a single electron over a long period of time to obtain carrier velocities or simulation of many carriers over a short period of time to obtain the distribution of velocities. This Monte Carlo process models the dominant scattering mechanisms at 300 K – acoustic and polar optical phonon emission and absorption, interface roughness and alloy scattering, interspersed with periods of free flight. The process proceeds in the following steps:

1) Initial calculation of the scattering rates for intra- and inter-subband scattering.

2) Injection of electrons into the structure. Carriers are initially injected with thermal velocity.

3) Random choice of scattering event as one of acoustic phonon scattering, polar optical phonon absorption and emission, intervalley scattering, interface roughness scattering, alloy scattering, etc.

4) Updating the final position and velocity of the electron after the scattering event.

5) Free flight.

Steps 3 and 5 are repeated until the end of the simulation. For the purpose of the simulation, the motion of one electron is considered, for a long period of time in the present case, 16 ns. This long period of simulation is chosen to ensure that the velocity at the end of the

simulation is a steady state velocity corresponding to the saturation, uniquely corresponding to the electric field in the channel. The resulting curve is used to deduce the low field drift mobility. The advantage of using this technique is that one can obtain a very fine level of detail about the electron transport process.

The values of different material constants are taken from the literature. There is considerable uncertainty about the values of non-parabolicity of the upper valleys in the conduction band of wurtzite nitrides. The non-parabolicity factors used in the simulator are obtained from first principles calculation. The relation of effective mass of an electron in a semiconductor to the band gap is described by the k.p formalism:

$$\frac{1}{m^*} = \frac{1}{m_0} + \frac{2p_{cv}^2}{3m_0^2}\left(\frac{2}{E_{g\Gamma}} + \frac{1}{E_{g\Gamma} + \Delta}\right) \qquad (V-4)$$

where Δ is the separation between the heavy hole and the split-off bands.

In the Monte-Carlo approach, the electron is treated as a point particle along the channel plane, but in the growth direction, it is represented by an envelope function. The envelope function for the ground state is localized very close to the AlGaN/GaN interface. For higher subbands, it is spread into the GaN or AlGaN region. To calculate the scattering rates for a state that overlaps several different regions, an averaging procedure is used. The material parameters are averaged over the number of layers (*N*) and hence, each subband has its own value of the relevant parameter. Since, the wave functions are normalized over the entire device, the subband dependent value of material parameter is given by:

$$G_j = \sum_{i=1}^{N} f_{ji} G_i \qquad (V-5)$$

$$\text{where } f_{ji} = \int_{z_j-1}^{z_j} \psi_i^*(z)\psi_i(z)dz \qquad (V-6)$$

5.3 Device Structure and Composition

The device simulated was an AlGaN/GaN HEMT structure shown in Fig. IV-1. The AlGaN layer is 25.0 nm thick and its mole-fraction is 0.32. A Schottky barrier of $\Phi_b = 1.68$ eV is used to model the gate contact. The device structure and composition is the same as that of the actual devices used in the stress experiments. The formation of the two-dimensional (2-D) electron gas in AlGaN/GaN HEMT is due to the simultaneous presence of spontaneous and piezoelectric polarization introduced by fixed charges at the interface. The fixed charges are represented by 1.4×10^{13} cm^{-2} positive charges [12]. The doping in the GaN is 10^{15} cm^{-3} n-type, representing the unintentional doping during fabrication process. The gate, gate-source (G-S) access and gate-drain (G-D) access region were 0.05 µm, 0.35 µm, and 1.20 µm long, respectively. The initial simulations were performed at 300 K and the threshold voltage of the device was estimated to be about -3.8 V. The experiments showed that the V_T was around -3.5 V. The simulations were repeated at different gate biases in order to investigate the electric field and energy distributions for the ON and Semi-ON states. In the OFF state (with gate-bias less than the threshold voltage) there are insufficient carriers to complete the simulation and obtain the carrier-energy statistics. Similar simulations were performed to examine the effects of drain-bias, device temperature, doping concentrations, mole-fraction and device geometry on the carrier-energy statistics [27]-[29]. The results of the EMC simulations have been presented in the next chapter.

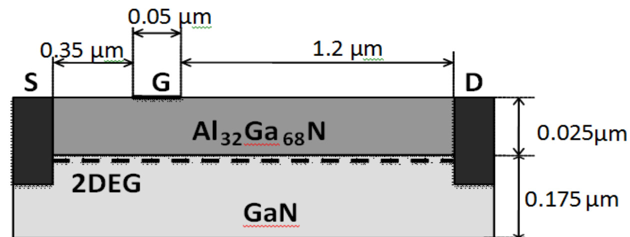

Fig. V-4. Cross-section of the AlGaN/GaN HEMT structure used for the EMC (Michigan HFET) simulations. The substrate (not shown here) used is SiC by default. The gate structure is recessed. Gate, source and drain contacts are all 50 nm in length [27].

CHAPTER VI

ENSEMBLE MONTE-CARLO SIMULATION RESULTS

This chapter describes the results obtained from the Michigan HFET EMC simulator. The energy band diagrams and the carrier densities are initially obtained under different operating conditions. Then we look at the electric field along the device under the same conditions. Next the carrier energy distribution is reported at the specific location where the electric field is at its highest for the three regions of operation. We also report the change in the carrier distribution depending on the change in other operating conditions such as temperature, doping density, device dimensions, AlGaN thickness and the Al mole-fraction.

6.1 Band Diagram and Carrier Density

The device described in chapter V (Fig. V-4) has been used for the EMC simulations, in which the AlGaN layer is 25 nm thick and the Al mole-fraction is 0.30. In these simulations, we maintain the drain bias at 20 V. The lowest value of gate bias for which the simulation cycle gets completed is -3.8 V. This indicates that for a V_{DS} of 20 V, there are insufficient carriers in the channel when V_{GS} is lower than -3.8 V. The results indicate that the threshold voltage for the simulated device is approximately -3.9 V when the drain bias applied is 20 V. Hence, we have not reported results from the OFF state of transistor operation

The energy band diagrams reported here are obtained vertically, sliced at the middle of the gate contact. Fig. VI-1 reports the band diagrams for the different bias conditions. We first look at the energy band diagram for the case when no gate bias (V_{GS} = 0 V) is applied to the device. Even without application of a gate bias, a quantum well (2D Electron Gas layer) is formed at the interface. So, the device is turned ON without a positive gate bias. Hence, these AlGaN/GaN HEMTs are depletion mode, which is typical.

a)

b)

c)

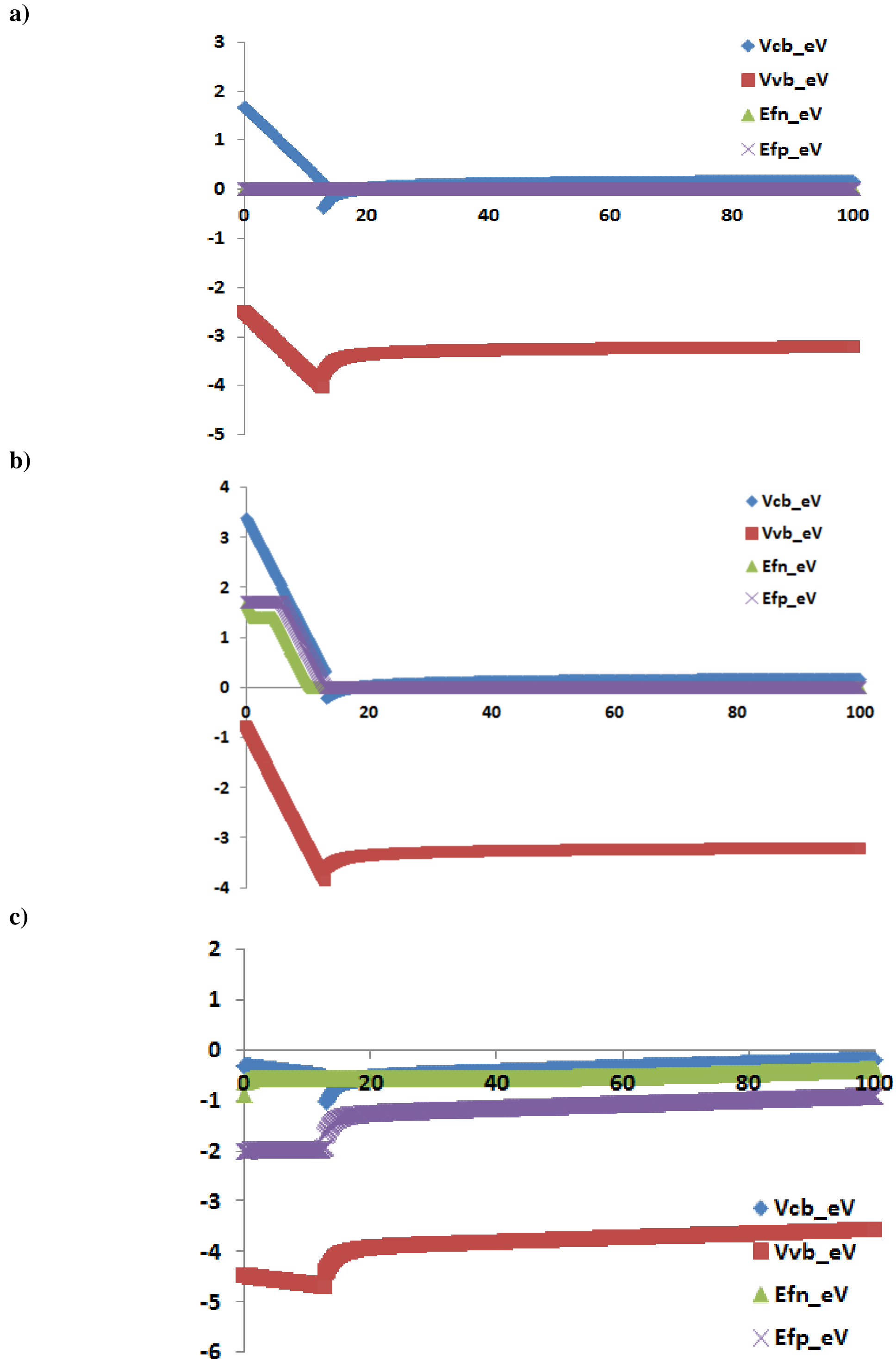

Fig. VI-1. Energy band diagram obtained at the middle of gate (at 300 K) for (a) V_{GS} = 0 V, V_{DS} = 20.0 V (b) V_{GS} = -2.0 V, V_{DS} = 20.0 V (c) V_{GS} = +2.0 V, V_{DS} = 20.0 V. The quantum well (2DEG) at the interface. The blue points indicate the conduction band, the red points indicate the valence band, green points indicate the electron fermi level and the violet point indicates the hole fermi level. The x-axis is in nanometers, whereas the y-axis is in eV.

Next, we investigate the carrier density in the device by slicing the device at the same point where the energy band diagrams were obtained. Fig. VI-2 shows the electron and hole densities for different bias conditions at room temperature. The AlGaN/GaN interface in this figure is at 15 nm. A very high peak in the electron density can be observed near this interface for all the bias conditions considered. The hole density on the other hand is negligible for all the cases. There is a very large electron density at the interface even without a gate bias being applied, since the device is depletion-mode (Fig. VI-2 (b)). The carrier density increases as we apply a positive gate bias (Fig. VI-2 (c)). In the semi-ON state of operation (V_{GS} = -2 V), the electron density is about a quarter compared to that of the ON condition (Fig. VI-2 (a)). Now, increasing the V_{DS} also has an impact on electron density at the interface too. It can be observed that for V_{DS} of 30 V, the density for V_{GS} = -2 V is higher than for V_{DS} of 20 V (Fig. VI-2 (d)).

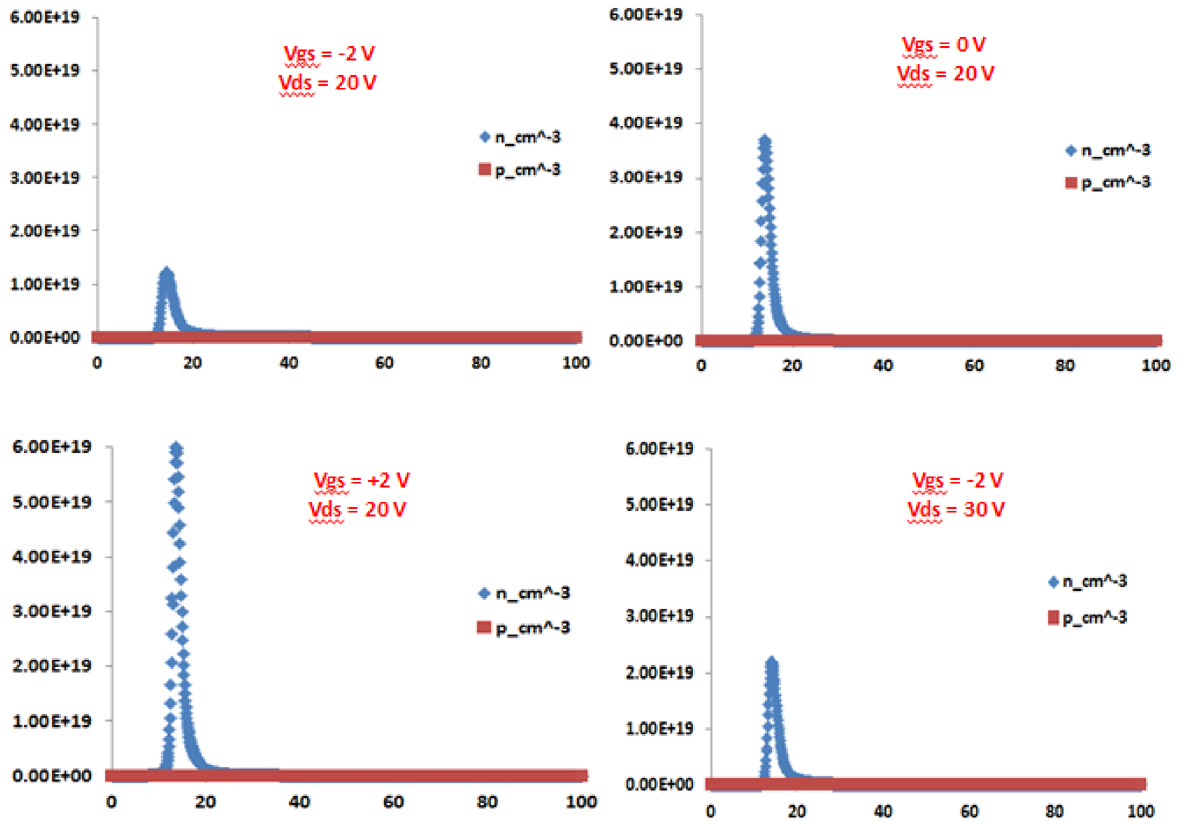

Fig. VI-2. Electron and hole density obtained by slicing at the gate (at 300 K) for (a) V_{GS} = -2.0 V, V_{DS} = 20.0 V (b) V_{GS} = 0 V, V_{DS} = 20.0 V (c) V_{GS} = +2.0 V, V_{DS} = 20.0 V (d) V_{GS} = -2.0 V, V_{DS} = 30.0 V. The x-axis is in nanometers. The peak is right at the AlGaN/GaN interface.

6.2 Profiles of Electric Field

The electric field dependence on the bias conditions is reported in this section. Both the parallel and perpendicular component of the electric field are presented (along the channel) in Fig. VI-3. The simulations are performed at different gate bias conditions for a V_{DS} of 20 V. All these results are for 300 K. In the figures mentioned below, the gate region extends from 0.35 μm to 0.40 μm (in the x-axis). The position 0.4 μm represents the gate edge on the gate to drain (G-D) access region side.

a)

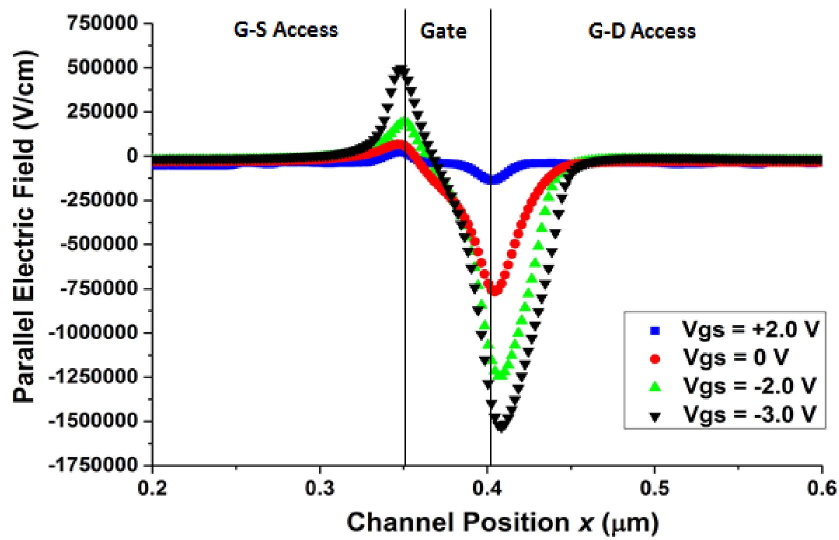

b)

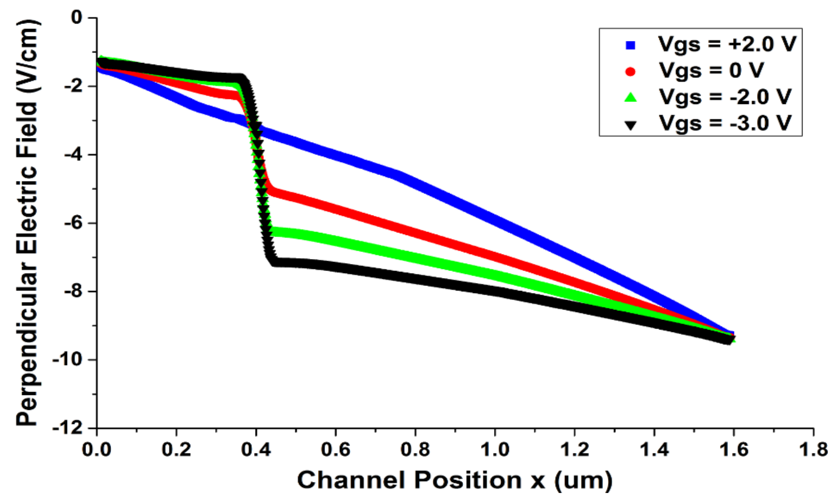

Fig. VI-3. a) Parallel and b) Perpendicular electric field as a function of channel position for different V_{GS} values at 300 K for V_{DS} = 20.0 V. The gate extends from 0.35 μm to 0.4 μm (After [26]).

The parallel electric field (refer Fig. VI-3 (a)) becomes positive at the gate-edge on the G-S access region side and goes negative at the gate-edge on the G-D access region side. The magnitude is significantly higher at the gate-edge on the G-D access region side for all the values of gate bias. The electric field keeps increasing as the value of V_{GS} becomes more and more negative. The electric field is negligible for a positive gate bias. The perpendicular component (refer Fig. VI-3 (b)) of the electric field is significantly smaller in comparison for all values of V_{GS}. Hence, the resulting magnitude of the total electric field is also the highest at the end of the gate on the G-D access region side. This indicates that the carriers with the highest kinetic energies are present in this region of the device, irrespective of the device operating conditions.

6.3 Carrier Energy Distribution (Bias Dependence)

Since, the electric field is at its maximum at the end of the gate on the G-D access region side, we investigated the energy of the electrons at this point by taking a slice at this point. Fig. VI-4 shows the carrier energy distribution for four values of V_{GS} vaat 300 K with V_{DS} at 20 V, obtained at the end of the gate on the G-D access region side. These carrier energy distributions (sliced at 0.4 μm across the device cross-section, with the source edge as the origin) show a distinct peak for moderate energy electrons (0.5 to 2.0 eV) and a high energy (carrier with energies greater than 2 eV) tail for all non-positive V_{GS} values. Both the moderate energy and the high energy carrier peaks are the highest for the case of V_{GS} = -2.0 V (semi-ON state). For V_{GS} = +2.0 V (completely ON), there are very few carriers above 0.4 eV, so the degradation is expected and observed to be minimal. The moderate energy carrier peak moves more and more to the left (lesser energy) as the gate bias becomes more and more negative. Hence, the number of lower energy carriers (i.e., less than 0.5 eV) is significantly larger for V_{GS} = -3 V. In the region of 2-3 eV energy, the highest number of carriers are for V_{GS} = 0 V.

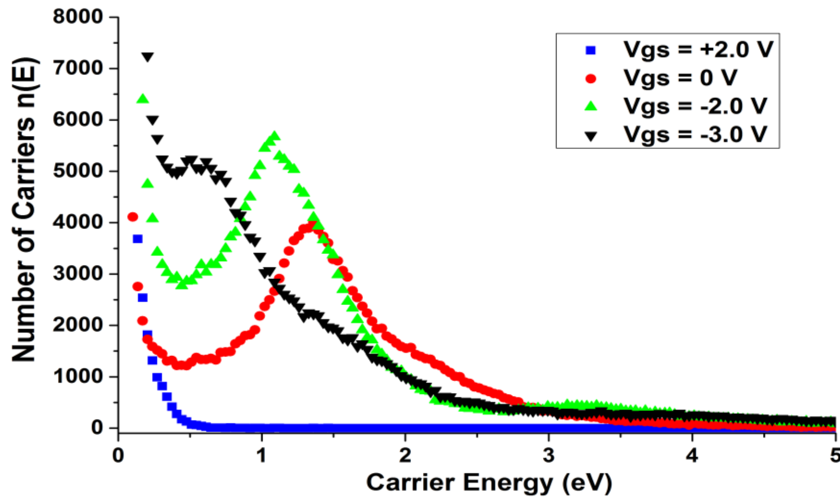

Fig. VI-4. Carrier energy distribution for different gate bias values at 300 K for V_{DS} = 20.0 V sliced at the end of gate on G-D access region side (0.4 μm) (After [27]).

The moderate and high energy peaks in the carrier-energy distribution can be explained in terms of inter-valley scattering. The moderate energy carrier peak observed at around 1.1 to 1.4 eV is due to carriers getting accumulated in the *A*-valley of the E-k diagram of Wurtzite GaN (please refer Fig. V-2). The reason is that the *A*-valley is about 1.3 eV from the lowest point in (Γ-valley) the conduction band. So, the number of electrons in this valley increases as the electric field increases when the gate bias become more and more negative (till V_{GS} = -2 V). At a more negative value of V_{GS} the electric field becomes so high that the electrons scatter back to the Γ-valley. So, there is no moderate energy carrier peak for V_{GS} = -3 V, as there are few electrons present in the *A*-valley. Instead, there is a relatively large concentration of lower energy carriers in this condition. The higher energy carriers peaks (around 3 to 4 eV) can be attributed to the presence of carriers in the upper valleys. The electric field for V_{GS} = +2 V is so low that there are virtually no electrons in the *A*-valley, resulting in very few moderate energy carriers and virtually no high energy carriers. Table VI-1 reports the distribution of carriers for different gate bias conditions. This simultaneous presence of large electric field as well as moderate density of carriers in the semi-ON state may result in much higher degradation than in the ON or OFF conditions.

TABLE VI-1

Number of carriers above a given energy level (in steps of 0.5 eV) for different values of V_{GS} with V_{DS} = 20 V at room temperature obtained at the end of the gate on the G-D access region side.

Greater than	V_{GS} = +2 V	V_{GS} = 0 V	V_{GS} = -2 V	V_{GS} = -3 V
0.5 eV	2840	139000	184000	162000
1.0 eV	340	115000	129000	94600
1.5 eV	110	63800	64500	62500
2.0 eV	32	32600	35400	34800
2.5 eV	0	14900	26200	25300
3.0 eV	0	6840	20400	20800

a)

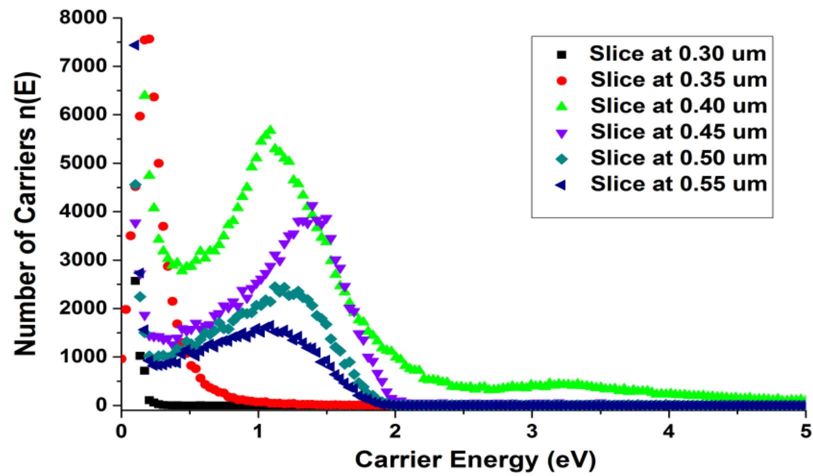

b)

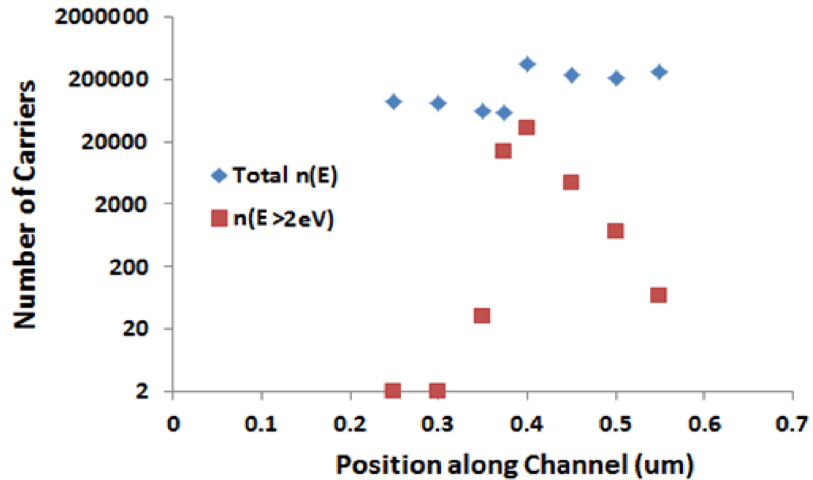

Fig. VI-5. (a) Carrier energy distribution for V_{GS} = -2.0 V, V_{DS} = 20.0 V (at 300 K) obtained by slicing at different points along the channel. (b) The total number of carriers at each slicing point compared with the number of energetic (E > 2 eV) carriers at the corresponding point (after [24]).

Fig. VI-5 (a) shows carrier energy distributions at different points along the channel for the semi-ON state at 300 K. The figure confirms that the number of both moderate and high energy carriers is significantly higher at the gate edge (0.4 µm slice). As we move away from the gate edge towards the drain, the moderate energy carrier peak starts to decrease. As we move towards the gate, very few moderately energetic carriers are present, but a fairly large number of low energy (less than 0.5 eV) carriers are present. Only the 0.4 µm slice shows the secondary peak for very high energy carriers. Other cuts show very few carriers with energies greater than 2.5 eV. Fig. VI-5 (b) indicates the total number of carriers as well as the number of energetic carriers at each slicing point in the device.

6.4 Carrier Energy Distribution (Temperature Dependence)

Next, we consider the effects of the device temperature on the carrier energy distribution in the semi-ON state. EMC simulations were performed with the device biased in the semi-ON (V_{GS} = -2.0 V, V_{DS} = 20 V) for temperatures ranging from 250 K to 600 K. The carrier energy distributions at the end of the gate on the G-D access region side are shown as a function of the device temperature in Fig. VI-6 (a). Fig. VI-6 (b) focuses on the high energy (> 2 eV) carrier distribution tail portion of Fig. VI-6 (a).

As the temperature increases, the number of moderately energetic carriers (0.5 to 2.5 eV) increases. On the other hand, the number of higher energy (> 2.5 eV) carriers decreases with the increase in temperature. In Fig. VI-6 (b), the 600 K semi-ON stress result shows significantly fewer high energy carriers compared to the lower temperatures. The number of moderately energetic electrons keeps increasing with the device temperature till 450 K. There is no mid-energy carrier peak at 500 K and above. Above 500 K, there is an increase in the number of lower energy (less than 0.5 eV) carriers. The shape of the carrier-energy distribution changes very little as the temperature increases further.

a)

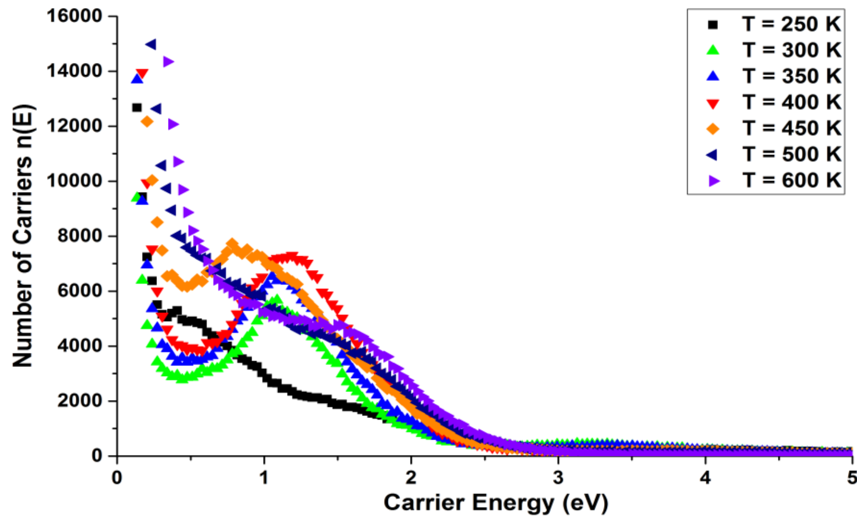

b)

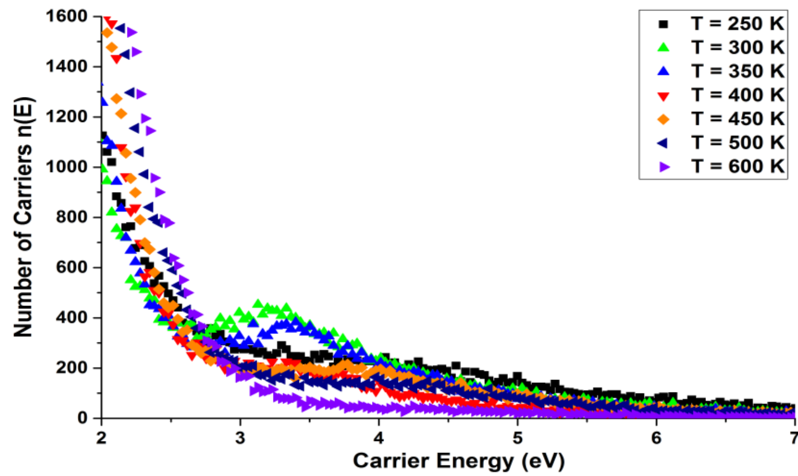

Fig. VI-6. (a) Carrier energy distribution for different temperatures in the semi-ON (V_{GS} = -2.0 V, V_{DS} = 20.0 V) condition sliced at the end of the gate on the G-D access region side. (b) Close-up view of the high energy carrier distribution region (greater than 2 eV) of Fig VI-6. (a) (After [24]).

Table VI-1 presents the number of carriers above a given energy value for different temperatures at semi-ON. Fig. VI-7 shows the plot for this table. This figure is helpful in understanding the effect of temperature on the energetic carriers. It is clear from the plot that the number of carriers above 2.5 eV decreases with increasing temperature, whereas the number of energetic carriers in the 'above 1.5 eV to above 2.0 eV' range is relatively unaffected by the device temperature.

TABLE VI-1

Number of carriers above a given energy level for different temperatures at semi-ON (V_{GS} = -2 V)

Greater than	T = 250 K	T = 300 K	T = 350 K	T = 400 K
0.5 eV	152000	184000	203000	214000
1.0 eV	91800	129000	141000	152000
1.5 eV	59500	64500	65300	67900
2.0 eV	36200	35400	33100	25800
2.5 eV	25100	26200	21000	12900
3.0 eV	19200	20800	16400	9020

There is a peak in the carrier distribution at about 1.0 to 1.4 eV for temperatures up to 450 K. As described before, this phenomenon is due to electrons getting accumulated in the *A*-valley (Fig. V-2), as the bottom of the *A*-valley is approximately 1.3 eV from the bottom of the conduction band (*Γ*-valley). Only at about 500 K, the optical phonons gain the energy to scatter these electrons (Fig. V-3). Hence, there is not a distinct peak for 500 K and 600 K. Instead, there is an increase in low energy carriers (less than 0.5 eV) for 500 K and 600 K. Fig. 8 summarizes the trend of change in carrier distribution with the increase in device temperature. Both high and moderate energy carriers can create or reconfigure defects if the defect activation energy is sufficiently low.

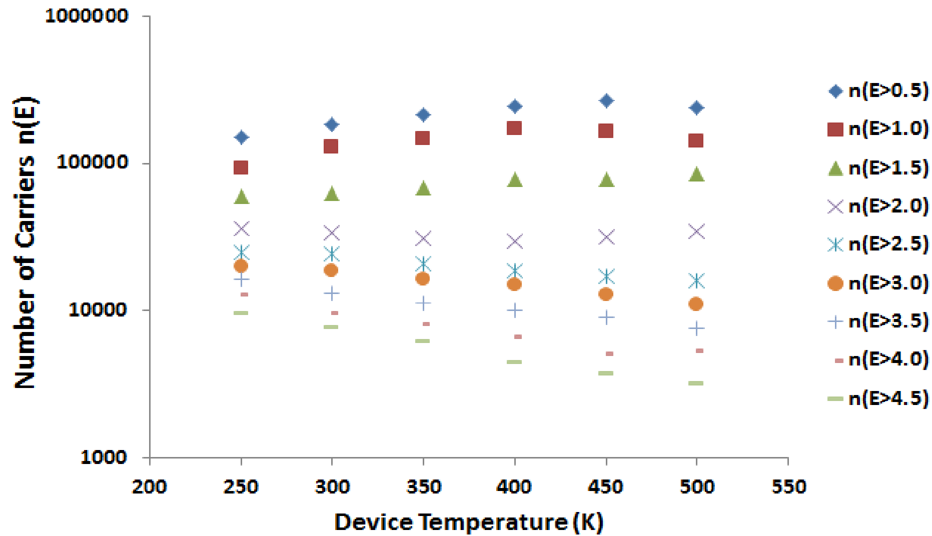

Fig. VI-7. Number of carriers with energies greater than the specified value (in steps of 0.5 eV) over the temperature range of 250 K to 500 K (After [24]).

6.5 Carrier Energy Distribution (Doping Dependence)

Next, the impact of varying the doping in the GaN and AlGaN layer on the carrier energy distribution has been investigated. In this case, we increase the doping level in the GaN and AlGaN from 10^{15} cm^{-3} to 10^{16} cm^{-3} (donor type) and run the simulations. We use the semi-ON stress conditions, and keep the temperature at 300 K. The results (Fig. VII-1) indicates that increasing the doping in the AlGaN has relatively no impact on the carrier distribution. On the other hand, increasing the doping in the bulk (GaN) has a reasonable impact on the distribution. The number of moderate energy carriers increases whereas the number of high energy carriers decreases as the doping in the bulk increases.

a)

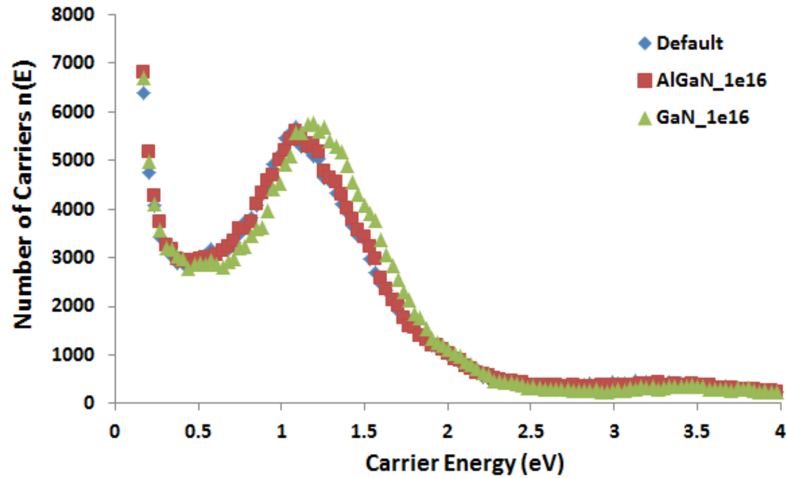

b)

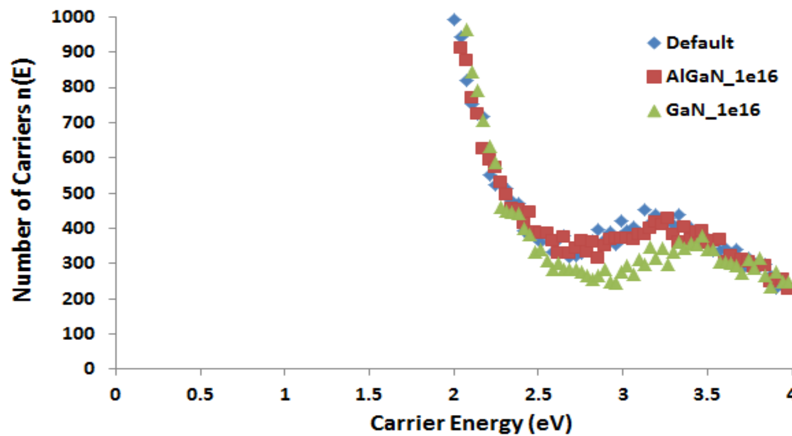

Fig. VI-8. (a) Carrier energy distribution for different GaN and AlGaN donor density in the semi-ON (V_{GS} = -2 V, V_{DS} = 20 V) condition sliced at the end of the gate on the G-D access side. (b) Close-up view of the high energy carrier distribution region (above 2 eV) of Fig VI-8. (a).

6.6 Carrier Energy Distribution (Geometry Dependence)

We also investigated the impact of the variation in the device dimensions on the carrier energy statistics. The impact of changing the access region lengths on the distribution has been investigated. The simulations were carried out at semi-ON condition (V_{GS} = -2 V, V_{DS} = 20 V). The device temperature is kept at 300 K. We initially keep the G-D access region and the gate lengths constant (from Fig. V-4) and vary the G-S access region lengths. G-S access region length of 0.35 µm was the dimension of our original device.

Fig. VI-9 reports the results of the simulations. The carrier energy distribution is obtained at the end of the gate on the G-D access region side in all three cases. Varying the G-S access region length has minimal effect on the carrier energy distribution. The reason is the lateral electric field at the gate-edge on the drain side remains unaffected with the change in G-S access region length, as long as the G-D access region length remains constant. Similarly, varying the gate length has limited impact on the distribution too. However, varying the G-D access region length has a slightly higher impact on the carrier distribution. The number of energetic carriers increases as the G-D access region length decreases.

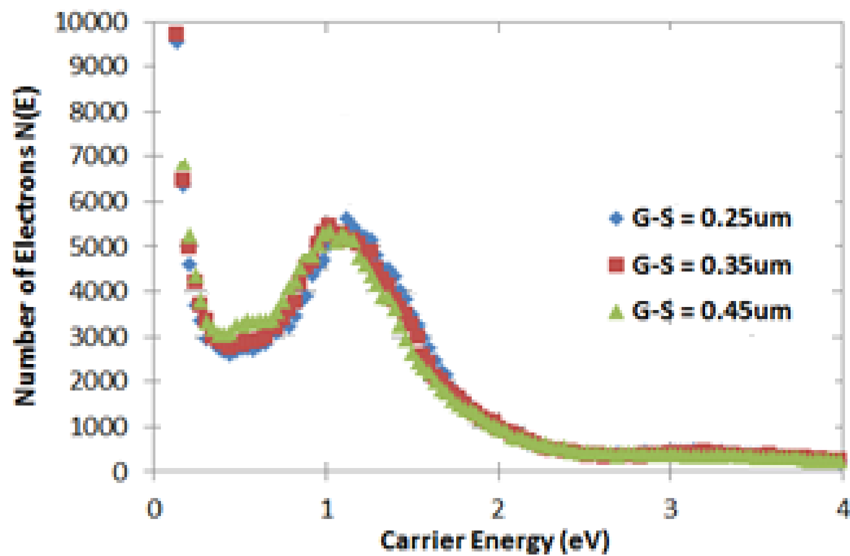

Fig. VI-9. Carrier energy distribution for different device geometry (access region lengths) in the semi-ON (V_{GS} = -2 V, V_{DS} = 20 V) condition sliced at the end of the gate on the G-D access region side (at room temperature).

6.7 Carrier Energy Distribution (Drain Bias Dependence)

Finally, the impact of drain bias on the carrier energy distribution has been explored. For consistency, V_{GS} was maintained at -2 V. We keep the device dimensions and the temperature constant, and vary the V_{DS} from 10 V to 30 V. Fig. VI-10 reports the results of the simulations. It can be observed that the medium energy carrier peak increases with the increase in the drain bias. But above 21.5 V the medium energy carrier peak suddenly disappears and we see a significant increase in the number of lower energy carriers. Above 25 V, the carrier energy distributions do not change much with the change in the value of V_{DS}.

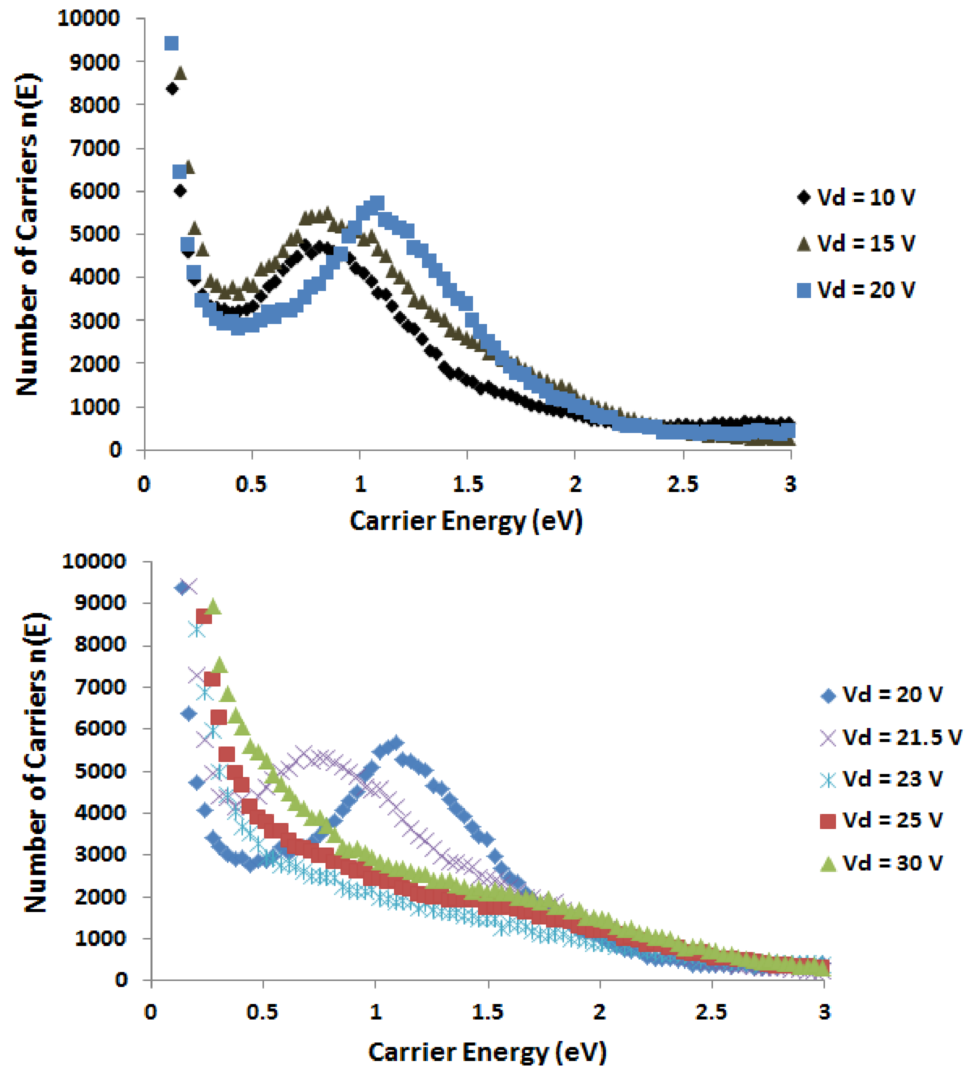

Fig. VI-10. Carrier energy distribution for different drain bias values for V_{GS} = -2.0 V, sliced at the end of the gate on the G-D access region side (at room temperature).

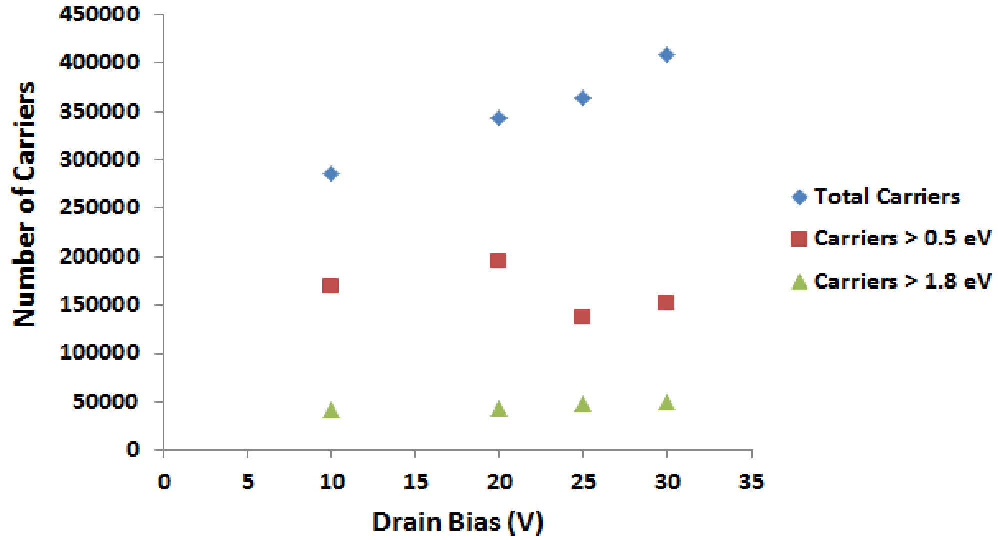

Fig. VI-11. Comparison of high energy (E > 1.8 eV), medium energy (E > 0.5 eV) and total number of carriers obtained for different drain bias values obtained at V_{GS} = -2.0 V, sliced at the end of the gate on the G-D access region side.

Fig. VI-11 summarizes the variation of carriers with the drain bias. The total number of carriers at the gate-edge increases with increase in the drain bias. The number of carriers with energies above 0.5 eV is highest at V_{DS} = 20 V. Above 20 V, this number decreases sharply. On the other hand, the number of energetic carriers (above 1.8 eV) keeps increasing with the increase in the drain bias. The next chapter describes how the information related to the carrier energy distribution can be used to estimate the scattering cross-section of the defect.

CHAPTER VII

EXTRACTION OF SCATTERING CROSS-SECTION

This chapter explains the first step of the degradation modeling procedure, i.e., calculation of the scattering cross-section of the defect present in the device. For extracting the scattering cross-section, it is important to identify the defect and calculate the activation energy of the defect. This chapter also gives an overview of the steps involved in the calculation of the barrier for hydrogen depassivation, which involves ab-initio DFT calculations. The impact of this activation energy as a modeling parameter is also described in the chapter.

7.1 Energy-Independent Scattering Cross-Section

The scattering cross-section (σ) of the defect in the device can be calculated from the V_T shift data of a stress experiment. The equations used for estimating the scattering cross-section of the defect has been derived in chapter IV. As explained before, the defect cross-section is modeled as being energy-independent for simplicity. Thus, the scattering cross-section is assumed to be zero for energies up to E_{act} and constant for the higher energies. The equations VII-1 and VII-2 gives the V_T shift equation assuming the cross-section is a simple step function:

$$\Delta V_T(t) = \frac{q\, d_{AlGaN}}{\varepsilon}\left[N_d^{\infty} - N_d(0)\right]\left(1 - e^{-\frac{t}{\tau}}\right) \qquad \text{(VII} - 1\text{)}$$

$$\frac{1}{\tau} = \sum_{E > E_{act}} n(E, T, V_{GS}, V_{DS})\; v(E)\boldsymbol{\sigma} \qquad \text{(VII} - 2\text{)}$$

Equation VII-1 can be used to fit the stress test data (V_T shift), and the value of the time constant (τ) can be calculated from the exponential dependence using equation VII-2. Then, using first principles DFT calculation we compute the activation energy (E_{act}) of the defect. Using this information and the results of EMC simulation results the value of σ can be determined.

7.2 Defect Activation Energy Calculation: Ab-initio DFT

For each candidate defect the energy barrier for depassivation (hydrogen removal) is determined using first-principles Density Functional Theory calculations were performed using VASP (Vienna Ab-Initio Simulation Package) [35]. These calculations employ the Perdew-Burke-Ernzerhof (P-B-E) version of the generalized gradient approximation (GGA) exchange-correlation functional [36], and include corrections for the zero-point vibrational contribution for hydrogen migration in GaN [37], [38].

The Nudged Elastic Method (NEB) is employed for the relevant defect activation processes [39]. Ultra-soft pseudopotentials were used to replace core electrons. The plane-wave basis energy cut-off was set at 348 eV. Supercells containing 128 atoms in a Wurtzite structure were used. A single k-point at 2π/a (¼, ¼, ¼) was employed for the Brillouin zone integrations. Atomic positions were relaxed until the configuration energy difference was less than 10^{-4} eV. The hybrid functional HSE06 was used for calculations to reproduce the correct value of the band gap, which is underestimated in the local density approximation. A correct value of the band gap is necessary to identify the position of electron levels near the conduction band. The defect formation energy is calculated as a function of the position in the band gap using [37], [40],

$$E^f\left[D_{Ga}^q V_N^x I^y\right] = E_{tot}\left[D_{Ga}^q V_N^x I^y\right] - E_{tot}^{bulk} + \mu_{Ga} + x\mu_N - y\mu_I + q(E_F + E_V) \qquad (VII-3)$$

where $E_{tot}\left[D_{Ga}^q V_N^x I^y\right]$ is the total energy of the supercell with defect with charge q at a gallium site, with or without (x = 0,1) a nitrogen vacancy and an impurity (hydrogen or oxygen) (y = 0,1) atom. E_{tot}^{bulk} is total energy of the supercell containing only bulk GaN. For Ga-rich fabrication conditions the Ga chemical potential (μ_{Ga}) is chosen to represent metallic orthorhombic Ga. The impurity chemical potential for O_2 or H_2 is chosen to correspond to the gas environment. Chemical potentials depend on the defect under investigation. For instance, if the defect is a N in a Ga site then only the chemical potential of Ga and N are required [40], [41].

To overcome the band gap problem, we use the ‘standard candle, method where we first choose the gallium vacancy as the standard candle defect below the midgap levels and the nitrogen vacancy as the standard candle defect for levels above midgap. We locate the valence band maximum for each defect by calculating the change in the local potential (ΔV) far from the defect and aligning the band edge from a GaN perfect crystal calculation. The alignment correction strongly depends on the charge state of the defect and varies from -0.2 to 0.1 eV. The conduction band is fixed using the experimental band gap. Then, the standard candle defect is shifted by δE_{shift} to fit the experimental level. Finally, all corresponding defect levels for are also shifted by the same δE_{shift} value. The accuracy of this method depends on defect levels having the same shifts as the standard candle defects [39]-[41].

As an example, we consider the case where electrons dehydrogenate a Ga vacancy hydrogen complex (N-rich devices, with positive V_T shift), Fig. VII-1 (a) and (b) that shows the atomic configurations and the energy barrier for the H removal from substitutional O_N in $Al_{0.30}Ga_{0.70}N$. First-principle calculations show that the energy barrier of hydrogen removal from the Ga vacancy hydrogen complex is E_{act} = 2.7 eV and energy barrier for the removal from oxygen complex is E_{act} = 2.1 eV. The V_T of the devices grown in N-rich conditions have negative shifts, as shown in Fig. III-4. These negative shifts are attributed to reconfiguration of O_N–H complexes, namely the H removal and subsequent increase in the concentration of O^{+1}_N [26].

In the next example, the process described is dehydrogenation of substitutional oxygen (Ga-rich devices, with negative V_T shift), with the energy barrier of initial step calculated to be about 0.5 eV. Fig. VII-2 shows the energy barrier for H removal from substitutional oxygen in AlGaN. The initial step is shown in Fig. VII-2 (a) and further removal is shown in Fig. VII-2 (b). We consider the E_{act} for the complete removal of H atom, as described in ref. [15]. The barrier for the complete removal of H is about 2.1 eV. The activation step controlling V_T and g_m degradation corresponds to the initial process.

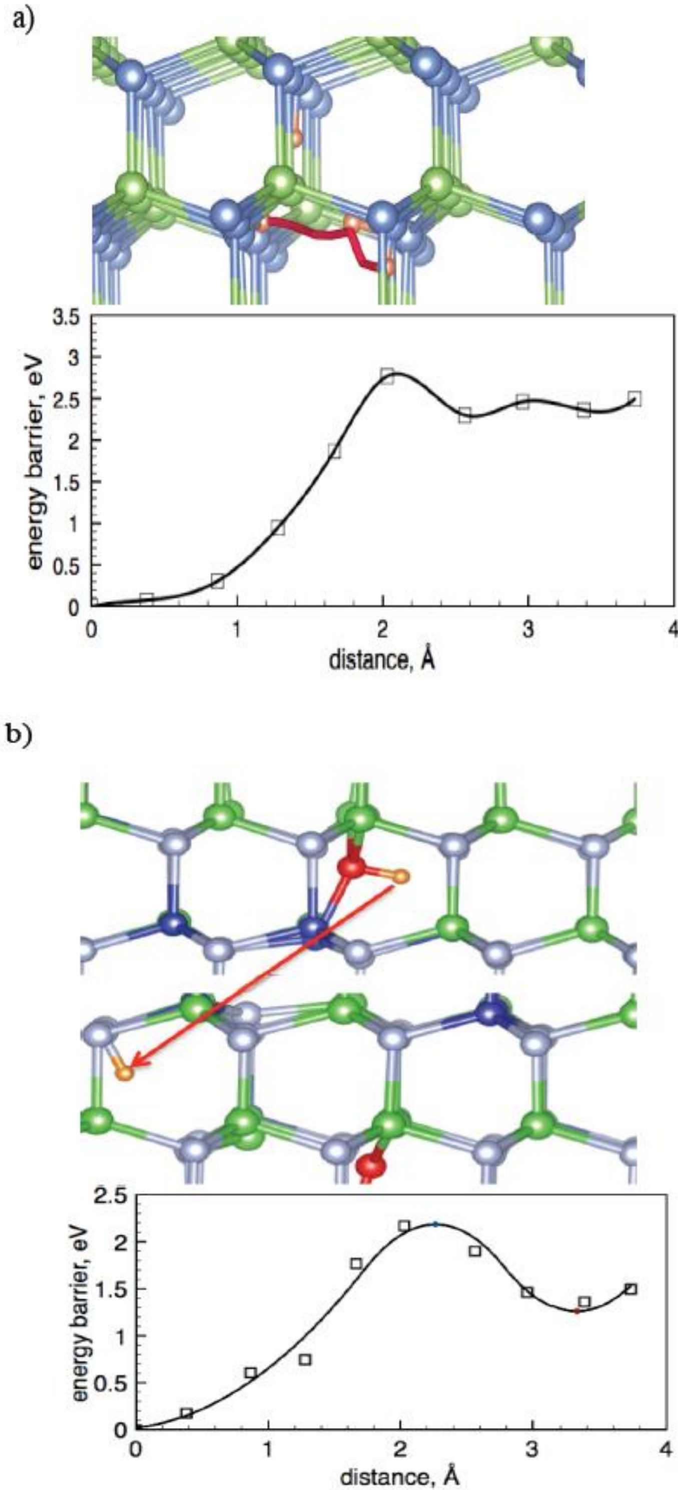

Fig. VII-1. (a) Atomic configuration and the corresponding migration energy barrier of a doubly hydrogenated Ga vacancy (for N-rich devices) in GaN. The red line highlights the H removal path and energy barrier along the path. (b) Atomic configuration and barrier of hydrogenated substitutional oxygen in AlGaN. The red arrow shows the removal of H to the next cell. The barrier is calculated along the path between initial and final positions of H. Colors used, Ga: Green, N: Blue, H: Orange, Al: Dark Blue [26].

a)

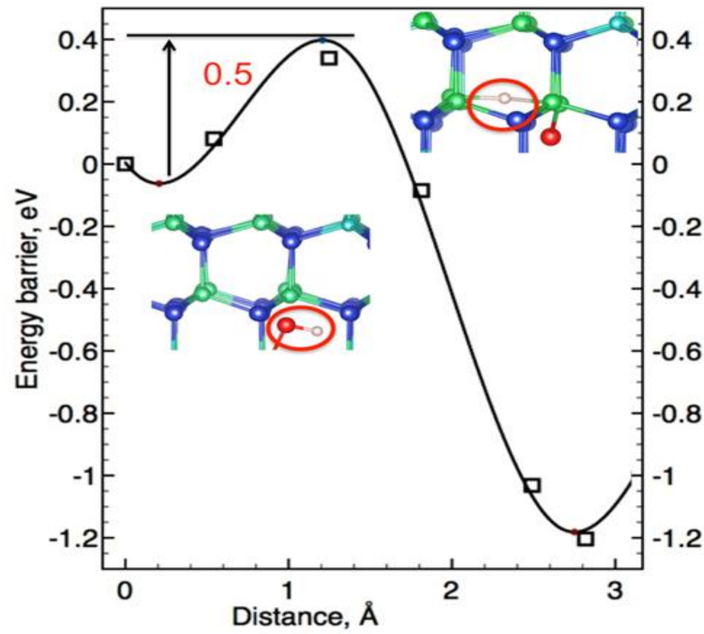

b)

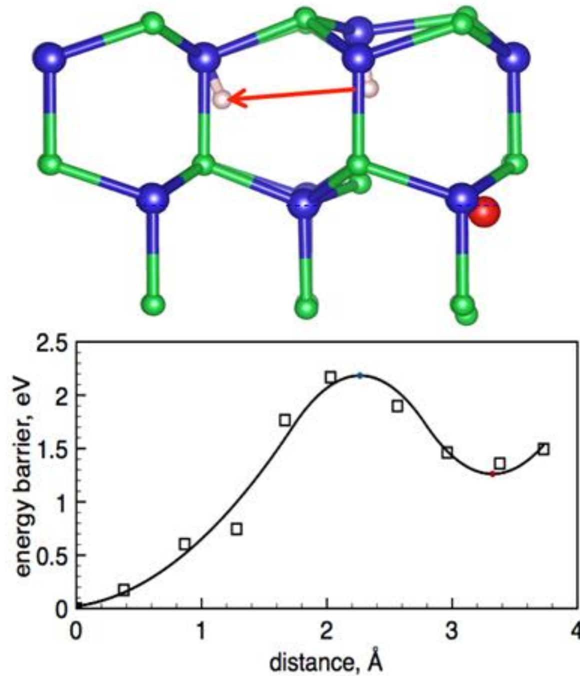

Fig. VII-2. (a) Energy barrier for electron-activated removal for hydrogen in GaN from first-principles DFT calculations using VASP. The figure shows the atomic configuration of hydrogenated substitutional oxygen (for Ga-rich devices), with Al atoms shown in dark blue. The red circle shows the position of H. The energy barrier is calculated along the path between initial and final positions of the H. The activation barrier for the initial step of removal process is 0.5 eV. (b) Barrier and defect reconfiguration for H to move further from O defect. The calculated barrier for this complete removal is 2.1 eV (After [27]).

7.3 Scattering Cross-Section Calculation

This section presents the values of extracted scattering cross-section, and how they vary from device to device. As an example, consider the case of Ga-rich devices. Fig. VII-3 presents the V_T shift data from semi-ON stress (at room temperature) for three Ga-rich HEMTs. Even though the device dimensions and growth techniques were identical, the device-to-device variation in the degradation trend can be observed from the figure. Since, these devices are Ga-rich and the V_T shift direction is negative, we can conclude that the likely defect in these devices is substitutional oxygen. From the DFT calculation results (Fig. VII-2), we know that the initial barrier for H removal for this defect is 0.5 eV. Now equation VII-1is used to fit the three V_T shift results using E_{act} of 0.5 eV. The corresponding value of $\Sigma n(E)v(E)$ for 0.5 eV can be obtained from the EMC simulation results. The value of cross-section (σ) can be calculated using equation VII-2 from the value τ of calculated from the fit. Fig. VII-3 presents the values for σ for the three devices. All the values are in the 10^{-16} cm^2 range, which is consistent with the numbers reported in the literature for defects in GaN. The value of σ is higher for devices which show greater V_T shift within the same stress time. We will use the V_T shift result for device # 3 to explain the dependence of activation energy on the modeling process.

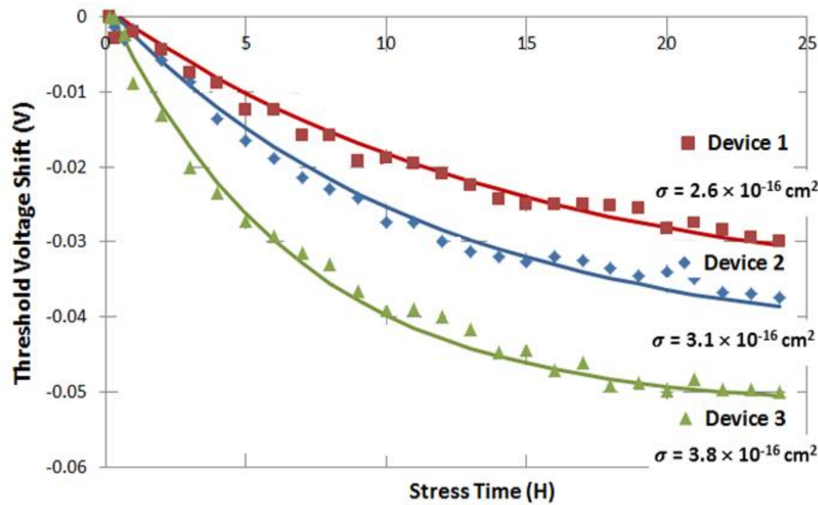

Fig. VII-3. Exponential fits to the semi-ON stress (V_{GS} = -2 V, V_{DS} = 20 V) results for the three Ga-rich devices, and the corresponding extracted scattering cross-section values. Activation energy of 0.5 eV has been considered for the calculation (After [26]).

7.4 Activation Energy as a Modeling Parameter

The accurate estimation of the defect activation energy is important in calculating the scattering cross-section. In this study we consider several hypothetical defects with different activation energies (in steps of 0.5 eV) and calculate the scattering cross-section values from the fit to the V_T degradation result of the Ga-rich device # 3. Even in this case we consider that the defect cross-section is independent of carrier energy. The number of carriers with energies higher than the activation energy of each hypothetical defect at semi-ON (Table VII-1) is mentioned below. The calculated cross-section values for different activation energies are shown in Fig. VII-4. The value of σ varies a lot with the value of E_{act}, especially for defects with high activation energies (greater than 2 eV).

TABLE VII-1

Number of carriers above a given energy level for semi-ON (V_{GS} = -2 V, V_{DS} = 20 V) at 300 K.

Greater than	Number of Carriers
0.5 eV	184000
1.0 eV	129000
1.5 eV	64500
2.0 eV	35400
2.5 eV	26200
3.0 eV	20800
3.5 eV	12300

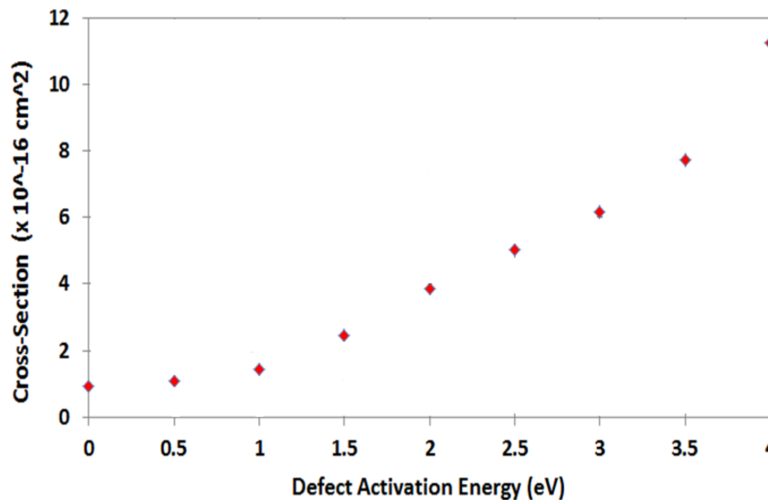

Fig. VII-4. Extracted scattering cross-section values from the fit to Device # 3 (Ga-rich) semi-ON stress data for eight hypothetical defects with different activation energies.

7.5 Energy-Dependent Cross-Section

So far in our calculations we have considered the scattering cross-section (σ) to be independent of carrier energy for simplicity. In other words, we were treating σ as a step function. In this section σ is calculated considering a more realistic distribution with a dependence on carrier energy E. Equations VII-4 and VII-5 are used to describe the new σ. The result of V_T shift for the Ga-rich device # 3 has been used for the calculations.

$$\text{For } E < E_{act}, \sigma(E) = e^{\left(\frac{E-E_{act}}{kT}\right)} \sigma \qquad (\text{VII}-4)$$

$$\text{For } E > E_{act}, \sigma(E) = \sigma \qquad (\text{VII}-5)$$

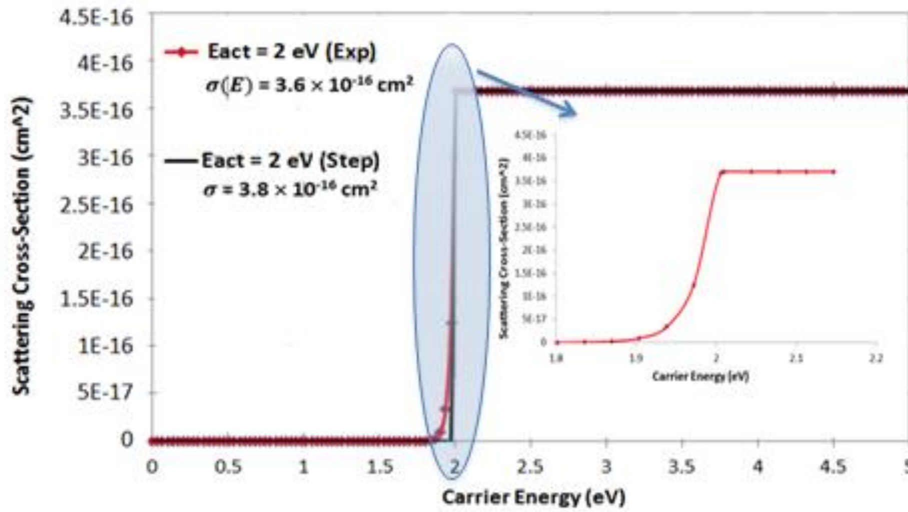

Fig. VII-5. Impact on the extracted scattering cross-section values from the fit to the Device # 3 semi-ON stress data when the cross-section is assumed to be energy-dependent.

Fig. VII-5. presents the distribution profiles for the two cases. The calculations show that the difference in the calculated cross-sections for the two cases is relatively small. The likely explanation for this observation is the very fast rise of the exponential for $E<E_{act}$, as shown in Fig. VII-5. So, it can be concluded that using an energy-independent cross-section (for simplicity) will not have a significant impact on the predictive modeling results. The next three chapters describe how the extracted value of the scattering cross-section can be utilized to model degradation at different operating conditions.

CHAPTER VIII

THRESHOLD VOLTAGE DEGRADATION MODELING

This chapter provides the procedure for the predictive modeling of the V_T as well as the results of the degradation modeling process considering the bias dependence. The results of the predictive model are then compared to the experimental results for similar stress conditions in order to verify the accuracy of the model. This chapter provides this comparison for three sets of devices fabricated using different process conditions.

8.1 Predictive Model for V_T Shift: Bias-Dependence

For predicting the bias-dependence of the devices we use equation VIII-1, which has been derived from the equation IV-1. Equation VIII-1 shows an exponential dependence of the V_T shift with the stress time, which is obtained from the number of carriers that exceeds the activation energy of the defect for a given gate bias (V_{GS}) using equation VIII-2:

$$\Delta V_T(t) = \frac{q\ d_{AlGaN}}{\varepsilon}[N_d^{\infty} - N_d(0)]\left(1 - e^{-\frac{t}{\tau}}\right) \qquad (\text{VIII} - 1)$$

$$\frac{1}{\tau} = \sum_{E>E_{act}} n(E, T, \boldsymbol{V_{GS}}, V_{DS})\ v(E)\sigma \qquad (\text{VIII} - 2)$$

Once we have established the type of defect present in the device and calculated the scattering cross-section based on the estimated activation energy, the degradation at different gate bias conditions can be predicted by simply substituting the value of $\Sigma\ n(E)v(E)$ obtained for all $E>E_{act}$, assuming the cross-section to remain constant. The same procedure can be extended to model the drain bias (V_{DS}) dependence of degradation too. The maximum shift in V_T is determined by the number of pre-cursor defects in the device obtained from the unstressed V_T, which is considered constant for the bias-dependence modeling.

8.2 Results of Predictive Modeling

Once the type of defect present in the device has been stablished and the scattering cross-section based on the estimated activation energy has been calculated, we can predict the degradation at different gate bias conditions by substituting the value of $\Sigma\, n(E)v(E)$ obtained for all $E>E_{act}$ in equation VIII-1, assuming the cross-section to remain constant. Fig. VIII-1 shows the trend in the change in the value of $\Sigma\, n(E)v(E)$ with respect to the activation energies of hypothetical defects for all the bias conditions that have been considered. This value is maximum for V_{GS} = -2 V irrespective of the defect activation energy.

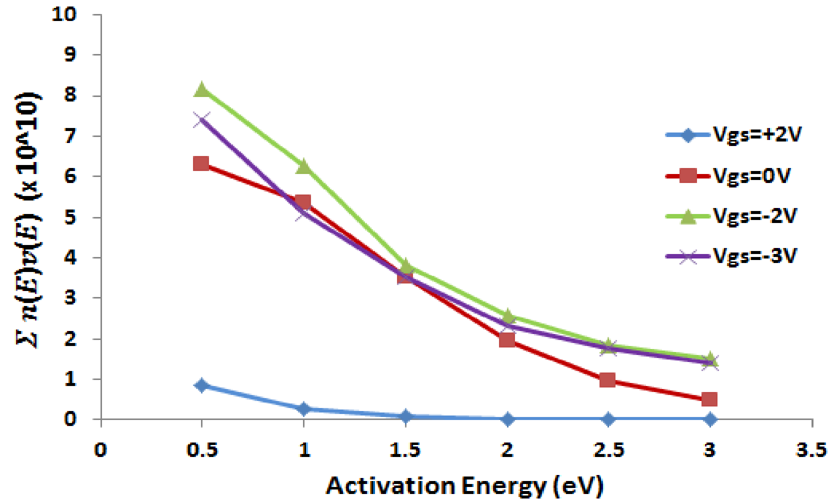

Fig. VIII-1. The values of summation of product of number of carriers and their velocities obtained for different V_{GS} values considering six hypothetical defects with different E_{act}.

We initially consider the case of N-rich devices from our first batch for the predictive modeling exercise. For the N-rich devices, the ab-initio DFT calculations showed that the hydrogenated Ga-vacancy with activation energy of 2.7 eV is the likely defect. We first fit the semi-ON stress data at 300 K using the equation VIII-1. The scattering cross-section of the defect (σ) calculated (using the equation VIII-2) from the value of time constant obtained from the fit is 1.2 x 10^{-15} cm^2. Now, we can use equations VIII-1 and VIII-2 again to determine the degradation at different bias conditions by simply plugging the value of $\Sigma\, n(E)v(E)$ for the corresponding bias condition considering the activation energy of 2.7 eV (from Fig. VIII-1).

Fig. VIII-2 shows the V_T shift predictions for the other gate bias values at 300 K obtained with the model by keeping the value of the defect scattering cross section constant. The results clearly show that the initial degradation is slower for all the other values of V_{GS}, as compared to V_{GS} = -2 V. All the predictions are made for V_{DS} of 20 V. All the predicted curves reach the same saturation value, but at different rates. The saturation point is determined by the number of available defects in the device, which is considered to be the same for all the devices as long as the process conditions and the operating temperatures are the same. The time taken to reach this value depends on the number of energetic carriers above the defect activation energy at the specified value of V_{GS}. This explains why the degradation rate is so slow for the ON condition (V_{GS} = +2 V). Virtually no degradation is expected in the ON condition, as there are very few carriers (above 2.7 eV) that can create or modify defects by hydrogen depassivation. The V_{GS} = 0 V prediction curve reaches the saturation value in about 20 hours whereas the V_{GS} = -3 V curve takes around nine hours to reach this saturation point. We will later check the consistency of the model by comparing the predicted results with the stress experiment results for the corresponding gate bias conditions for V_{DS} = 20 V.

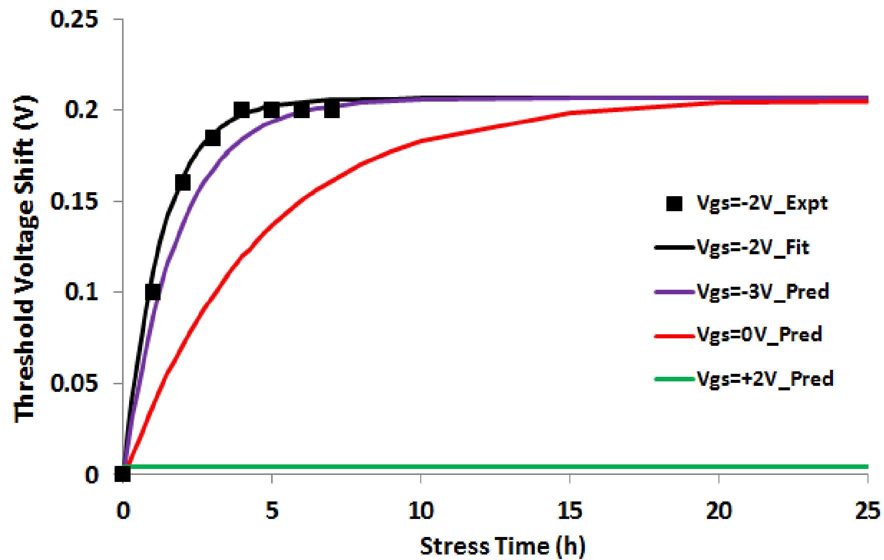

Fig. VIII-2. The V_T shift predictions (for the N-rich devices) obtained for different values of V_{GS} at 300 K (for V_{DS} = 20 V). The predictions are based on the scattering cross-section value obtained from the exponential fit to the semi-ON (V_{GS} = -2 V) stress experiment data (black). The value of σ extracted from the fit to the V_{GS} = -2 V stress data is 1.2 x 10^{-15} cm^2.

Next we consider the case of Ga-rich devices for predictive modeling. For the Ga-rich devices, the V_T shift is in the opposite direction as that of the N-rich devices. So, there is a net build-up of positive charge at the interface due to the applied stress. The DFT calculations show that substitutional oxygen is the likely defect in these devices. The energy barrier for this defect is about 0.5 eV. Again, the V_{GS} = -2 V stress test data was fitted using the equation VIII-1 and calculate the scattering cross-section. The value of σ obtained is 3.8 x 10^{-16} cm^2. Next, we use the value of $\Sigma\, n(E)v(E)$ for the corresponding bias condition considering the activation energy of 0.5 eV (from Fig. VIII-1) and determine the respective prediction in shifts.

Even in this case, the predictions are made for V_{DS} of 20 V at room temperature. Even in the case of Ga-rich devices the rate of degradation is greatest in the semi-ON state of operation and the degradation is negligible in the ON condition (V_{GS} = +2 V). The predicted shifts do not show saturation within 24 hours. For the N-rich devices, the V_T shift predictions saturated within 18 hours. On the other hand, the maximum value of degradation (shift in V_T) for the Ga-rich devices is much less (about 25%) than the N-rich devices. This can be attributed to lesser number of pre-existing and available defects in the N-rich devices when the stress test started.

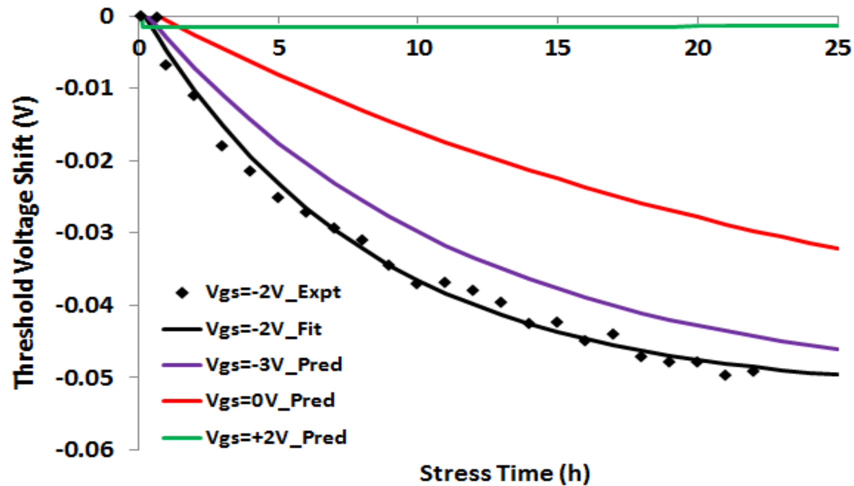

Fig. VIII-3. The V_T shift predictions (for the Ga-rich devices) obtained for different values of V_{GS} at 300 K (for V_{DS} = 20 V). The predictions are based on the scattering cross-section value obtained from the exponential fit to the semi-ON (V_{GS} = -2 V) stress experiment data (black). The value of σ obtained from the semi-ON fit is 3.8 x 10^{-16} cm^2.

Table VIII-1 summarizes the values of available defect concentration and the estimated values of time constants for the other bias conditions for the Ga-rich device. The values of $1/\tau$ increase as V_{GS} is becomes more negative.

TABLE VIII-1

Number of benign defects and the calculated values of time constant for different values of V_{GS}.

V_{GS}	$N_d^{\infty} - N_d(0)$	Σ n(E) v(E)	$1/\tau$
+2.0	4.26 x 10^{16}	0.72 x 10^{9}	0.073
0	4.26 x 10^{16}	6.21 x 10^{10}	0.467
-2.0 *	4.26 x 10^{16}	8.12 x 10^{10}	*0.648*
-3.0	4.26 x 10^{16}	7.58 x 10^{10}	0.626

8.3 Comparison with Experimental Results

It is important to verify the results obtained from the predictive model. For this, we compare the predicted results with the stress experiment results for the corresponding gate bias conditions. We use devices of similar dimensions and processing conditions for consistency. Figures VIII-4 and VIII-5 show the comparison between the predicted results and experimental data for N-rich and Ga-rich devices respectively. The stress test data show good agreement with the predicted values for the N-rich devices. For the Ga-rich device, the stress test data deviates slightly from the predicted path.

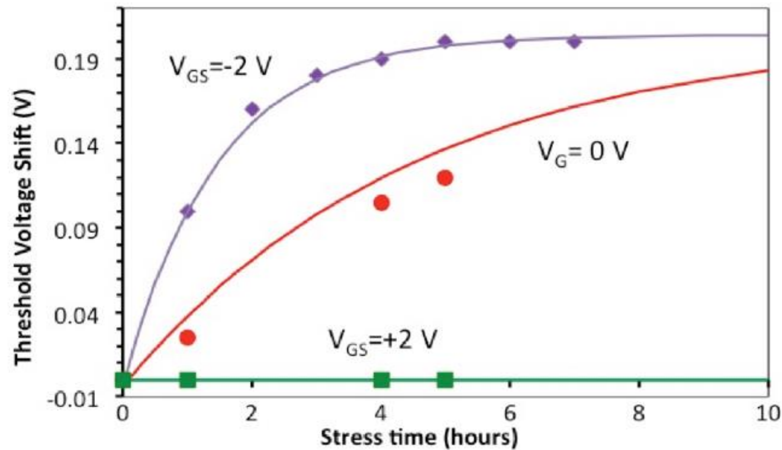

Fig. VIII-4. Comparison of experimental results (for V_{DS} = 20 V) with V_T shift predictions (N-rich devices) obtained for different values of V_{GS} at 300 K.

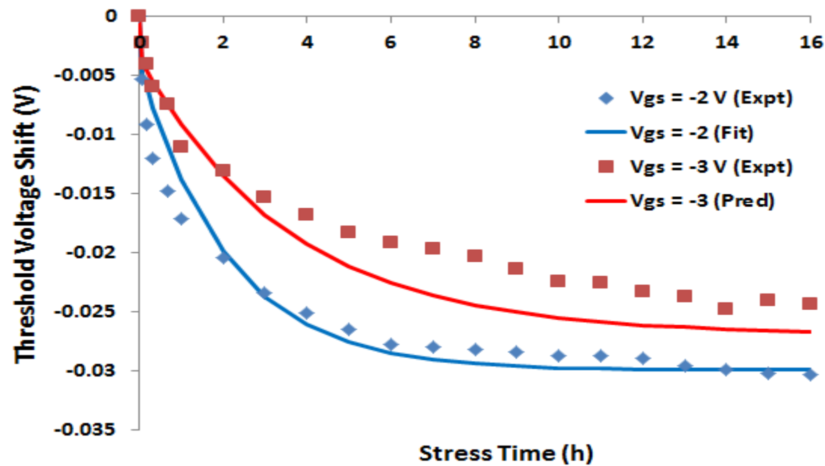

Fig. VIII-5. Comparison of experimental results (for V_{DS} = 20 V) with V_T shift predictions (Ga-rich devices) obtained for different values of V_{GS} at 300 K.

8.4 Prediction for Longer Duration Stress

We also modeled the long term degradation of these devices under semi-ON stress. In this case, we predict the shift in the V_T of a device under stress for more than two days from the V_T shift observed from the first 8-10 hours. Here, we consider the example of a Ga-rich device. The device is subjected to semi-ON (V_{GS} = -2 V, V_{DS} = 20 V) stress at room temperature for a few days, but only the first few hours of data was used for the modeling purpose.

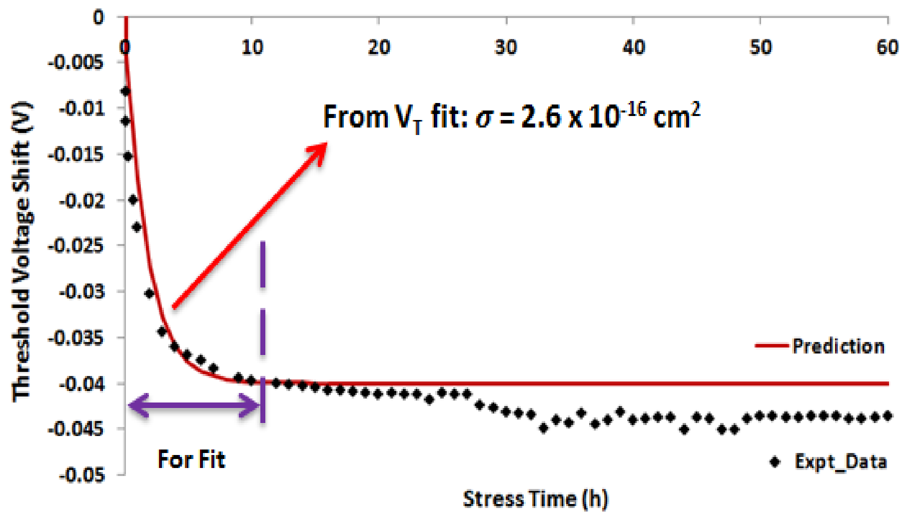

Fig. VIII-6. The long duration V_T shift prediction (Ga-rich) obtained for semi-ON (V_{GS} = -2 V) at 300 K (for V_{DS} = 20 V). The predictions are based on the scattering cross-section value obtained from the exponential fit to the first 10 hours of the stress experiment data.

We fit the data for the first 10 hours using equation VIII-1, and extract the value of the scattering cross-section (σ) of the defect in the device. The value of σ in this case is 2.6×10^{-16} cm^2. We keep the value of σ constant and only vary the stress time parameter t to obtain the long term degradation of the device. Fig. VIII-6 shows the comparison of the stress test data with the prediction curve. The prediction shows good agreement with the data till the 30 hour mark, at which time the stress experiment data shows a sudden deviation from the prediction. A similar trend was observed in devices fabricated under N-rich and NH_3-rich conditions too. This sudden bump in the V_T shift may be attributed to creation or modification of another defect following a long duration semi-ON stress. The next chapter describes how the model can be extended to predict the temperature-dependence of the V_T degradation.

CHAPTER IX

V_T DEGRADATION MODELING (TEMPERATURE-DEPENDENCE)

This chapter explains the procedure for predictive modeling of the V_T shift considering the temperature dependence. The results of the predictive model are then compared to the experimental results for similar temperature conditions in order to check the consistency of the model. The results shown in this chapter are mainly for the Ga-rich devices.

9.1 Predictive Model for V_T Shift: Temperature-Dependence

The procedure for predictive modeling of temperature is quite similar to that of modeling bias dependence. For predicting the temperature-dependence of the devices we use equation IX-1, which has been derived from the equation IV-1. Equation IX-1 shows an exponential dependence of the V_T shift with the stress time, which is obtained from the number of carriers that exceeds the activation energy of the defect for a given gate bias (V_{GS}) using equation IX-2:

$$\Delta V_T(t) = \frac{q\ d_{AlGaN}}{\varepsilon}[N_d^{\infty} - N_d(0)]\left(1 - e^{-\frac{t}{\tau}}\right) \qquad (IX-1)$$

$$\frac{1}{\tau} = \sum_{E>E_{act}} n(E, \boldsymbol{T}, V_{GS}, V_{DS})\ v(E)\sigma \qquad (IX-2)$$

Since, we already know the type of defect present in the device and calculated the scattering cross-section based on the estimated activation energy, we can predict the degradation at different temperatures by simply substituting the value of $\Sigma\, n(E) v(E)$ obtained for all $E>E_{act}$, assuming the cross-section to remain constant. The maximum shift in V_T is determined by the number of available defects in the device at the given temperature. This is dependent on the number of pre-cursor defects in the device, which can be obtained from the initial unstressed value of V_T at the specific temperature

9.2 Results of Predictive Modeling

Once we have established the type of defect present in the device and calculated the scattering cross-section based on the estimated activation energy, the degradation at different temperatures can be predicted by substituting the value of $\Sigma\, n(E)v(E)$ obtained for all $E>E_{act}$ in equation IX-1, assuming the cross-section to remain constant. Fig. IX-1 shows the trend in the change in the value of $\Sigma\, n(E)v(E)$ with respect to the activation energies of hypothetical defects for all the temperatures that we have considered (obtained from EMC, Fig. VI-6).

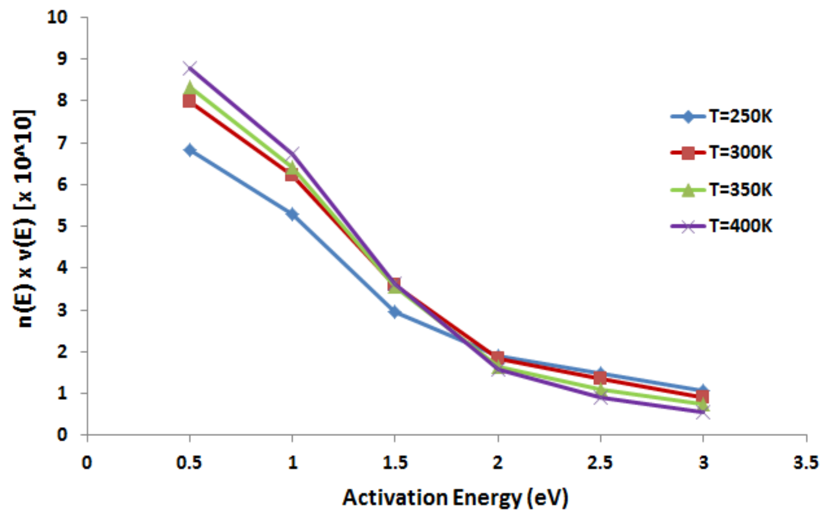

Fig. IX-1. The values of summation of product of number of carriers and their velocities obtained for different values of temperature considering six defects with different activation energies.

In this example, we consider the case of Ga-rich devices. For these devices, the DFT calculations showed that substitutional oxygen with activation energy of 0.5 eV is the likely defect. We first fit the semi-ON stress data at 300 K using equation IX-1. The scattering cross-section of the defect (σ) calculated (using the equation IX-2, Fig. IX-3) from the value of time constant obtained from the fit is 4.7 x 10^{-16} cm^2. Now, we can use equations IX-1 and IX-2 again to determine the degradation at different temperatures by utilizing the value of $\Sigma\, n(E)v(E)$ for the corresponding temperature considering the activation energy of 0.5 eV (from Fig. IX-1). The number of available defects can be computed from Fig. IX-2 (calculated from Fig. III-3). This quantity defines the maximum value of degradation at a given temperature.

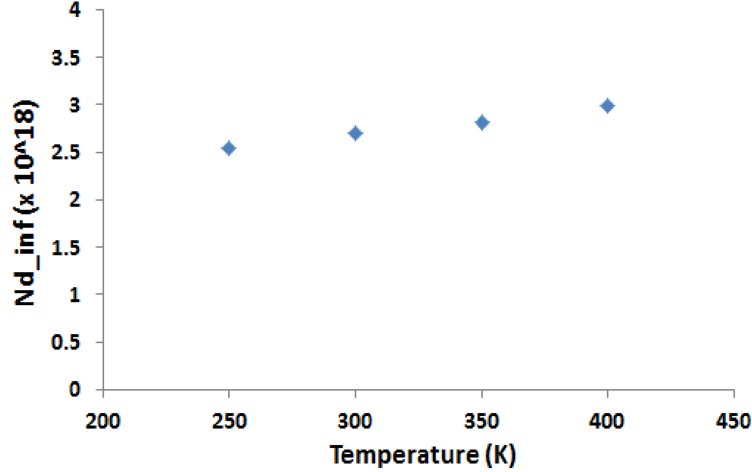

Fig. IX-2. The density of precursor defects (N_d^∞) for different device temperatures (for Ga-rich) obtained from the initial V_T values for the corresponding temperature (from Fig. III-3).

The density of the precursor defects in the device increases with the temperature. This is because the initial V_T (at $t = 0$) of the device increases with the temperature. Hence, the number of available defects initially (at $t = 0$) also increases with the device temperature. So, we expect the value of maximum degradation (V_T shift) to increase with the temperature. We neglect the impact of device-to-device variation. The time taken to reach this saturation is dependent on the carrier energy distribution, however. Table IX-1 summarizes the values for the available defect concentration and the time constants at different temperatures. The values for the 300 K data are obtained directly from the fit. The time constants for the other temperatures are obtained using the results of EMC temperature simulations. The value of 1/τ increases as the temperature increases. This is because the number of carriers with energies above the activation energy of substitutional oxygen (i.e., above 0.5 eV) in GaN increases with the increase in the device temperature.

TABLE IX-1

Concentration of available defects (at $t = 0$) and the calculated values of time constant for different temperatures at semi-ON. The values for 300 K are obtained directly from the fit.

Temperature	$N_d^\infty - N_d(0)$	Σ n(E) v(E)	*1/τ*
250 K	1.92 x 10^{16}	6.76 x 10^{10}	0.461
300 K	2.26 x 10^{16}	7.87 x 10^{10}	*0.548*
350 K	2.47 x 10^{16}	8.18 x 10^{10}	0.618
400 K	4.52 x 10^{16}	8.62 x 10^{10}	0.704

9.3 Comparison with Experimental Data

Next the V_T shift prediction (temperature) results were compared with the experimental data for the corresponding temperature. All the devices had similar dimensions and were Ga-rich. The devices were stressed at semi-ON (V_{GS} = -2 V, V_{DS} = 20 V), as this was the bias condition used in the simulations. Fig. IX-3 compares the results of the predictions with the stress experiment data. As explained earlier, the results were obtained based on the defect cross-section (σ) calculated from the fit to the 300 K semi-ON stress data.

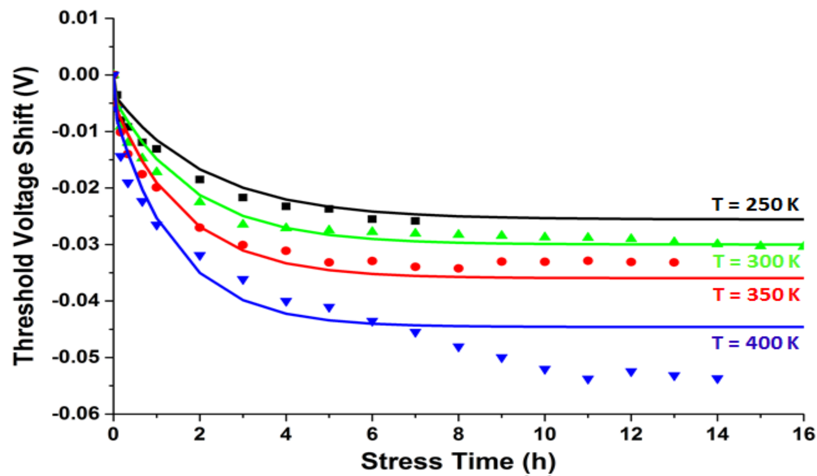

Fig. IX-3. V_T shift predictions (for Ga-rich devices) obtained for different temperatures at semi-ON (V_{GS} = -2 V, V_{DS} = 20 V) compared with the experimental data for the corresponding temperature. The predictions are based on the scattering cross-section value obtained from the exponential fit to the 300 K stress experiment data (green) considering an E_{act} of 0.5 eV.

The results from Fig. IX-3 indicate that the temperature stress experiment results show good agreement with the predicted degradation path for temperatures up to 350 K. At 400 K, the stress test results match the predictions for the first 5-6 hours only. Following that, there is an additional shift in the V_T with the stress time. So, it is clear that there is an additional build-up of positive charge at the interface at elevated temperatures. This may be due to generation or modification of additional defects at the elevated temperatures. This may be due to the significant increase in moderate energy carriers at elevated temperatures. Although these carriers are not very energetic, these are still capable of creating defects since the energy barrier for the initial removal of H in substitutional oxygen is low (0.5 eV).

Here we show an example of modeling the degradation with incorrect defect activation energy. In this example we consider the energy barrier for the complete removal of H as the activation energy. So, the temperature stress data was modeled with an E_{act} of 2.1 eV. The process of predictive modeling remains exactly the same as before. Fig. IX-4 presents the results of the new predictions compared with the same stress test results. The stress test data do not show good agreement with the new predictions for any temperature, not even during the initial degradation (4-5 hours). In the next chapter, we extend the model to predict the transconductance degradation by linking the threshold voltage shift to mobility reduction.

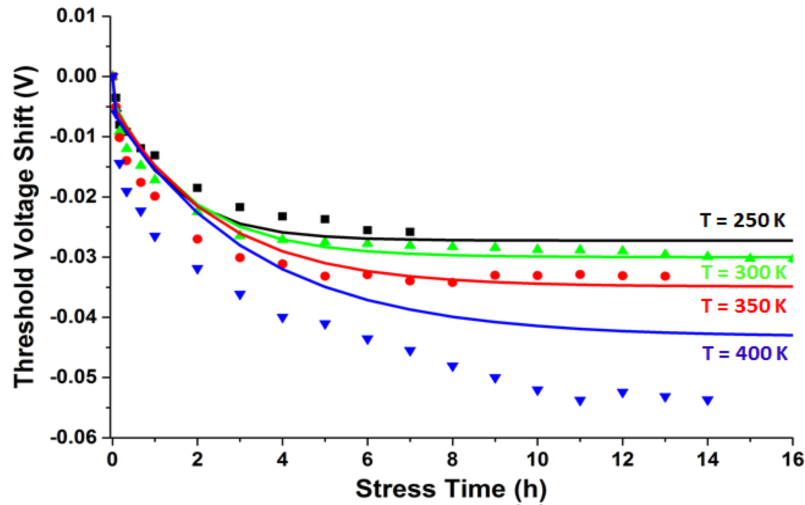

Fig. IX-4. V_T shift predictions (for Ga-rich devices) obtained for different temperatures at semi-ON compared with the experimental data for the corresponding temperature. The predictions are based on the scattering cross-section value obtained from the exponential fit to the 300 K stress experiment data (green) considering an E_{act} of 2.1 eV.

CHAPTER X

TRANSCONDUCTANCE DEGRADATION MODELING

As the experimental results showed, the observed V_T shifts are relatively small in these devices, but the corresponding degradation in g_m is significant and likely to be a concern in practical applications. Hence, it is important to model the effects of stress on the g_m degradation as well. This chapter provides the procedure for the predictive modeling of the g_m degradation with the stress time.

10.1 Transconductance Model: Relating g_m Degradation to V_T Shift

First, we determine whether the g_m degradation can be directly linked to the same defects in type and location as those that cause the V_T shift of the device. We first assume that both the effects are due to a correlated increase in the scattering from the same charged defects in type and location, and check for the self-consistency and plausibility of this assumption. The relationship between the effective mobility (μ) and the areal defect density $N_d(t)$ in the device can presented using Matthiessen's rule as follows [42]:

$$\mu = \frac{\mu_0}{1 + \alpha\, N_d(t)} \qquad (X-1)$$

where α is a proportionality constant related to the scattering strength and μ_0 is the pre-stress mobility. The equation X-1 can be rearranged to determine the change in mobility,

$$\frac{\mu_0 - \mu}{\mu} = \frac{\Delta\mu}{\mu} = \alpha\, N_d(t) \qquad (X-2)$$

The drain current (I_D) of the device in this region of transistor operation is given by [43],

$$I_D = \frac{\mu\, W\, \varepsilon}{2\, L\, d_{AlGaN}}\, [2(V_{GS} - V_T)V_{DS} - {V_{DS}}^2] \qquad (X-3)$$

where W is the width of the device and L is the channel length. The transconductance (g_m) of a transistor (in the linear region) can now be determined by differentiating the equation X-1 with respect to the gate voltage (V_{GS}),

$$g_m = \frac{\partial I_D}{\partial V_{GS}} = \frac{\mu\, W\, \varepsilon\, V_{DS}}{L\, d_{AlGaN}} \qquad (X-4)$$

The transconductance degradation ($\Delta g_m/g_m$) can be linked to the mobility reduction ($\Delta\mu/\mu$) using the following equation,

$$\frac{\Delta g_m}{g_m} = \frac{W\, \varepsilon\, V_{DS}}{L\, d_{AlGaN}} \frac{\Delta\mu}{\mu} \qquad (X-5)$$

The transconductance degradation in the linear region of operation can be linked to the defect density $N_d(t)$ using the equation,

$$\frac{\Delta g_m}{g_m} = \frac{W\, \varepsilon\, V_{DS}}{L\, d_{AlGaN}}\, \alpha\, N_d(t) \qquad (X-6)$$

Using this equation the g_m degradation can be linked to the V_T shift, which gives a linear relationship between the two quantities,

$$\frac{\Delta g_m}{g_m} = \alpha \frac{W\, \varepsilon^2\, V_{DS}}{q\, L\, {d_{AlGaN}}^2}\, V_T(t) \qquad (X-7)$$

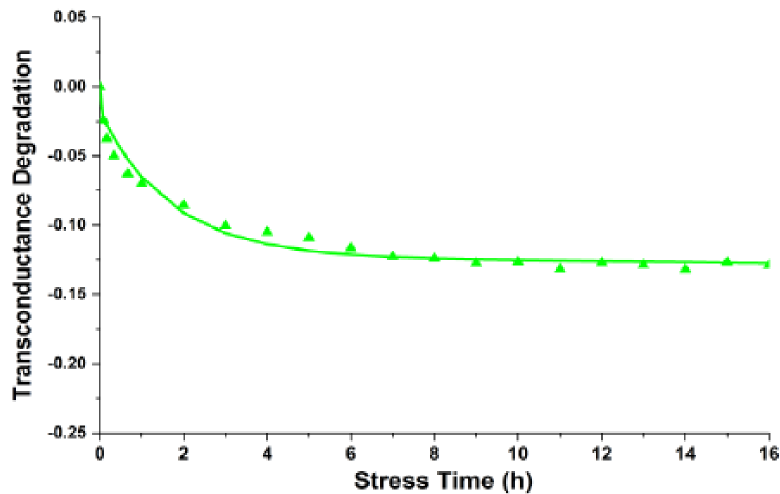

Fig. X-1. The best fit obtained by scaling the V_T shift exponential fit to the semi-ON stress data at 300 K to match the corresponding g_m degradation data at semi-ON (also 300 K).

A potentially self-consistent value of α can now be calculated by scaling the V_T shift equation until obtain the best match to g_m degradation for that specific condition. Fig. X-1 shows the best match to the g_m degradation data for 300 K using the equation for the 300 K V_T shift fit. The scaling factor obtained is,

$$\alpha \frac{W\ \varepsilon^2\ V_{DS}}{q\ L\ {d_{AlGaN}}^2} = 3.86 \qquad (X-8)$$

The value of α obtained from the 300 K stress data is about 4 x 10^{-9} cm^2. The g_m degradation simulations at other temperatures can be obtained by changing the values of τ and with the values of α and σ kept constant. Previous work shows that the values of α for similar carrier-defect scattering that are more than three orders of magnitude smaller [44], [45]. Hence, it is clear that a greater density of defects must contribute to the g_m degradation than to the V_T shifts. The simplest explanation of this result is that the charged defects that cause the V_T shift and g_m degradation build up at similar rates with stress, but differ in density and location. A self-consistent explanation for the above results is obtained if one assumes that the shifts in V_T are caused by the subset of defects at or near the gate-edge where the influence of traps on V_T is very strong, but the g_m degradation is determined by the charged defects of similar type located across a much broader region of the gate-drain access region.

Hence, for more accurate results we model the g_m degradation by directly relating it to the change in the charge density in the channel using [2], [46], [47]:

$$\Delta g_m(t) / g_{m0} = \frac{q\ \mu\ W\ h\ V_A}{L}\ \Delta Q'_d(t) \qquad (X-9)$$

where h is the channel thickness (25 nm), $\Delta Q'_d(t)$ is the stress-induced change in the volume charge density and the voltage V_A is given by,

$$\text{where } V_A = 1 - \left(\frac{V_{bi} - V_{GS}}{V_p}\right)^{1/2}$$

Here, V_{bi} is the built-in voltage and V_p is the threshold voltage of the device. Now, the transconductance degradation ($\Delta g_m/g_{m0}$) can be given as,

$$\frac{\Delta g_m(t)}{g_{m0}} = \frac{q\,\mu\,W\,h\,V_A}{L}\,[N_d^{\infty} - N_d(0)]\left(1 - e^{-\frac{t}{\tau}}\right) \qquad (X-10)$$

$$\text{where}\quad \frac{1}{\tau} = \sum_{E>E_{act}} n(E,T,V_{GS},V_{DS})\, v(E)\sigma$$

Unlike equation X-7, here the reduction in the transconductance degradation has been represented in terms of the initial value of peak transconductance (g_{m0}). As in the case of V_T modeling, the degradation at a different condition can be estimated by simply using the value of $\Sigma n(E)v(E)$ for the specific condition (obtained from the EMC simulation results) in the equation above. The scattering cross-section (σ) is assumed to be constant. Similar to the case of the V_T shift prediction equation in chapter IV, the g_m degradation prediction equation can be extended to include multiple defects,

$$\frac{\Delta g_m(t)}{g_{m0}} = \frac{q\,\mu\,W\,h\,V_A}{L}\left\{[N_d^{\infty} - N_d(0)]'\left(1 - e^{-\frac{t}{\tau_1}}\right) + \right.$$

$$[N_d^{\infty} - N_d(0)]''\left(1 - e^{-\frac{t}{\tau_2}}\right) + \cdots$$

$$\left. \ldots + [N_d^{\infty} - N_d(0)]^{n'\cdots}\left(1 - e^{-\frac{t}{\tau_n}}\right)\right\} \qquad (X-11)$$

where the time constants for the defects are as follows,

$$\frac{1}{\tau_1} = \sum_{E>E_{act1}} n(E,T,V_{GS},V_{DS})\, v(E)\sigma_1$$

$$\frac{1}{\tau_2} = \sum_{E>E_{act2}} n(E,T,V_{GS},V_{DS})\, v(E)\sigma_2$$

…..

$$\frac{1}{\tau_n} = \sum_{E>E_{actn}} n(E,T,V_{GS},V_{DS})\, v(E)\sigma_n$$

10.2 Results of Predictive Modeling

We consider the example of the Ga-rich devices again, with substitutional oxygen as the likely defect in the GaN buffer. Similar to the case of V_T shift modeling, the first step of the g_m modeling process is to estimate the scattering cross-section (σ) of the defect. We calculate this value by fitting the 300 K semi-ON stress test data (please check Fig. I-1, green-triangle data points) using equation X-10. The value of σ for this data set is approximately 1.4 x 10^{-16} cm^2. Keeping the value of σ constant throughout, we estimate the g_m degradation predictions for different temperatures by using the respective values of $\Sigma n(E)v(E)$ at 0.5 eV (the activation energy of substitutional oxygen) from Fig. VIII-1 in equation X-10.

The predictions are compared with the stress test data obtained at semi-ON condition for 250 K, 350 K and 400 K. The prediction results show good agreement with the stress test data for all the temperatures in the initial 2-3 hours. Up to 350 K the predictions are good till the 16 hour mark. But for 400 K stress, the stress test data deviates from the prediction results significantly. The experimental data for 400 K do not show saturation within 16 hours. This continuation of degradation may be due to the activation of another defect with a higher activation energy (but same charge state) at the elevated temperatures.

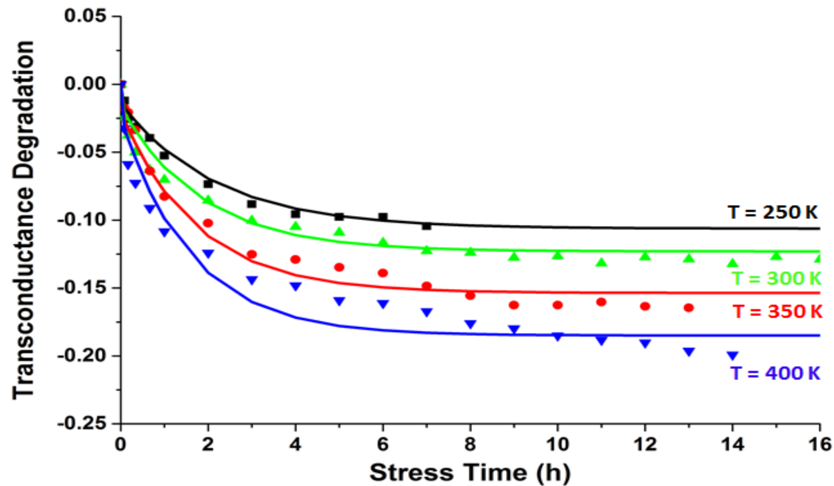

Fig. X-2. The g_m degradation predictions (Ga-rich devices) obtained for different temperatures at semi-ON (V_{GS} = -2 V,V_{DS} = 20 V) compared with the experimental data for the corresponding temperature. The scattering cross-section (σ) of the defect is initially estimated from the time constant (τ) calculated from the fit to the 300 K data.

We next try to understand the dependence of the operating temperature and the activation energy of the defect on the scattering cross-section of the defect. In this case, the semi-ON stress data has been directly fitted for the four temperatures on the Ga-rich devices (from Fig. X-2) using the single-defect g_m degradation equation (equation X-10). The dependence of the scattering cross-section on the temperature for 0.5 eV has been reported in Fig. X-3 (a), and the dependence of scattering cross-section on the temperature (with respect to different defect activation energies) calculated (from g_m data) in Fig. X-3 (b). The scattering cross-section values obtained for 250 K is significantly larger compared to the other temperatures.

a)

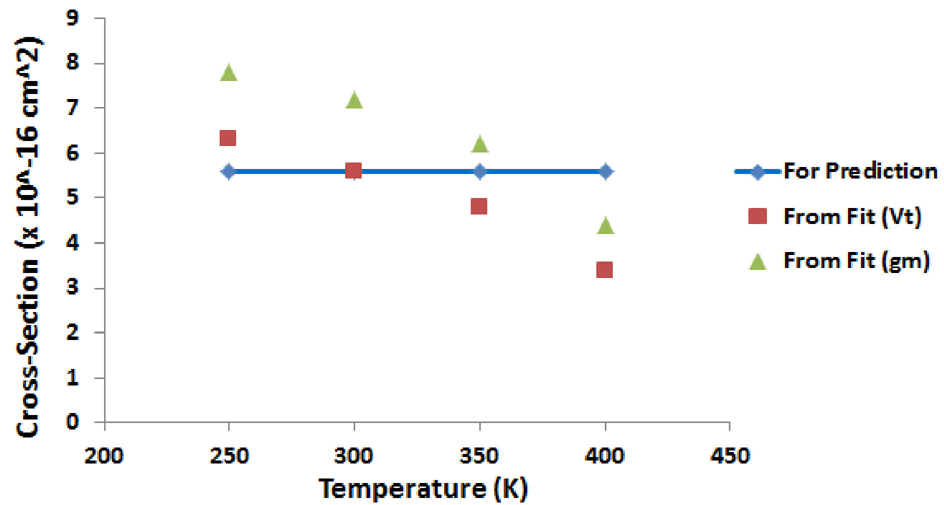

b)

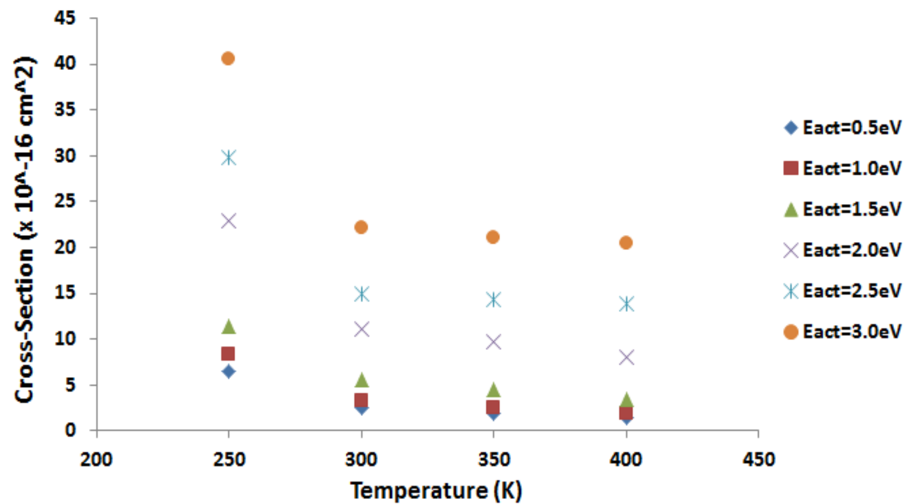

Fig. X-3. Impact on the extracted scattering cross-section values from the fit to the semi-ON stress temperature data when the cross-section is assumed to be energy-dependent.

10.4 Prediction for Longer Duration Stress

This section compares the results of long duration g_m degradation test data with the prediction results. In this approach, we keep the value of σ (obtained from the fit to V_T shift data, first 10 hours) constant and scale the V_T shift equation till it matches the g_m degradation data (similar to X-7) for the first 10 hours. Then, we can keep the values of σ and α constant and determine degradation at a longer time. The comparison of the prediction result with the stress test data indicates that the agreement is again reasonably good till the 30 hour mark (similar to the long duration V_T case), following which the stress test data deviates from the prediction results.

a)

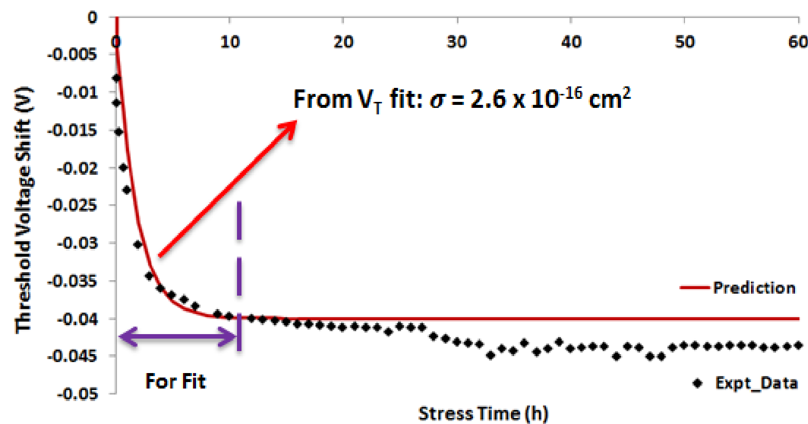

b)

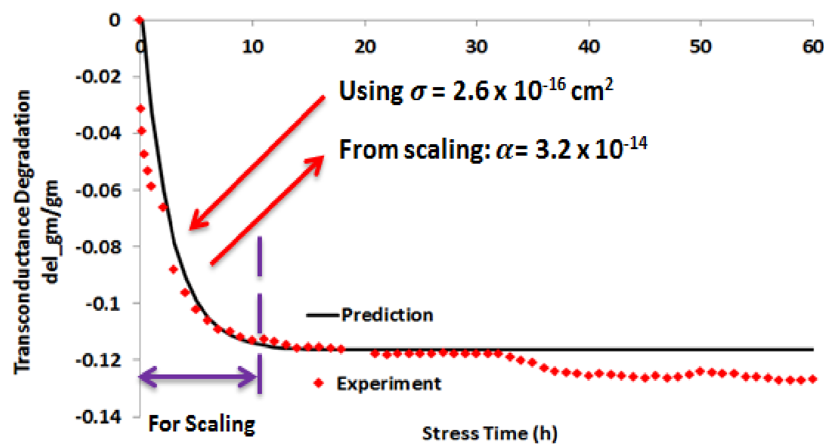

Fig. X-4. The long duration g_m degradation prediction (Ga-rich) obtained for V_{GS} = -2 V at 300 K (for V_{DS} = 20 V). The prediction is based on the scattering cross-section value obtained from the exponential fit to the first 10 hours of the stress test data (Fig (a)), and α obtained from scaling the V_T shift to closely match the g_m degradation data at 300 K, again for the first 10 hours (Fig (b)).

CHAPTER XI

MODELING MULTIPLE DEFECTS: V_T AND TRANSCONDUCTANCE

Since the model including one defect was insufficient to explain the degradation observed at elevated temperatures, we try to model the stress test data with multiple defects. This chapter provides a description of the procedure of modeling with multiple defects. The approach can be extended to both V_T shift and g_m degradation experiment results.

11.1 Fit with Two Defects (or a Defect with Two Energy Barriers)

The multiple-defect model includes multiple exponentials with dependence on the carrier energy distribution. The number of exponentials with different time constants (τ) is equal to the number of defects believed to be present in the device. The V_T degradation model with multiple defects is shown in equation XI-1. Each defect-type is assumed to have a different concentration of pre-existing defects. The corresponding g_m degradation can be obtained similar to g_m for the one-defect model, and is shown in equation XI-2.

$$\Delta V_T(t) = \frac{q\, d_{AlGaN}}{\varepsilon}\left\{[N_d^{\infty} - N_d(0)]'\left(1 - e^{-\frac{t}{\tau_1}}\right) + [N_d^{\infty} - N_d(0)]''\left(1 - e^{-\frac{t}{\tau_2}}\right) + \cdots \right.$$
$$\left. \ldots + [N_d^{\infty} - N_d(0)]'^{\cdots}\left(1 - e^{-\frac{t}{\tau n}}\right)\right\} \qquad (XI-1)$$

$$\frac{\Delta g_m(t)}{g_{m0}} = \frac{q\, \mu\, W\, h\, V_A}{L}\left\{[N_d^{\infty} - N_d(0)]'\left(1 - e^{-\frac{t}{\tau 1}}\right) + [N_d^{\infty} - N_d(0)]''\left(1 - e^{-\frac{t}{\tau_2}}\right) + \cdots \right.$$
$$\left. \ldots + [N_d^{\infty} - N_d(0)]'^{\cdots}\left(1 - e^{-\frac{t}{\tau n}}\right)\right\} \qquad (XI-2)$$

where the time constants for the defects are,

$$\frac{1}{\tau_1} = \sum_{E > E_{act1}} n(E, \boldsymbol{T}, V_{GS}, V_{DS})\ v(E)\sigma$$

$$\frac{1}{\tau_2} = \sum_{E > E_{act2}} n(E, \boldsymbol{T}, V_{GS}, V_{DS})\ v(E)\sigma$$

$$\frac{1}{\tau_n} = \sum_{E > E_{actn}} n(E, \boldsymbol{T}, V_{GS}, V_{DS})\ v(E)\sigma$$

The first step of the process is to fit the V_T shift and g_m degradation data at 400 K with two defects. A model with two exponentials is sufficient to get a proper fit for the 400 K data for both the V_T shift and g_m degradation. This is a reasonable indication that a second defect is activated in the device at the elevated temperatures. The next step is to determine the activation energies of these defects. This can be done by calculating the values of $\Sigma n(E)v(E)$ from the time constants of each defect obtained from the fit. The values of activation energy for each can now be estimated from the results of the EMC simulations.

Fig. XI-1 shows the fits using two-defects to the V_T shift and g_m degradation data for 400 K semi-ON stress. The figures also show the individual contributions from each defect for both V_T and g_m. The fit to the V_T shift data gives 0.46 eV and 1.68 eV as the activation energies for the two defects. The fit to the gm degradation data gives 0.42 eV and 1.74 eV as the activation energies for the defects. From the individual contributions, it is clear that the defect with the higher activation energy is responsible for the continued degradation that we observe in the stress test data at 400 K. It can also be noted that the values of the defect activation energies obtained from V_T and g_m are reasonably close. The next step in the process is to identify the defects in GaN with energy barriers close to the values obtained using the fitting process. It is also important to calculate the exact values of energy barriers for this defect, in order to figure out whether it can fit stress test data at other conditions. Ab-initio DFT calculations are used again to identify the new defect and the energy barriers.

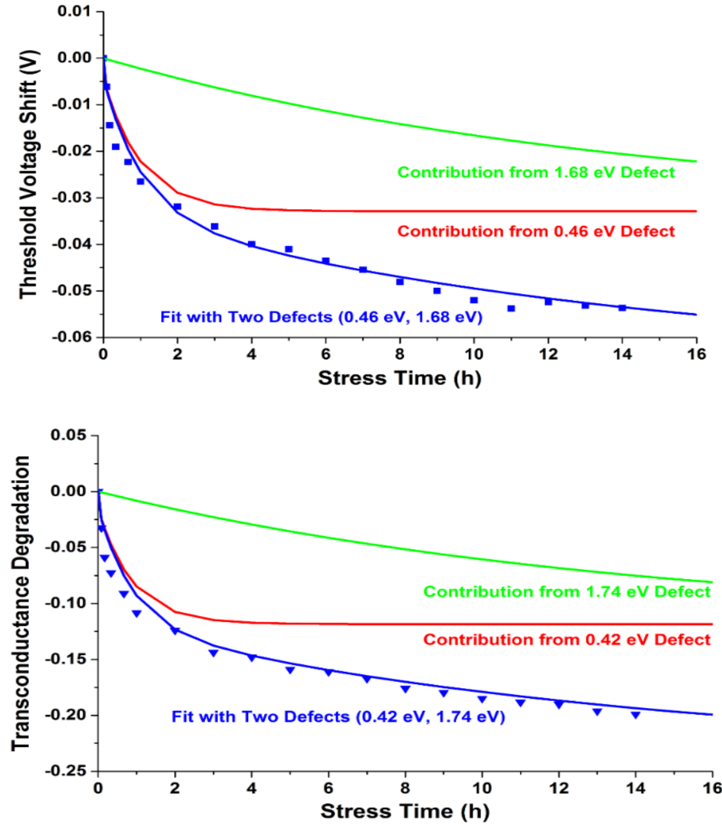

Fig. XI-1. The best fit to the V_T shift and g_m degradation data at 400 K using the two-defect exponential model. The relative contributions for each defect E_{act} has been also presented.

11.2 Likely Defect: Substitutional Iron Complex

Since the V_T shift is negative, the candidate defects that produce the degradation must reduce the negative net charge or increase the net positive charge. Negative V_T shift in devices grown in an NH_3-rich environment were attributed to the dehydrogenation of N antisite defects [23]. The present devices were grown in a Ga-rich environment, for which a lower percentage of N antisite defects are expected, so we must broaden the list of candidate defects. It has been recently reported that the iron-vacancy complex Fe_{Ga}-V_N can cause current collapse. The defect is initially hydrogenated and neutral, but upon dehydrogenation, it has an energy level at about 0.57 below the conduction band edge, is positively charged, and acts as an electron trap. Thus Fe_{Ga}-V_N-H is a good candidate for the degradation we are discussing here. Other candidate defects on the basis of past work and new analysis are Fe_{Ga}-H and hydrogenated oxygen complexes [26].

a)

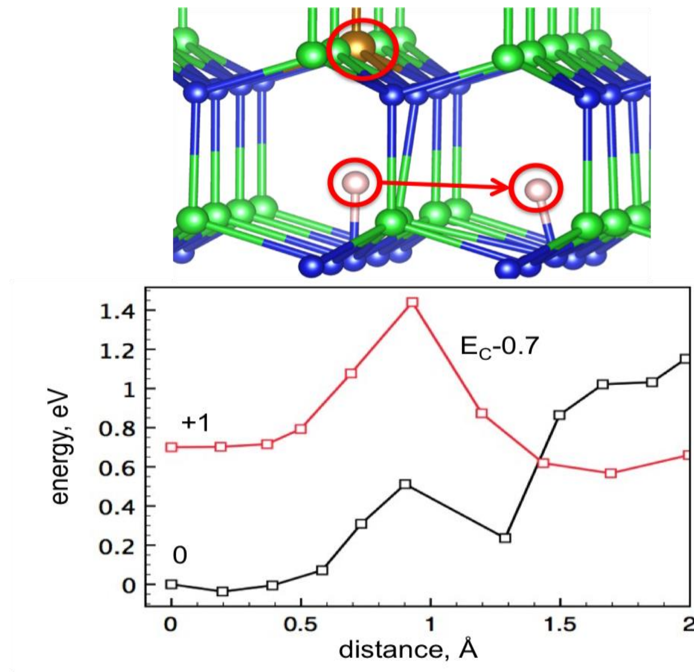

b)

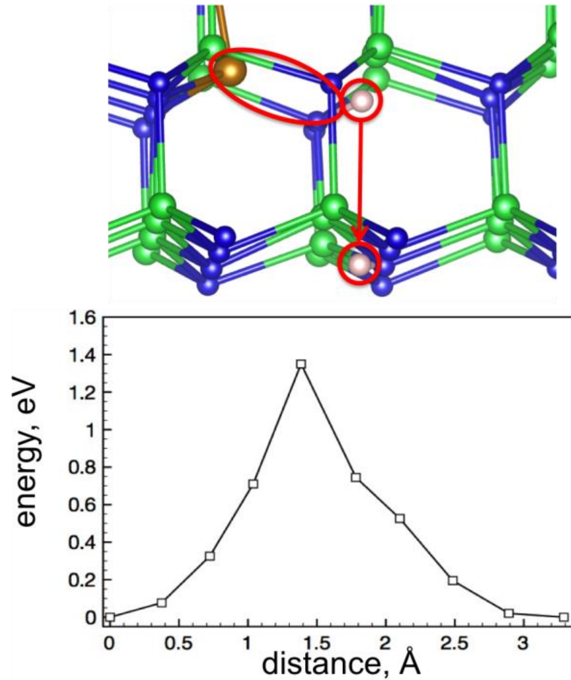

Fig. XI-2. Atomic configurations are shown above the corresponding migration energy barriers of H removal from iron impurity. Red circles show the positions of Fe (in brown) and H. Arrows connect initial and final H positions. These positions correspond to the initial and final points of the distance axis in the migration energy plots. Nitrogen atoms are shown in blue; gallium atoms are shown in green. (a) H migration near Fe_{Ga} with the barrier of 0.6 eV. (b) The defect configurations of H migration near Fe-V_N with barrier of 1.4 eV [24].

We now show that the charge states and activation energies for the dehydrogenation of Fe_{Ga}-V_N-H and Fe_{Ga}-H enable a self-consistent description of the full data set. Energy barriers for dehydrogenation of Fe_{Ga} and Fe-V_N complexes are shown in Fig. I-1. The values are 0.6 eV for Fe_{Ga} and 1.4 eV for Fe_{Ga}-V_N. Fig. XI-2 (a) shows the configurations of hydrogenated Fe_{Ga} before and after H migration across an atomic plane, and the corresponding energy barriers for neutral and positively charged complexes.

The charge state of the complex is determined by choosing the state (neutral or positive) with lower energy at the H atom position on the migration path. Therefore, the charge state of Fe_{Ga} changes from neutral to positive as the minimum energy changes at the crossing of the migration barrier curves. Hydrogen migration, which controls both V_T shift and g_m degradation, is rate-limiting for lower temperature stress, where the migration barrier for the initial step of moving away by one unit cell is 0.6 eV. The x-axis shows the distance between the initial position and the position of H along the removal path. The relative positions of the energy barrier curves depend on the Fermi level, which is at E_c–0.7 eV during high-field stress.

Atomic configurations and the energy barrier for H removal from the Fe_{Ga}-V_N complex are shown in Fig. XI-2(b). This removal from Fe_{Ga}-V_N occurs without changing the charge state. The barrier for the H to migrate more than one unit cell away from the impurity complex occurs with an energy barrier of 1.4 eV. This corresponds to the diffusion barrier of H in GaN. After H diffuses from the Fe_{Ga}-V_N complex, the resulting configuration is an isolated Fe_{Ga}-V_N^{+1}, causing an additional shift in V_T and further degradation in g_m. This process of complete removal of H from the impurity, characterized by the energy barrier of 1.4 eV, describes the degradation at the elevated temperatures (above 350 K).

We now show using equation X-1 that a degradation model with E_{act1} and E_{act2} equal to 0.6 eV and 1.4 eV, associated with the above dehydrogenation processes, can self-consistently describe the device response (V_T shift) vs. temperature. Fig. XI-1 shows the fits for the V_T shift for stress data at four temperatures using the two activation energies.

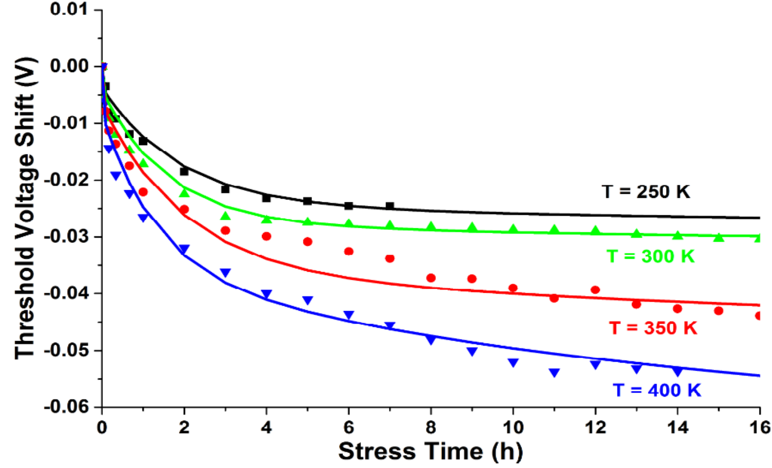

Fig. XI-3. The V_T shift data for the devices stressed at semi-ON for different temperatures modeled using two-defect model, with the activation energies of 0.6 eV (for the initial barrier) and 1.4 eV (for the complete removal of H).

11.3 Modeling Temperature Stress Data (considering Substitutional Iron)

In this process, σ_1 and σ_2 are treated as free parameters. We first fit the data at 400 K, where the deviation from a single-defect model is largest. The best-fit values obtained at 400 K for σ_1 and σ_2 are 8.2×10^{-16} cm^2 and 2.3×10^{-16} cm^2, respectively. The time constants corresponding to the two defect activation energies are calculated for the other temperatures using these values of σ_1 and σ_2, without further adjustment. The remaining temperature dependence enters entirely through the electron energy distribution. The calculated values of time constants obtained as a result are listed in Table XI-1. We use these time constants to model $\Delta V_T(t)$ for the other three temperatures. As shown in Fig. XI-3, the model describes the degradation well at all temperatures. The model agreement is essentially the same if E_{act1} varies by up to ± 0.1 eV and/or E_{act2} varies by up to ± 0.25 eV. These results provide strong evidence that dehydrogenation of Fe_{Ga}-H and Fe_{Ga}-V_N-H are the most likely origins of the observed hot-electron degradation. The values for the concentrations of available pre-existing defects obtained from this process are listed in Table XI-2. The pre-existing concentration for the higher-energy defect (Fe_{Ga}-V_N-H) is greater at 400 K than at other temperatures, consistent with activation of a second defect.

TABLE XI-1

Calculated time constants at different temperatures for the defect activation energies of 0.6 eV and 1.4 eV, respectively. The time constants for 400 K are obtained directly from the two-activation-energy fit to the 400 K stress experiment data.

Temperature (semi-ON)	For E_{act} = 0.6 eV $1/\tau$ (h)	For E_{act} = 1.4 eV $1/\tau$ (h)
250 K	0.486	0.043
300 K	0.538	0.048
350 K	0.636	0.056
400 K	0.763	0.067

TABLE XI-2

Concentrations of available pre-existing defects at different temperatures for the defect activation energies of 0.6 eV and 1.4 eV, obtained from the exponential fits to the data of Fig XI-3.

Temperature (semi-ON)	For E_{act} = 0.6 eV $[N_d^{\infty} - N_d(0)]_1$ (cm^{-2})	For E_{act} = 1.4 eV $[N_d^{\infty} - N_d(0)]_2$ (cm^{-2})
250 K	1.28×10^{11}	0.31×10^{11}
300 K	1.46×10^{11}	0.36×10^{11}
350 K	1.66×10^{11}	0.47×10^{11}
400 K	1.87×10^{11}	1.19×10^{11}

We can also show using the equation XI-2 that the degradation model with E_{act1} and E_{act2} equal to 0.6 eV and 1.4 eV can be used for the g_m degradation too. Fig. XI-4 shows that the g_m degradation data for the four temperatures can be modeled well using the two activation energies.

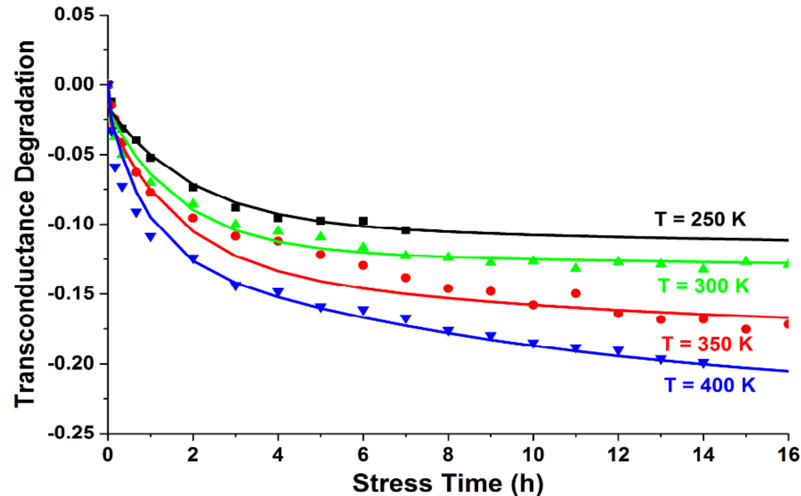

Fig. XI-4. Fits to the transconductance degradation $(\Delta g_m / g_m)$ data for the devices stressed at semi-ON (V_{GS} = -2 V, V_{DS} = 20 V) for different temperatures using the two-defect model, with defect activation energies of 0.6 eV and 1.4 eV.

Although defects with the same microstructure appear to be causing the shifts in threshold voltage and degradation in transconductance, it is not just the subset of the charged defects under the gate that cause the threshold voltage shifts that also cause the transconductance degradation. Instead, it is likely that similar defects located in the gate-drain access region dominate the transconductance degradation. Recent work using scanning Kelvin probe microscopy suggests that the Fe complexes responsible for the degradation in these devices do not lie in the AlGaN layer, but instead are located in the GaN buffer [48]-[50].

We conclude that dehydrogenation of substitutional iron complexes is largely responsible for the hot-carrier degradation observed in these devices. A two-defect energy-level model is developed that accounts for the time and temperature dependence of the observed degradation in V_T and g_m. The early-stage degradation observed in these devices at lower temperatures results from the electron-activated process of hydrogen migration across the atomic plane, causing a charge state change in a Fe_{Ga} impurity complex, characterized by a 0.6 eV activation barrier. The higher temperature degradation is caused both by dehydrogenation of Fe_{Ga}-H and dehydrogenation of Fe_{Ga}-V_N-H whose activation barrier is 1.4 eV. Similar defects located near the drain-edge of the gate and in the gate-drain access region are evidently responsible for the V_T shifts and g_m degradation in these devices, respectively.

CHAPTER XII

CONCLUSIONS

The physical mechanisms affecting the reliability of AlGaN/GaN High Electron Mobility Transistors operating at moderate drain biases are explored in this work. A predictive model is developed to describe the degradation of transistor characteristics (like V_T and g_m) over time. The model is based on the assumption that the degradation in device performance at moderate drain biases is due to the formation or modification of charged point defects by energetic electrons. These energetic electrons have sufficient energies to create these defects by hydrogen depassivation (electron-activated hydrogen removal) process. A combination of EMC simulation statistics, ab-initio DFT calculation and accelerated stress experiment fit results are used to describe the type of defect and the overall degradation behavior. The EMC as well as TCAD simulations indicate that the highest degradation is expected in the 'semi-ON' state of operation. We observe a significant increase in the density of both moderate as well as high energy carriers at semi-ON (between V_{GS} = -1.5 V and V_{GS} = -2.5 V) at the end of the gate on the gate-drain access region side where the lateral electric field is very high. The stress experiments confirm that the device degradation (both V_T and g_m) is at its maximum for V_{GS} = -2.0 V. The semi-ON stress tests indicate a relatively minor shift for V_T (about 1.0 to 1.5 %) but a very large degradation in gm (about 12 to 20 %) within 24 hours. We observe this trend consistently across a range of devices fabricated using different processing techniques like PA-MBE and MOCVD. The combination of very high electric field (at the gate edge) and moderate density of carriers in the semi-ON state is the primary reason behind this degradation. The large degradation of g_m in the semi-ON state can be a big concern to the designers of high efficiency (class-AB) high-power microwave amplifiers as these devices are biased very close to pinch-off.

The candidate defects are identified using the DFT calculations by understanding the process conditions and the polarity of the charge build-up (from the direction of V_T shift). The scattering cross-section of the defect is calculated using the defect generation rate equation. The carrier-energy distribution is obtained from the EMC simulations whereas the barrier for the removal of hydrogen is calculated using DFT. The scattering cross-section used in the calculations is assumed to be a step function for simplicity, transitioning at the activation barrier. The difference in V_T shifts in the model is linked to the values of the time constants which are obtained from the energetic carrier distributions (from EMC simulations). The g_m degradation is initially linked to the V_T shift through a mobility reduction model, using a constant to represent the scattering strength. A single defect model is sufficient to describe the bias-dependence of both V_T shift and g_m degradation. For the devices grown using PA-MBE, the degradation in the Ga-rich devices is attributed to substitutional oxygen (E_{act} = 0.5 eV), whereas the degradation in N-rich devices is attributed to hydrogenated gallium vacancies (E_{act} = 2.1 eV). For the devices grown using MOCVD, the degradation in the NH_3-rich devices is attributed to the nitrogen anti-sites (E_{act} = 1.8 eV). In the case of longer duration stress experiments, the V_T shift and g_m degradation models show reasonably good agreement with the experimental data till the 30-32 hour mark.

The semi-ON state temperature stress experiments indicate that both the V_T shift and g_m degradation increase with the device temperature. The carrier-energy distributions from the EMC simulations show that the density of moderate energy (0.5 to 2.5 eV) carriers increases with the rise in temperature whereas the density of high energy (greater than 2.5 eV) carriers decreases at elevated temperatures. This observation can be attributed to the rise in phonon scattering of electrons at elevated temperatures. The temperature dependence of the degradation is explained well with a single defect model till 350 K. At higher temperatures, the experimental data deviate considerably from the model. For example, for the Ga-rich devices the single defect model considering substitutional oxygen (E_{act} = 0.5 eV) did not match the experimental data at 400 K. Hence, we introduce a multiple-defect model to explain the effects at higher temperatures. The

calculations show a two-defect model with activation energies of 0.5 eV and 1.45 eV can fit the experimental data for 400 K well. The DFT calculations indicate that dehydrogenation of substitutional iron and its complexes is the likely defect. The initial barrier for the removal of hydrogen in these complexes is 0.6 eV, and the process of complete removal of hydrogen is characterized by a barrier of 1.4 eV. The semi-ON stress temperature data can be modeled well with these two activation energies. Iron is a well-known contaminant in GaN-based devices, especially those grown using the PA-MBE technique. The V_T shift in these devices is due to the presence of these defects under the gate (peaking at the gate-edge), whereas the g_m degradation is due to scattering of electrons from the defects which are present under the gate as well the gate-drain access region. The defects resulting in the device degradation are located at the AlGaN/GaN interface as well as the GaN buffer. Hence, only a subset of the charged defects actually contributes to the V_T shift whereas all the defects are contributing to the g_m degradation. This explains the relatively small shift in V_T compared to the larger reduction in g_m.

This work explores a very important topic in the field of GaN-based HEMT technology development. The conclusions from this work can be useful to the system designers as well as the process technologists working in this field. The designers can use the model for rough prediction of device performance parameters that may be useful in defining proper guard-bands (avoiding over-estimation). The process engineers can try to reduce (or eliminate) the defects identified in this work, which may be helpful in reducing the semi-ON state degradation. Additionally, the approach used in this work can be refined and extended to other III-V material-based systems (like LEDs, Solar Cells and MEMS/Sensors) where the primary reliability concern is the degradation due to hot electrons.

REFERENCES

[1] U. K. Mishra, P. Parikh and Y. F. Wu, "AlGaN/GaN HEMTs - an overview of device operations and applications," *Proc. of the IEEE*, vol. 26, pp. 117-135, Mar 2002.

[2] U. K. Mishra and J. Singh, Semiconductor Device Physics and Design, Berlin, Germany, *Springer*, 2007.

[3] U. K. Mishra, L. Shen, T. E. Kazior and Y. F. Wu, "GaN-based RF power devices and amplifiers," *Proc. of the IEEE*, vol. 96, pp. 287-305, Feb 2008.

[4] M. A. Khan, A. Bhattarai, J. N. Kuznia and D. T. Olson, "High electron mobility transistor based on GaN/$Al_xGa_{1-x}N$ heterojunction," *Appl. Phys. Lett.*, vol. 63, pp. 1214-1216, May 1993.

[5] M. Meneghini, A. Stocco, R. Silvestri, G. Meneghesso and E. Zanoni, "Degradation of AlGaN/GaN high electron mobility transistors related to hot carriers," *Appl. Phys. Lett.*, vol. 100, p. 233508, May 2012.

[6] C. Whelan, N. Kolias, J. Smolko, T. Kazior and S. Bernstein, "State-of-the-art RF semiconductors for military systems," *Raytheon Technology Highlights*, Sep 2013.

[7] D. Aichele, "High power GaN solutions for next-generation RADAR," *European Microwave Week 2012 (RFMD)*, Oct 2012.

[8] J. A. del Alamo and J. Joh, "GaN HEMT reliability," *Microelectron. Reliab.*, vol. 49, no. 9, pp. 1200-1206, Sep 2009.

[9] U. K. Mishra, "Reliability of AlGaN/GaN HEMTs; An overview of the results generated under the ONR DRIFT program," *Proc. of the IEEE Int. Reliability Physics Symp*., Apr 2012, pp. 2C.1.1-2C.1.6.

[10] S. Sque, "High-voltage GaN-HEMT devices, simulation and modeling," *ESSDERC 2013 (NXP Semiconductors),* Nov 2013.

[11] A. Kalavagunta, "Understanding the impact of bulk traps on GaN HEMT DC and RF characteristics," *Doctoral Dissertation (EE)*, Vanderbilt University, Jan 2009.

[12] J. P. Ibbetson, P. T. Fini, K. D. Ness, S. P. DenBaars, J. S. Speck and U. K. Mishra, "Polarization effects, surface states, and the source of electrons in AlGaN/GaN HFETs," *Appl. Phys. Lett.*, vol. 77, pp. 250-252, Nov 2000.

[13] G. Meneghesso, G. Verzellesi, F. Danesin, F. Rampazzo, F, Zanon, A. Tazzoli, M. Meneghini and E. Zanoni, "Reliability of GaN high-electron-mobility transistors: State of the art and perspectives," *IEEE Trans. Dev. Mater. Reliab.*, vol. 8, no. 2, pp. 332-343, Jun 2008.

[14] G. Meneghesso, M. Meneghini, A. Tazzoli, N. Ronchi, A. Stocco, A. Chini and E. Zanoni, "Reliability issues of Gallium Nitride High Electron Mobility Transistors," *IEEE J. Microwave Wireless Tech.*, vol. 2, pp. 39-50, Feb 2010.

[15] J. Jungwoo and J. A. del Alamo, "Critical voltage for electrical degradation of GaN high-electron mobility transistors," *IEEE Electron Device Lett.*, vol. 29, no. 4, pp. 287-289, Apr 2008.

[16] P. Makaram, J. Joh, J. A. del Alamo, T. Palacios and C. V. Thompson, "Evolution of structural defects associated with electrical degradation in AlGaN/GaN high electron mobility transistors," *Appl. Phys. Lett.*, vol. 96, p. 233509, May 2010.

[17] E. Zanoni, F. Danesin, M. Meneghini, M. Peroni and G. Meneghesso, "Localized damage in AlGaN/GaN HEMTs induced by reverse-bias testing," *IEEE Electron Device Lett.*, vol. 30, no. 5, pp. 427-429, May 2009.

[18] U. Chowdhury, J. L. Jiminez, C. Lee, E. Beam, T. Balistreri, J. Wang and J. A. del Alamo, "TEM observation of crack-and-pit-shaped defects in electrically degraded GaN HEMTs," *IEEE Electron Device Lett.*, vol. 29, no. 10, pp. 1098-1100, Sep 2008.

[19] M. Meneghini, A. Stoccio, M. Bertin, D. Marcon, A. Chini, G. Meneghesso and E. Zanoni, "Time-dependent degradation of AlGaN/GaN HEMTs under reverse bias," *Appl. Phys. Lett.*, vol. 100, p. 033505, May 2012.

[20] E. Zanoni, G. Meneghesso, M. Meneghini, F. Rampazzo, A. Tazzoli and F. Zanon, "A comprehensive reliability investigation of the voltage-, temperature- and device geometry-dependance on state-of-the-art GaN-on-Si HEMTs," *Proc. of the IEEE Int. Electron Devices Meeting*, Dec 2010, pp. 20.3.1-20.3.4.

[21] Presentation for structures of HEMTs fabricated at UCSB (Internal communication with S. Kaun and E. Kyle).

[22] T. Roy, "Reliability-limiting defects in GaN high electron mobility transistors," *Doctoral Dissertation (EE),* Vanderbilt University, Oct 2011.

[23] Y. Puzyrev, T. Roy, M. Beck, B. R. Tuttle, R. D. Schrimpf, D. M. Fleetwood and S. T. Pantelides, "Dehydrogenation of defects and hot-electron degradation in GaN high electron mobility transistors," *J. Appl. Phys.*, vol. 109, p. 034501, May 2011.

[24] S. Mukherjee, Y. S. Puzyrev, J. Chen, R. D. Schrimpf, D. M. Fleetwood and S. T. Pantelides, "Hot carrier degradation in AlGaN/GaN HEMTs due to substitutional Iron and its complexes," *IEEE Trans. Electron Devices,* (under review).

[25] R. D. Schrimpf, D. M. Fleetwood, S. T. Pantelides, Y. S. Puzyrev, S. Mukherjee, R. A. Reed, J. S. Speck and U. K. Mishra "Physical mechanisms affecting the reliability of GaN-based high electron mobility transistors," *MRS Proceedings*, vol. 1792, pp. 1316-1320, Mar 2015.

[26] Y. Puzyrev, S. Mukherjee, J. Chen, T. Roy, M. Silvestri, J. M. Hinckley, R. D. Schrimpf, D. M. Fleetwood, J. Singh, A. Paccagnella and S. T. Pantelides, "Gate bias dependence of defect-mediated hot-carrier degradation in GaN HEMTs," *IEEE Trans. Electron Devices*, vol. 61, no. 5, pp. 1316-1320, May 2014.

[27] S. Mukherjee, Y. Puzyrev, J. M. Hinckley, R. D. Schrimpf, D. M. Fleetwood, J. Singh and S. T. Pantelides, "Role of bias conditions in the hot carrier degradation of AlGaN/GaN HEMTs," *Phys. Stat. Sol. c*, vol. 10, no. 5, pp. 794-798, May 2013.

[28] A. Kalavagunta, S. Mukherjee, R. A. Reed and R. D. Schrimpf, "Comparison between trap and self-healing induced mobility degradation in AlGaN/GaN HEMTs," *Microelectron. Reliab.*, vol. 54, no. 3, pp. 570-574, Mar 2014.

[29] University of Michigan HFET user manual (Internal communication with J. Singh).

[30] Y. R. Wu, M. Singh and J. Singh, "Device scaling physics and channel velocities in AlGaN/GaN HFETs: Velocities and effective gate length," *IEEE Trans. Electron Devices*, vol. 53, no. 4, pp. 588-593, Apr. 2006.

[31] Y. R. Wu and J. Singh, "Transient study of self-heating effects in AlGaN/GaN HFETs," *J. Appl. Phys.*, vol. 101, p. 113712, May 2007.

[32] Y. R. Wu, M. Singh and J. Singh, "Sources of transconductance collapse in III-V nitrides - Consequences of velocity-field relations and source/gate design," *IEEE Trans. Electron Devices*, vol. 52, no. 6, pp. 1048-1054, May 2005.

[33] Y. Zhang, I. P. Smorchkova, C. R. Elsass, J. P. Ibbetson, S. Denbaars, U. K. Mishra and J. Singh, "Charge control and mobility in AlGaN/GaN transistors: Experimental and theoretical studies," *J. Appl. Phys.*, vol. 87, pp. 7981-7987, Feb 2000.

[34] GaN Band Strutcure, *NSM Archive*, Ioffe Institute, Russia.

[35] G. Kresse and J. Furthmuller, "Efficient iterative schemes for ab-initio total-energy calculations using plane-wave basis set," *Phys. Rev. B.*, vol. 54, pp. 11169-11172, Oct 1996.

[36] J. P. Perdew, K. Burke and M. Ernzerhof, "Generalized gradient approximation made simple," *Phys. Rev. Lett.*, vol. 77, pp. 3865-3867, Oct 1996.

[37] K. H. Warnick, Y. S. Puzyrev, T. Roy, D. M. Fleetwood, R. D. Schrimpf and S. T. Pantelides, "Room-temperature diffusive phenomena in semiconductors: The case of AlGaN," *Phys. Rev. B.*, vol. 84, p. 214109, Dec 2011.

[38] Y. Puzyrev, R. D. Schrimpf, D. M. Fleetwood and S. T. Pantelides, "Role of Fe impurity complexes in the degradation of AlGaN/GaN high electron mobility transistors," *Appl. Phys. Lett.*, vol. 106, p. 053505, Jan. 2015.

[39] G. Henkelman and H. Jonsson, "Improved tangent estimate in the nudged elastic band method for finding minimum energy paths and the saddle points," *J. Chem. Phys.*, vol. 113, no. 22, pp. 9978-9985, Aug. 2000.

[40] A. F. Wright, "Interaction of hydrogen with nitrogen interstitials in wurtzite GaN," *J. Appl. Phys.*, vol. 90, pp. 6526-6534, Jul. 2001.

[41] A. F. Wright, C. H. Seager, S. M. Myers, D. D. Koleske and A. A. Alerman, "Hydrogen configurations, formation energies, and migration barriers in GaN," *J. Appl. Phys.*, vol. 94, pp. 2311-2318, Jul. 2003.

[42] S. C. Sun and J. D. Plummer, "Electron mobility in inversion and accumulation layers on thermally oxidized silicon surfaces," *IEEE J. Solid-State Circuits*, vol. 15, no. 4, pp. 562-573, Aug. 1980.

[43] S. M. Sze and K. K. Ng, Physics of Semiconductor Devices, New York, US, *Wiley*, 2006.

[44] F. W. Sexton and J. R. Schwank, "Correlation of radiation effects in transistors and integrated circuits," *IEEE Trans. Nucl. Sci*., vol. 32, no. 6, pp. 3975-3981, Dec. 1985.

[45] K. F. Galloway, M. Gaitan and T. J. Russell, "A simple model for separating interface and oxide charge effects in MOS device characteristics," *IEEE Trans. Nucl. Sci*., vol. 31, no. 6, pp. 1497-1501, Dec. 1984.

[46] M. Delagebeaudeuf and N. T. Linh, "Metal-(n) AlGaAs-GaAs two-dimensional gas FET," *IEEE Trans. Electron Devices*, vol. 29, no. 6, pp. 955-960, Jun. 1982.

[47] N. Braga, R. Mickevicius, R. Gaska, X. Hu, M. S. Shur, M. A. Khan and J. Yang, "Simulation of hot electron and quantum effects in AlGaN/GaN heterostructure field effect transistors," *J. Appl. Phys.*, vol. 95, pp. 6409-6414, May 2004.

[48] A. Sasikumar, D. W. Cardwell, A. R. Arehart, J. Lu, S. W. Kaun, S. Keller, U. K. Mishra, J. S. Speck, J. P. Pelz and S. A. Ringel, "Toward a physical understanding of the reliability limiting Ec-0.57 eV trap in GaN HEMTs," in *IEEE Intl. Reliab. Phys. Symp.*, 2014, pp. 2C.1.1-6.

[49] D. W. Cardwell, A. Sasikumar, A. R. Arehart, S. W. Kaun, J. Lu, S. Keller, J. S. Speck, U. K. Mishra, S. A. Ringel and J. P. Pelz, "Spatially-resolved spectroscopic measurements of Ec-0.57 eV traps in AlGaN/GaN high electron mobility transistors," *Appl. Phys. Lett.*, vol. 102, p. 193509, May 2013.

[50] D. Bisi, M. Meneghini, M. V. Hove, D. Marcon, S. Stoffels, T.-L Wu, S. Decoutere, G. Meneghesso and E. Zanoni, "Trapping mechanisms in GaN-based MIS-HEMTs grown on silicon substrate," *Phys. Status Solidi A*, pp. 1-8, Jan. 2015.

[51] M. Meneghini, D. Bisi, M. V. Hove, D. Marcon, S. Stoffels, T.-L Wu, S. Decoutere, G. Meneghesso and E. Zanoni, "Trapping in GaN-based MIS transistors: Role of high drain bias and hot electrons," *Appl. Phys. Lett.*, vol. 104, p. 143505, Apr. 2014.

[52] M. Tapajna, N. Killat, V. Palankovski, D. Gregusova, K. Cico, N. Grandjean, J.-F. Carlin, M. Kuball and J. Kuzmik, "Hot-electron-related degradation in InAlN/GaN high electron mobility transistors," *IEEE Trans. Electron Devices*, vol. 61, no. 8, pp. 2793-2801, Jul. 2014.

BIOGRAPHICAL SKETCH

Shubhajit grew up in Mumbai, India. He received his bachelor's degree in Electronics and Communication Engineering from RAIT (University of Mumbai) in June 2005. From August 2005 to July 2007 he worked at an industrial automation start-up (SoftDEL Systems) in Mumbai as a Firmware Engineer designing ISM-band transreceiver systems. He joined the University of Houston in the fall of 2007 to pursue graduate studies. He received his master's degree in Electrical Engineering in December 2009. His thesis targeted the identification of process-level treatments which may reduce NBTI degradation in submicron CMOS technology.

Shubhajit joined Vanderbilt University in the fall of 2010 for his doctoral studies. He is enrolled under the Interdisciplinary Graduate Program in Materials Science. He has been part of the Radiation Effects and Reliability Group for last four years. The objective of his doctoral research is to understand the mechanisms of hot carrier-induced defect formation in GaN-based HEMTs, and to use this information to develop a predictive model. Shubhajit has interned as a Device Engineer with several semiconductor corporations during his stay at Vanderbilt. He interned with the Power A/MS Technology (HV-BiCMOS) Development division (Supertex Inc) of Microchip Technology in Mountain View, CA during the summer of 2011. He was with the Emerging Non-Volatile Memory (3D-XPoint) Process Integration team (Intel-Micron Flash JDP) of Micron Technology in Boise, ID during the summer of 2012. During the summer of 2013, he worked with the Xeon Technology Development (Skylake Architecture, Tri-Gate Technology) - Reliability Modeling group of Intel Corporation in Santa Clara, CA.